NASA Contractor Report 4183

Development of the General Interpolants Method for the CYBER 200 Series of Supercomputers

J. F. Stalnaker, M. A. Robinson,
L. W. Spradley, S. C. Kurzius,
and J. Thoenes

CONTRACT NAS1-15783
DECEMBER 1988

NASA Contractor Report 4183

Development of the General Interpolants Method for the CYBER 200 Series of Supercomputers

J. F. Stalnaker, M. A. Robinson,
L. W. Spradley, S. C. Kurzius,
and J. Thoenes
Lockheed Missiles & Space Company, Inc.
Huntsville Research & Engineering Center
Huntsville, Alabama

Prepared for
Langley Research Center
under Contract NAS1-15783

National Aeronautics
and Space Administration

**Scientific and Technical
Information Division**

1988

FOREWORD

This report constitutes final documentation of work performed by personnel of Lockheed's Huntsville Research & Engineering Center for NASA-Langley Research Center on Contract NAS1-15783. The purpose of the report is the presentation of the GIM code modifications and the latest flowfield calculations performed with the General Interpolants Method (GIM) computer code. The work describes the GIM code reacting flow model, the hyperbolic steady-state Euler version of the code, investigation of a solution adaptive grid algorithm, and improvements to the turbulence models. The authors gratefully acknowledge the contribution to and continued support of this work by the NASA-Langley Contract Monitors J. L. Hunt and R.C. Rogers. Inquiries concerning this report should be directed to:

John F. Stalnaker
Lockheed-Huntsville Research & Engineering Center
4800 Bradford Drive
Huntsville, Alabama 35807

Telephone: (205) 837-1800, ext. 401

CONTENTS

PRECEDING PAGE BLANK NOT FILMED

PAGE iv INTENTIONALLY BLANK

CONTENTS (Concluded)

1. INTRODUCTION AND SUMMARY

The General Interpolants Method (GIM) code was developed to analyze complex flow fields which defy solution by simple methods. The code uses numerical difference techniques to solve the full three-dimensional time-averaged Navier-Stokes equations in arbitrary geometric domains. The numerical analogs of the differential equations are derived by representing each flow variable with general interpolant functions. The point of departure then requires that a weighted integral of interpolants be zero over the flow domain. By choosing the weight functions to be the interpolants themselves, the GIM formulation can produce the classical implicit difference schemes. Choosing the weight functions to be orthogonal to the interpolant functions produces explicit finite difference type discrete analogs. By appropriate choice of constants in the weight functions, the GIM becomes analogous to standard finite difference schemes such as centered, backward, forward, windward and multi-step predictor-corrector schemes. The GIM analogs, however, are automatically produced for arbitrary geometric flow domains and hence are a general point of departure and provide flexibility in the choice of differencing schemes.

The GIM computer code was originally written for the CDC 7600 machine. The first effort that was accomplished under Contract to NASA-Langley was the conversion and reprogramming of the code for the CDC-STAR (now termed the CYBER 200 series) vector processor. The GIM-STAR code was then exercised for three-dimensional exhaust flows for application to Scramjet engine studies. The next sequential study in this computational fluid dynamics effort consisted of the development and application of a parabolized GIM algorithm, computation of the flow, including spillage, in a model aircraft inlet and investigation of linearized block implicit schemes for GIM application. These tasks were accomplished under two contracts through a cooperative effort of the Hypersonic Aerodynamics and Hypersonic Propulsion Branches. These efforts then continued to include program modification to fully utilize the features of the CYBER 203, inclusion of the implicit MacCormack algorithm, inclusion of algebraic and differential equation turbulence models, creation of an interactive input program, calculation of the inviscid flow about a wing-body configuration, and the incorporation of a finite rate nonequilibrium reacting flow model.

The most current effort, which is the subject of this report, is a continuation of the GIM code development and application on the CYBER 203 machine. Objectives of this effort include the following.

- Complete the development of the finite rate chemically reacting flow model.
- Validate the reacting flow model for hydrogen-air and hydrocarbon-air combustion by analyzing an experimental case.
- Develop a hyperbolic marching Euler solver for inviscid flowfield analysis.
- Investigate solution-adaptive grid algorithms for inclusion in the GIM code.
- Complete the formulation of the turbulence models in the GIM code.

Certain of these stated objectives were accomplished in full and other partially. The plan of attack was to organize a set of overall tasks, some of which are interrelated, aimed at meeting the major objectives. This report is organized into sections with each section independently presenting details of the major tasks. The following is a summary of these sections:

THE GIM CODE CHEMICALLY REACTING FLOW MODEL

The GIM code chemically reacting flow model has been developed to facilitate the calculation of a broad spectrum of flow fields involving chemical reactions. The GIM code model allows the calculation of frozen flow, equilibrium flow, and finite-rate nonequilibrium flow. Both an explicit and an implicit time integration scheme are available at the option of the user. All of the chemistry calculations are tailored to be readily compatible with the overall GIM code methodology and are highly vectorized so as to obtain maximum computational efficiency on the CDC CYBER 200 series of supercomputers. Furthermore, the model is completely general in that any number of reactions of the general form

$$\sum_{i=1}^{N} \nu'_{ij} A_i \rightleftarrows \sum_{i=1}^{N} \nu''_{ij} A_i \qquad j = 1,\ldots, \begin{matrix}\text{Number of}\\ \text{Reactions}\end{matrix}$$

can be considered. In addition to the regular GIM code integration input, the user must input the equation describing each reaction, reaction rate data, and tables of the thermodynamic properties of each species as a function of temperature. An initial estimate of the species mass fraction distribution is also required. As output, the GIM code produces the regular integration output plus species mass fraction distributions.

THE GIM HYPERBOLIC STEADY EULER SOLVER

The General Interpolants Method solution methodology was brought to bear on a spatial-marching MacCormack algorithm for the solution of the hyperbolic steady Euler equations of inviscid flow. The resulting code has the computational efficiency resulting from the combination of the explicit MacCormack algorithm, the progressive assembly of the GIM difference analogs (see Appendix D), and the CYBER 200 series of supercomputers. Further features of the method include the geometric versatility of all GIM derivatives and dynamic monitoring of the marching step size with the ability to interpolate secondary cross planes in order to maintain stability.

INVESTIGATION OF A SOLUTION ADAPTIVE GRID ALGORITHM FOR THE GIM CODE

A study was made to determine the feasibility and suitability of a solution adaptive grid scheme for the GIM code. This task consisted of a literature survey of currently available methods and development of a one-dimensional code implementing a test algorithm. The approach taken was to be the "boundary conforming" coordinate transformation whereby all the grid movement is contained in the form of metric coefficients. The grid velocities were determined by setting them proportional to the local pressure gradient. The one-dimensional algorithm and an example result are presented in this report. The example case is a standing shock wave in a tube. The grid points are shown to migrate toward the discontinuity in pressure. The shock profile is seen to improve over the fixed grid case in that the "wiggles" due to MacCormack differencing are no longer present. We conclude that adaptive grid methods are feasible for inclusion in the GIM code and that a three-dimensional study should be started toward this goal.

TURBULENCE MODELING IN THE GIM CODE

Section 5 describes improvements made to the turbulence models in the GIM code. The Baldwin-Lomax algebraic eddy viscosity model was extended to include two-dimensional and axisymmetric regions bounded by more than one wall. It was further modified to allow the user to limit the region of application of the model. The Turbulent Kinetic Energy (TKE) two-equation model was completed with the inclusion of wall function boundary conditions.

RECOMMENDATIONS

An important part of any research effort is the publishing of the findings and results. In addition to NASA Contractor Reports, the results of the GIM code development and applications have been presented at many professional society meetings and published in the open literature. The authors would like to acknowledge the realization of this aspect of research by the Langley personnel and thank them for their support in these efforts to disseminate knowledge.

Another equally important aspect of computational research is the effort to keep current and potential users of computer codes abreast of changes and modifications to the code. To this end a GIM Code User's Bulletin has been circulated as warranted and three courses have been given to aquaint users with the latest versions of the code.

To further enhance the GIM code's capability and to utilize its current potential, the following actions are recommended.

- Include the new streamlined assembly procedure in all GIM INTEG modules.
- Investigate solution-adaptive methods including adaptive grids, time steps, and difference schemes.
- Include higher order interpolants into the present geometry program and include other state-of-the-art grid generators.
- Restructure the code for storage optimization.
- Investigate matching techniques to allow the code to dynamically switch among the hyperbolic, parabolic, and elliptic options.
- Use the GIM approach as a solution methodology to take advantage of its geometric and algorithmic consistency for the development of better solution techniques.

Finally, the use of the GIM code by Langley personnel in their many research efforts is encouraged and recommended. Only through use and users' input can a code with the capability of the GIM code be developed along rational lines.

2. GIM CODE CHEMICALLY REACTING FLOW MODEL

2.1 INTRODUCTION

The GIM Code chemically reacting flow model has been developed to facilitate the calculation of a broad spectrum of flow fields involving chemical reactions. The GIM code model allows the calculation of frozen flow, equilibrium flow, and finite rate nonequilibrium flow. Both an explicit and an implicit time integration scheme are available at the option of the user. All of the chemistry calculations are tailored to be readily compatible with the overall GIM code methodology and are highly vectorized so that maximum computational efficiency can be obtained on the CDC CYBER 200 series of supercomputers. Furthermore, the model is completely general in that any number of reactions of the general form

$$\sum_{i=1}^{N} \nu'_{ij} A_i \rightleftarrows \sum_{i=1}^{N} \nu''_{ij} A_i \qquad j=1,\ldots,\text{Number of Reactions}$$

can be considered. In addition to the regular GIM code integration input, the user must input the equation describing each reaction, reaction rate data, and tables of the thermodynamic properties of each species as a function of temperature. An initial estimate of the species mass fraction distribution is also required. As output, the GIM code produces the regular integration output plus species mass fraction distributions.

This section details the theory and algorithms employed in the GIM code chemically reacting flow model and describes the input required to implement the model. Section 2.2 presents the governing equations used in the model, while Section 2.3 describes the computational model. Section 2.4 details the frozen flow and equilibrium flow models incorporated in the general chemically reacting flow model. Section 2.5 is an input guide describing use of the model as well as the inputs required. A sample nonequilibrium finite rate reacting chemistry calculation is presented in Section 2.6. Nomenclature and references are presented in Sections 2.7 and 2.8, respectively.

2.2 GOVERNING EQUATIONS

The governing equations for general three-dimensional chemically reacting flow with N species and M reactions as modeled in the GIM code include the following:

Global Continuity Equation

$$\frac{\partial \rho}{\partial t} + \sum_{j=1}^{3} \frac{\partial}{\partial x_j} (u_j \rho) = 0 \qquad (2.1)$$

Momentum Equations

$$\frac{\partial}{\partial t} (\rho u_i) + \sum_{j=1}^{3} \frac{\partial}{\partial x_j} (\rho u_i u_j - \tau_{ij}) + \frac{\partial p}{\partial x_i} = 0 \qquad i=1,2,3 \qquad (2.2a)$$

where

$$\tau_{ij} = \mu \left(\frac{\partial u_i}{\partial x_j} + \frac{\partial u_j}{\partial x_i} \right) + \delta_{ij} \lambda \sum_{k=1}^{3} \frac{\partial u_k}{\partial x_k} \qquad (2.2b)$$

Energy Equation

$$\frac{\partial}{\partial t} (\rho \mathcal{E}) + \sum_{i=1}^{3} \frac{\partial}{\partial x_i} \left[(\rho \mathcal{E} + p) u_i - \sum_{j=1}^{3} u_j \tau_{ij} - q_i \right] = 0 \qquad (2.3a)$$

where

$$\mathcal{E} = \sum_{i=1}^{N} c_i \left\{ h_{o_i} + \int_{T_o}^{T} c_{p_i} \, dT + h_{f_i} \right\} - \frac{p}{\rho} + \sum_{j=1}^{3} \frac{u_j u_j}{2} \tag{2.3b}$$

$$q_i = k \frac{\partial T}{\partial x_i} + \rho \mathcal{D}_i \sum_{j=1}^{N} \left\{ h_{o_j} + \int_{T_o}^{T} c_{p_j} \, dT + h_{f_j} \right\} \frac{\partial c_j}{\partial x_i} \tag{2.3c}$$

Species Continuity Equations

$$\frac{\partial}{\partial t} (\rho c_i) + \sum_{j=1}^{3} \frac{\partial}{\partial x_j} \left(\rho u_j c_i - \rho \mathcal{D}_j \frac{\partial c_i}{\partial x_j} \right) - \bar{m}_i \dot{w}_i = 0 \tag{2.4a}$$

where

$$\dot{w}_i = \sum_{j=1}^{M} (\nu''_{ij} - \nu'_{ij}) \left[k_{f_j} \prod_{\ell=1}^{N} \left(\frac{\rho c_\ell}{\bar{m}_\ell} \right)^{\nu'_{\ell j}} - k_{b_j} \prod_{\ell=1}^{N} \left(\frac{\rho c_\ell}{\bar{m}_\ell} \right)^{\nu''_{\ell j}} \right] \tag{2.4b}$$

$$k_{f_j} = A'_j (T - T'_{o_j})^{B'_j} \exp\left[C'_j / \Re / (T - T'_{o_j})^{D'_j} \right] \qquad j=1,M \tag{2.4c}$$

$$k_{b_j} = A''_j (T - T''_{o_j})^{B''_j} \exp\left[C''_j / \Re / (T - T''_{o_j})^{D''_j} \right] \qquad j=1,M \tag{2.4d}$$

$$k_{f_j}/k_{b_j} \equiv K_{c_j} = K_{p_j} (\Re T)^{\sum_{i=1}^{N} (\nu'_{ij} - \nu''_{ij})} \qquad j=1,M \tag{2.4e}$$

$$K_{p_j} = \exp(-\Delta G_j / \Re T) \qquad j=1,M \tag{2.4f}$$

$$\Delta G_j = \sum_{i=1}^{N} (\nu''_{ij} - \nu'_{ij}) \, [(\bar{h}_i - \bar{h}_{o_i}) + \bar{h}_{f_i} - T\bar{s}_i] \qquad j=1,M \tag{2.4g}$$

Equation of State

$$p = \rho \Re T \sum_{i=1}^{N} \frac{c_i}{\bar{m}_i} \tag{2.5}$$

Written in the conservation vector format employed in the GIM code, Eqs. (2.1) through (2.4) become

$$\frac{\partial U}{\partial t} + \sum_{j=1}^{3} \frac{\partial E_j}{\partial x_j} - H = 0 \tag{2.6a}$$

where U, E_j, and H are given below:

$$\left.\begin{aligned}
U = \begin{bmatrix} \rho \\ \rho u_1 \\ \rho u_2 \\ \rho u_3 \\ \rho \mathcal{E} \\ \rho c_1 \\ \vdots \\ \rho c_N \end{bmatrix} \qquad & \qquad H = \begin{bmatrix} 0 \\ \vdots \\ 0 \\ \bar{m}_1 w_1 \\ \vdots \\ \bar{m}_N w_N \end{bmatrix} \\
E_j = & \begin{bmatrix} \rho u_j \\ \rho u_j u_1 + \delta_{j1} p - \tau_{j1} \\ \rho u_j u_2 + \delta_{j2} p - \tau_{j2} \\ \rho u_j u_3 + \delta_{j3} p - \tau_{j3} \\ (\rho \mathcal{E} + p) u_j - \sum_{k=1}^{3} u_k \tau_{jk} - q_j \\ \rho u_j c_1 - \rho \mathcal{D}_j \frac{\partial c_1}{\partial x_j} \\ \vdots \\ \rho u_j c_N - \rho \mathcal{D}_j \frac{\partial c_N}{\partial x_j} \end{bmatrix}
\end{aligned}\right\} \tag{2.6b}$$

2.3 COMPUTATIONAL MODEL

2.3.1 General

The integration of Eqs. (2.1) through (2.4), or equivalently equation (2.6), is not as straightforward as it is when the flow field is considered alone. The species continuity Eqs. (2.4a) contain an algebraic production or source term, namely $\dot{w}_i$ which most often involves a characteristic time scale much smaller than the characteristic time scale typically associated with the flowfield integration. This results in a set of "stiff" partial differential equations which can be computationally difficult to integrate. Two techniques are available in the GIM code to integrate this set of equations. Both techniques employ the MacCormack (Ref. 1) explicit predictor-corrector scheme to integrate the flow field Eqs. (2.1) through (2.3). The species continuity Eqs. (2.4) are integrated using an iterative predictor-corrector-chemistry scheme in which the chemistry terms can be solved either explicitly or implicitly at the option of the user. The explicit scheme can be subject to severe time step restrictions but can be computationally quite efficient. The implicit scheme is not nearly so restricted with regard to the time step but requires more computational effort per time step.

2.3.2 Flowfield Differencing

The MacCormack explicit predictor-corrector differencing scheme is always used to integrate the flowfield Eqs. (2.1) through (2.3), or alternatively the first 5 of Eqs. (2.6). This scheme as used in the GIM code is given by:

$$P: \begin{cases} \delta \overline{U^{n+1}} = - \sum_{j=1}^{3} \frac{\partial^F}{\partial x_j} (E_j^n) & (2.7a) \\ B[\delta \overline{U^{n+1}}] \rightarrow \delta \overline{U^{n+1}} & (2.7b) \\ \overline{U^{n+1}} = U^n + \Delta t \; \delta \overline{U^{n+1}} & (2.7c) \end{cases}$$

$$
\text{C:}\quad \left\{
\begin{aligned}
\delta U^{n+1} &= -\sum_{j=1}^{3} \frac{\partial^{B}}{\partial x_j} \left(\overline{E_j^{n+1}}\right) && \text{(2.8a)}\\
B[\delta U^{n+1}] &\longrightarrow \delta U^{n+1} && \text{(2.8b)}\\
U^{n+1} &= U^{n} + \frac{\Delta t}{2} \left(\delta \overline{U^{n+1}} + \delta U^{n+1}\right) && \text{(2.8c)}\\
&= \overline{U^{n+1}} + \frac{\Delta t}{2} \left(\delta U^{n+1} - \delta \overline{U^{n+1}}\right)
\end{aligned}
\right.
$$

2.3.3 Chemistry Differencing

The species continuity Eqs. (2.4) or alternately the last N of Eqs. (2.6) are integrated using a predictor-corrector-chemistry scheme in which the chemistry production terms can be solved either explicitly or implicitly, at user option. This method employs the explicit MacCormack predictor-corrector differencing scheme to predict the influence of convection and diffusion which is then used in the final iterative chemistry step. This scheme as used in the GIM code is given below:

$$
\text{P:}\quad \left\{
\begin{aligned}
\delta \overline{U^{n+1}} &= -\sum_{j=1}^{3} \frac{\partial^{F}}{\partial x_j} \left(E_j^{n}\right) && \text{(2.9a)}\\
B[\delta \overline{U^{n+1}}] &\longrightarrow \delta \overline{U^{n+1}} && \text{(2.9b)}\\
\overline{U^{n+1}} &= U^{n} + \Delta t\, \delta \overline{U^{n+1}} && \text{(2.9c)}
\end{aligned}
\right.
$$

$$
\text{C:}\quad \left\{
\begin{aligned}
\delta \overline{\overline{U^{n+1}}} &= -\sum_{j=1}^{3} \frac{\partial^{B}}{\partial x_j} \left(\overline{E_j^{n+1}}\right) && \text{(2.10a)}\\
B[\delta \overline{\overline{U^{n+1}}}] &\longrightarrow \delta \overline{\overline{U^{n+1}}} && \text{(2.10b)}\\
\overline{\overline{U^{n+1}}} &= U^{n} + \frac{\Delta t}{2} \left(\delta \overline{U^{n+1}} + \overline{\overline{U^{n+1}}}\right) \\
&= \overline{U^{n+1}} + \frac{\Delta t}{2} \left(\delta \overline{\overline{U^{n+1}}} - \delta \overline{U^{n+1}}\right) && \text{(2.10c)}
\end{aligned}
\right.
$$

$$\text{CH:}\quad \begin{cases} \delta U^{n+1} = \left[\frac{1}{2} - \sum_{j=1}^{3} \frac{\partial^F}{\partial x_j} (E_j^n) - \sum_{j=1}^{3} \frac{\partial^B}{\partial x_j} (E^{\overline{n+1}}) \right] + (1 - \phi)\, H^n + \phi H^{n+1} & \text{(2.11a)} \\ B[\delta U^{n+1}] \rightarrow \delta U^{n+1} & \text{(2.11b)} \\ U^{n+1} = U^n + \Delta t\ \delta U^{n+1} & \text{(2.11c)} \end{cases}$$

where ϕ is an adjustable parameter which can vary between zero and one, $0 \le \phi \le 1$. The value of ϕ determines to what degree the chemistry production terms are treated explicitly or implicitly. A value of $\phi = 0$ renders the chemistry terms fully explicit, while a value of $\phi = 1$ yields a fully implicit treatment. Typically, a value of $\phi = 0.5$ is used which yields a second order trapezoidal-like integration scheme. If the magnitudes of the chemistry production terms are so large that the species continuity equations become stiff, then ϕ is adjusted toward a value of 1.0 so that the equations are integrated in a nearly fully implicit mode.

Equations (2.11) are implicit in U^{n+1} through the H^{n+1} term. These equations can be solved in an explicit manner through linearization of the H^{n+1} and the method of successive substitutions or they can be solved as is via the Newton-Raphson method for nonlinear equations.

2.3.3.1 Explicit Solution Technique

Equations (2.11) can be solved explicitly by linearizing the H^{n+1} term and then using the method of successive substitutions. This is done as follows:

Let H^{n+1} be approximated by

$$H^{n+1} = H^{(\ell)} + \left(\frac{\partial H}{\partial U}\right)^{(\ell)} [U^{(\ell)} - U^{(\ell-1)}] + O(\Delta t^2) \qquad (2.12)$$

$$(\ell) = 0,1,2....$$

where $(\partial H/\partial U)$ is the Jacobian matrix associated with the H vector and where superscript (ℓ) indicates evaluation using the ℓ^{th} iteration approximation of U^{n+1}. Combine Eqs. (2.11) and (2.12) to obtain

$$\left[\frac{U^{(\ell+1)} - U^{(\ell)}}{\Delta t}\right] = -\left[\frac{U^{(\ell)} - U^{n}}{\Delta t}\right] + \frac{1}{2}\left[-\sum_{j=1}^{3}\frac{\partial^{F}}{\partial x_j}(E_j^{n}) - \sum_{j=1}^{3}\frac{\partial^{B}}{\partial x_j}(\overline{E_j^{n+1}})\right]$$

$$+ (1 - \phi)\, H^{n} + \phi\left\{H^{(\ell)} + \left(\frac{\partial H}{\partial U}\right)^{(\ell)}\left[\frac{U^{(\ell)} - U^{(\ell-1)}}{\Delta t}\right]\Delta t\right\} \qquad (2.13)$$

Equation (2.13) represents N equations which are solved explicitly at each node in the flow field for the quantity

$$\left[\frac{U^{(\ell+1)} - U^{(\ell)}}{\Delta t}\right].$$

The values of $U^{(\ell+1)}$ are given by

$$U^{(\ell+1)} = U^{(\ell)} + \Delta t\left[\frac{U^{(\ell+1)} - U^{(\ell)}}{\Delta t}\right] \qquad (2.14)$$

Equations (2.13) and (2.14) are iterated on ℓ beginning with $U^{(1)} = U^{(0)} = U^{n}$ until the difference $U^{(\ell+1)} - U^{(\ell)}$ becomes negligible, at which time $U^{n+1} \equiv U^{(\ell+1)}$.

2.3.3.2 Implicit Solution Technique

Equations (2.11) can be solved implicitly by using the Newton-Raphson method for nonlinear equations as follows:

Combine Eqs. (2.11) and define F^{n+1}

$$F^{n+1} = \left(\frac{U^{n+1} - U^{n}}{\Delta t}\right) - \frac{1}{2}\left[- \sum_{j=1}^{3} \frac{\partial^{F}}{\partial x_j} (E_j^n) - \sum_{j=1}^{3} \frac{\partial^{B}}{\partial x_j} (\overline{E_j^{n+1}}) \right] - (1-\phi)\, H^n - \phi H^{n+1} \tag{2.15a}$$

then

$$\left(\frac{\partial F}{\partial U}\right)^{(\ell)} [U^{(\ell+1)} - U^{(\ell)}] = - F^{(\ell)} \qquad (\ell) = 0,1,2... \tag{2.15b}$$

where superscript (ℓ) indicates evaluation using the ℓ^{th} iteration approximation of U^{n+1} and

$$\left(\frac{\partial F}{\partial U}\right)^{(\ell)} = \frac{1}{\Delta t} I - \phi \left(\frac{\partial H}{\partial U}\right)^{(\ell)} \tag{2.15c}$$

Combining Eqs. (2.15) yields

$$\left\{ I - \phi \Delta t \left(\frac{\partial H}{\partial U}\right)^{(\ell)} \right\} \left[\frac{U^{(\ell+1)} - U^{(\ell)}}{\Delta t}\right] = - \left[\frac{U^{(\ell)} - U^{n}}{\Delta t}\right] + \frac{1}{2}\left[- \sum_{j=1}^{3} \frac{\partial^{F}}{\partial x_j} (E_j^n) - \sum_{j=1}^{3} \frac{\partial^{B}}{\partial x_j} (\overline{E_j^{n+1}}) \right.$$

$$+ (1 - \phi)\, H^n + \phi H^{(\ell)} \tag{2.16}$$

where I is the identity matrix and $(\partial H/\partial U)$ is the Jacobian matrix associated with the H vector. Equation (2.16) is a system of N equations which must be solved at each node in the flow field for the quantity

$$\left[\frac{U^{(\ell+1)} - U^{(\ell)}}{\Delta t}\right]$$

The values of $U^{(\ell+1)}$ are given by

$$U^{(\ell+1)} = U^{(\ell)} + \Delta t \left[\frac{U^{(\ell+1)} - U^{(\ell)}}{\Delta t}\right] \tag{2.17}$$

Equations (2.16) and (2.17) are iterated on ℓ beginning with $U^{(1)} = U^{(0)} = U^n$ until the difference $U^{(\ell+1)} - U^{(\ell)}$ becomes negligible, at which time $U^{n+1} = U^{(\ell+1)}$.

2.3.4 Decode Procedures

After obtaining the conserved variables at the new time level from Eqs. (2.7) and (2.8) plus Eqs. (2.9) through (2.11), the primitive variables ρ, u_1, u_2, u_3, $\mathcal{E}$, c_i, p, and T must be decoded. From the definition of U given in Eq. (2.6b) it can be seen that most of the primitive variables can be obtained simply by dividing U by ρ. However, a more complex relationship exists between p, T, $\mathcal{E}$, and c_i so that a special decode procedure must be devised in order to obtain p and T. This decode procedure as applied in the GIM code is given as follows

Given: ρ, u_1, u_2, u_3, $\mathcal{E}$, and c_i $i = N$ after each step

Find: p,T

$$\text{Set} \quad h_{specie}(T) - h_{flowfield}(T) = 0 \tag{2.18a}$$

where

$$h_{specie}(T) = \sum_{i=1}^{N} c_i \left\{ h_{o_i} + \int_{T_o}^{T} c_{p_i}(\xi)\, d\xi + h_{f_i} \right\} \tag{2.18b}$$

$$h_{\text{flow field}}(T) = \mathcal{E} - \frac{1}{2} q^2 + \frac{p}{\rho} = \mathcal{E} - \frac{1}{2} q^2 + RT \tag{2.18c}$$

and solve implicitly for T and then $p = \rho\ RT$.

To solve Eq. (2.18) directly, define $h_i(T)$

$$h_i(T) \equiv h_{o_i} + \int_{T_o}^{T} c_{p_i}(\xi)\, d\xi + h_{F_i}$$

so that Eq. (2.18) becomes

$$\sum_{i=1}^{N} c_i\, h_i(T) - \mathcal{E} + \frac{1}{2} q^2 - RT = 0$$

or

$$\sum_{i=1}^{N} c_i \left\{ h_i(T) - \frac{\Re T}{m_i} \right\} - \mathcal{E} + \frac{1}{2} q^2 = 0\ , \tag{2.19}$$

With the value of the function $h_i(T)$ available at J discrete temperature abscissa, i.e.,

$$h_i(T_j) = h_{i,j} \quad \text{for} \quad T_j = (j-1)\,\Delta T \quad j = 1,J$$

the value of the function at any temperature point in the range $T_1 \leq T \leq T_J$ can be represented by a second order Lagrangian interpolation polynomial, i.e.,

$$h_i(T) = \left[\frac{(T - T_j)\,(T - T_{j+1})}{(T_{j-1} - T_j)\,(T_{j-1} - T_{j+1})}\right] h_{i,j-1} + \left[\frac{(T - T_{j-1})\,(T - T_{j+1})}{(T_j - T_{j-1})\,(T_j - T_{j+1})}\right] h_{i,j}$$

$$+ \left[\frac{(T - T_{j-1})\,(T - T_j)}{(T_{j+1} - T_{j-1})\,(T_{j+1} - T_j)}\right] h_{i,j+1}$$

where j is selected such that

$$|T - T_j| \leq \Delta T \qquad j = 2, \ldots, J-1$$

This can be further simplified using the constant ΔT assumption:

$$h_i(T) = \frac{1}{2} \left[\frac{T}{\Delta t} - (j-1)\right] \left[\frac{T}{\Delta T} - j\right] h_{i,j-1} - \left[\frac{T}{\Delta T} - (j-2)\right] \left[\frac{T}{\Delta T} - j\right] h_{i,j}$$

$$+ \frac{1}{2} \left[\frac{T}{\Delta T} - (j-2)\right] \left[\frac{T}{\Delta T} - (j-1)\right] h_{i,j+1}$$

$$= \left[\frac{1}{2} h_{i,j-1} - h_{i,j} + \frac{1}{2} h_{i,j+1}\right] \left(\frac{T}{\Delta T}\right)^2$$

$$+ \left[-\frac{1}{2} (2j-1) h_{i,j-1} + (2j-2) h_{i,j} - \frac{1}{2} (2j-3) h_{i,j+1}\right] \left(\frac{T}{\Delta T}\right)$$

$$+ \left[\frac{1}{2} j (j-1) h_{i,j-1} - j(j-2) h_{i,j} + \frac{1}{2} (j-1)(j-2) h_{i,j+1}\right]$$

Substituting this expression into Eq. (2.19) yields

$$\left\{\sum_{i=1}^{N} c_i \left[\frac{1}{2} h_{i,j-1} - h_{i,j} + \frac{1}{2} h_{i,j+1}\right]\right\} \left(\frac{T}{\Delta T}\right)^2$$

$$- \left\{\sum_{i=1}^{N} c_i \left[\frac{1}{2} (2\,j-1) h_{i,j-1} - (2\,j-2) h_{i,j} + \frac{1}{2} (2\,j-3) h_{i,j+1} + \frac{\mathfrak{R}\,\Delta T}{\bar{m}_i}\right]\right\} \left(\frac{T}{\Delta T}\right) \qquad (2.20)$$

$$+ \left\{\sum_{i=1}^{N} c_i \left[\frac{1}{2} j(j-1) h_{i,j-1} - j(j-2) h_{i,j} + \frac{1}{2} (j-1)(j-2) h_{i,j+1}\right] - \mathcal{E} + \frac{1}{2} q^2\right\} = 0$$

Equation (2.20) is a simple quadratic equation in (T/ΔT) of the form

$$A \left(\frac{T}{\Delta T}\right)^2 - B \left(\frac{T}{\Delta T}\right) + C = 0 \qquad (2.21a)$$

with the solution given by

where

$$\left(\frac{T}{\Delta T}\right) = \frac{B + \sqrt{B^2 - 4\ AC}}{2A} \qquad (2.21b)$$

$$A = \sum_{i=1}^{N} c_i \left[\frac{1}{2}\, h_{i,j-1} - h_{i,j} + \frac{1}{2}\, h_{i,j+1}\right] \qquad (2.21c)$$

$$B = \sum_{i=1}^{N} c_i \left[\frac{1}{2}\,(2j-1)\, h_{i,j-1} - (2j-2)\, h_{i,j} + \frac{1}{2}\,(2j-3)\, h_{i,j+1} + \frac{R\Delta T}{\bar{m}_i}\right] \qquad (2.21d)$$

$$C = \sum_{i=1}^{N} c_i \left[\frac{1}{2}\, j(j-1)\, h_{i,j-1} - j(j-2)\, h_{i,j} + \frac{1}{2}\,(j-1)\,(j-2)\, h_{i,j+1}\right] - \mathcal{E} + \frac{1}{2}\, q^2 \qquad (2.21e)$$

$$T = \Delta T \left(\frac{T}{\Delta T}\right) \quad \text{and} \quad p = \rho RT = \rho T \mathfrak{R} \sum_{i=1}^{N} \frac{c_i}{\bar{m}_i} \qquad (2.22)$$

2.3.5 Vectorization Procedures

As stated earlier, all of the GIM code chemistry procedures are highly vectorized so as to obtain maximum computational efficiency on the CYBER 200 series of supercomputers. This is true for the production and rate Eqs. (2.4b) through (2.4g); the explicit and implicit integration Eqs. (2.7) through (2.11), (2.12) through (2.14), and (2.15) through (2.17); and the decode procedure Eqs. (2.18) through (2.22). The solution of the implicit chemistry Eqs. (2.16) which involves N simultaneous equations at each node in the flow field is also vectorized. This is possible because of the algebraic form of the production term H with the result that Eq. (2.16) contains unknown values only at the node of interest and does not involve terms at any other node in the flow field. Therefore, if there are NN nodes in the flow field under consideration, there will be NN systems of N simultaneous equations to solve each system of which is independent of all other systems but identical in form. Since the same sequence of mathematical operations must be applied to each of the NN systems of equations in order to solve them, this sequence of operations can be applied once to vector descriptors pointing to corresponding entries in the NN coefficient matrices and right-hand side, as opposed to applying the same sequence to each of the NN systems. These alternatives are illustrated below:

Let Eq. (2.16) be represented as

$$M \mathcal{U} = \text{RHS} \tag{2.23a}$$

where

$$M = I - \phi \Delta t \left(\frac{\partial H}{\partial U}\right)^{(\ell)} \qquad \mathcal{U} = \frac{U^{(\ell+1)} - U^{(\ell)}}{\Delta t}$$

$$\text{RHS} = -\left[\frac{U^{(\ell)} - U^{n}}{\Delta t}\right] + \frac{1}{2}\left[- \sum_{j=1}^{3} \frac{\partial^{F}}{\partial x_j} (E_j^n) - \sum_{j=1}^{3} \frac{\partial^{B}}{\partial x_j} (\overline{E_j^{n+1}})\right] + (1-\phi)\, H^n + \phi H^{(\ell)} \tag{2.23b}$$

Vectorized Approach

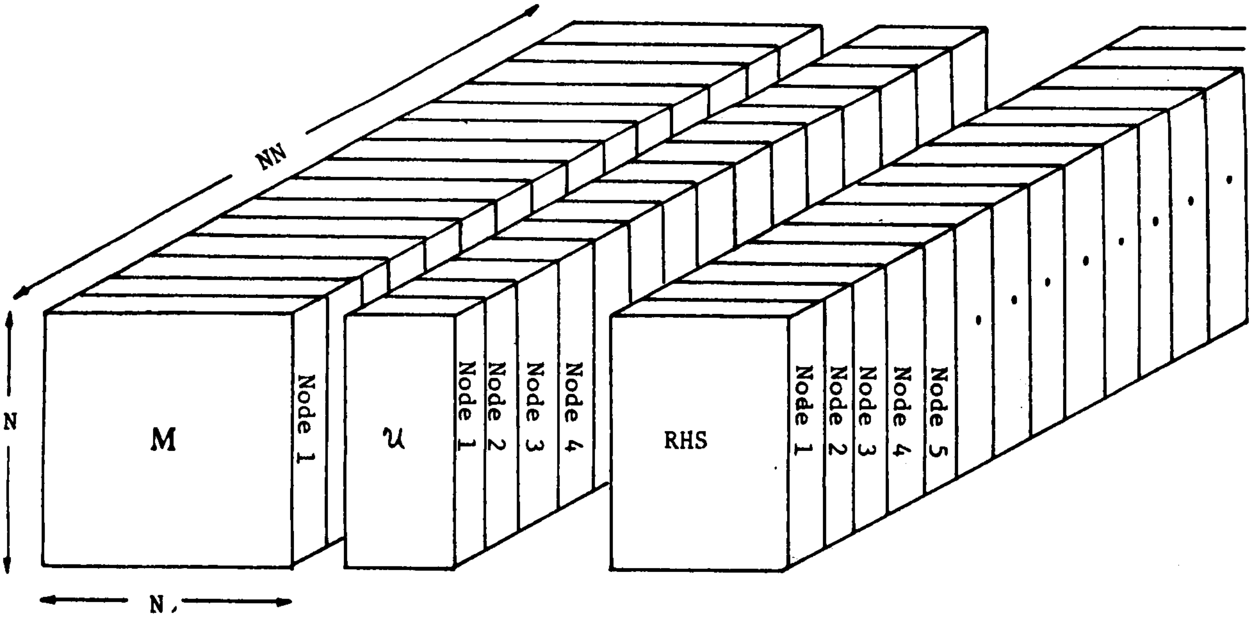

Scalar Approach

$$\boxed{M_1} \times \boxed{\mathcal{U}_1} = \boxed{RHS_1} \quad \bullet \quad \bullet \quad \bullet \quad \bullet \quad \bullet \quad \boxed{M_{NN}} \times \boxed{\mathcal{U}_{NN}} = \boxed{RHS_{NN}}$$

2.3.6 Artificial Numerical Diffusion

Limited experience has indicated that some form of artificial numerical diffusion or viscosity must be introduced into the species continuity equations (2.4a) to keep the solution smooth and physically consistent. This is particularly so in region of large concentration gradients on course computational grids. The form for this artificial numerical diffusion term was developed following the motivation of McRae, Goodin, and Seinfeld (Ref. 2-2) and Forester (Ref. 2-3). The form consists of a simple second order diffusion-like term with a variable coefficient that responds to species gradients:

$$\sum_{j=1}^{3} \frac{\partial}{\partial x_j}\left[-\varepsilon\left|\frac{\Delta c_i}{c_i}\right|(\rho\, u_j\, \Delta x_j)\,\frac{\partial c_i}{\partial x_j}\right] \qquad (2.24)$$

where

ε = a global coefficient of 0(1);

Δc_i = $\Delta x_j \dfrac{\partial c_i}{\partial x_j}$, so that $\left|\dfrac{\Delta c_i}{\Delta c_i}\right|$ is a normalized gradient-sensitive coefficient; and

$(\rho\, u_j\, \Delta x_j)$ = coefficient for consistency with convection terms.

This artificial numerical diffusion is incorporated into the species continuity Eqs. (2.4a) through the diffusion coefficient $\mathscr{D}_j$:

$$\mathcal{D}_j = \mathcal{D}_r + \mathcal{D}_{d_j}$$

where

$\mathcal{D}_r$ = real diffusion coefficient

$\mathcal{D}_{d_j}$ = artificial diffusion coefficient

$$= \varepsilon \left| \frac{\Delta c_i}{c_i} \right| u_j \, \Delta x_j$$

2.4 FROZEN FLOW AND EQUILIBRIUM FLOW MODELS

2.4.1 Reaction Rate Limits

Frozen flow and equilibrium flow are by definition the flow produced in the limit as the reaction rates become respectively infinitesimally small and infinitely large. Since the reaction rates appear explicitly only in the species continuity Eqs. (2.4a) via the production term $\dot{w}_i$, the frozen flow and equilibrium flow limits can be obtained by considering the effect on these equations as the reaction rates become infinitesimally small and infinitely large.

Substituting Eqs. (2.4e) into Eq. (2.4b) yields

$$\dot{w}_i = \sum_{j=1}^{M} \Delta \nu_{ij} \, k_{f_j} \left[\prod_{\ell=1}^{N} \left(\frac{\rho \, c_\ell}{\bar{m}_\ell} \right)^{\nu'_{\ell j}} - \frac{1}{K_{c_j}} \prod_{\ell=1}^{N} \left(\frac{\rho \, c_\ell}{\bar{m}_\ell} \right)^{\nu''_{\ell j}} \right] \qquad (2.25a)$$

$$= \sum_{j=1}^{M} \Delta \nu_{ij} \, k_{f_j} \, X_j$$

where

$$X_j \equiv \left[\prod_{\ell=1}^{N} \left(\frac{\rho\, c_\ell}{\bar{m}_\ell} \right)^{\nu'_{\ell j}} - \frac{1}{K_{c_j}} \prod_{i=1}^{N} \left(\frac{\rho\, c_\ell}{\bar{m}_\ell} \right)^{\nu''_{\ell j}} \right] \qquad (2.25b)$$

Then substituting Eq. (2.25) into the species continuity Eqs. (2.6) yields

$$\frac{\partial U}{\partial t} + \sum_{j=1}^{3} \frac{\partial E_j}{\partial x_j} - \sum_{j=1}^{M} \Delta\, \nu_{ij}\, k_{f_j}\, X_j = 0 \qquad (2.26)$$

from which the frozen flow and equilibrium flow limits can be determined.

2.4.2 Frozen Flow

In the frozen flow limit as the reaction rates become infinitesimally small the effect of chemical production becomes negligible so that convection and diffusion dominate the time rate of change of the species concentrations. In this limit the species continuity Eqs. (2.26) become

$$\frac{\partial U}{\partial t} + \sum_{j=1}^{3} \frac{\partial E_j}{\partial x_j} = 0 \qquad \text{(Frozen Flow)} \qquad (2.27)$$

Since $\dot{w} = 0$ and hence $H = 0$, the chemistry step of the differencing scheme, Eq. (2.11), is superfluous and is not used.

2.4.3 Equilibrium Flow

The equilibrium flow limit can be obtained by dividing Eq. (2.26) by each k_{f_j}, one at a time, and allowing k_{f_j} to become infinitely large. This limiting process applied for the M different k_{f_j}'s yields

$$X_j = 0 \qquad j=1,2,\ldots,M \tag{2.28a}$$

from which

$$\dot{w}_i = H = 0 \tag{2.28b}$$

which is the steady state equilibrium flow limit.

In order to obtain this steady state limit, the unsteady term in Eq. (2.26) is retained. Furthermore, for stability considerations, the artificial numerical diffusion term is also retained. Thus the equilibrium flow limit of the species continuity equations as used in the GIM code is given by Eqs. (2.6) with the convection terms omitted, i.e.,

$$\frac{\partial}{\partial t}(\rho\, c_i) + \sum_{j=1}^{3} \frac{\partial}{\partial x_j}\left(-\rho\, \mathscr{D}_{d_j} \frac{\partial c_i}{\partial x_j}\right) - \bar{m}_i\, \dot{w}_i = 0 \qquad i=1,N \qquad \text{(Equilibrium Flow)} \tag{2.29}$$

This limiting form of the species continuity equations allows the equilibrium solution to be obtained wherein the chemical production dominates the time rate of change of the species concentrations with convection and real diffusion being negligible.

2.5 INPUT GUIDE

2.5.1 General

The GIM code chemically reacting flow model consists of a set of UPDATE directives and code to be used with the INTEG integration module and the DYNDIM dynamic dimensioning module. These UPDATE directives are located on a semi-private file named CHEMOD on user number 838700C. CHEMOD contains two logical records. The first record contains the UPDATE directives for the INTEG integration module; the second contains the UPDATE directives for the DYNDIM dynamic dimensioning module. Both sets must be used with their respecitve modules in order to generate the GIM code chemically reacting flow model.

2.5.2 NOS Side Runstream Information

Figure 2-1 illustrates a typical NOS "front-side" or "Z-machine" runstream for use with the GIM code chemically reacting flow model.

2.5.3 CYBER 203 Runstream Information

Figure 2-2 illustrates a typical CYBER 203 runstream for use with the GIM code chemically reacting flow model.

2.5.4 Dynamic Dimensioning Input Data Summary

The GIM code chemically reacting flow model requires dynamic dimensioning input data that differ somewhat from that normally associated with INTEG. This section presents a summary of these data and a brief description of each input variable.

The dynamic dimensioning data for the GIM code chemically reacting flow model are input on one card in a 9I5 integer format. The integers are always right justified in five colume increments. The input variables are:

MN,IDIM,NSPEC,NREAC,NCATS,NSP,MNB,METHOD,IDYN

MN

The total number of nodes in the problem (elliptic run) or the number of nodes in the initial cross plane (quasi-parabolic run).

```
/JOB
/NOSEQ
RUNCHM,CM60000,T400.
USER(750978C,PASWRD)
CHARGE(0123456,LRC)
GET(OLDPL=INTEG,CHEMOD/UN=838700C)
UPDATE(F,C=TAPE8,L=A12)
RETURN(OLDPL)
GET(OLDPL=UTILOPL/UN=838700C)
UPDATE(I=CHEMOD)
FTN(I=COMPILE,B=DYNDIM,L=0,A)
MAP(OFF)
DYNDIM.
RENAME(INTGS=TAPE3)
RETURN(OLDPL,DYNDIM,CHEMOD,TAPE8,COMPILE)
ATTACH(FILE20)
ATTACH(FILE17  or  FILE21)
TOSTAR(INPUT,INTGS,FILE20,FILE17=BI  or  FILE21=BI)
DAYFILE(NOSDAY)
REPLACE(NOSDAY)
EXIT.
DAYFILE(NOSDAY)
REPLACE(NOSDAY)
EXIT.
/EOR
*READ,CHEMOD

                    Any other UPDATE Directives

/EOR
6534    2    5    2    0    329    326    2    0
/EOR
```

Fig. 2-1 - NOS Runstream

```
STORE 750978 400SDS RUNCHM           B
STRSIDE,T500.
REQUEST(FILE22/2000)
REQUEST(JANAF/2000)
FORTRAN(I=INTGS,B=INTGB/300,L=ERRFTN,OPT=B)
LOAD(INTGB,OU=ERRLOD,CN=INTEGO,4000,CDF=5000
,GRLP=*TMVEC,*PRIM,*EBUF,*VPROP,GRLP=*UBUF,*BOUND,*DELXYZ,*AXSYM
,GRLP=*XBUF1,GRLP=*XBUF2,GRLP=*TAUP,*TAU,*TAUF,*QPNOD,*SECORD
,GRSP=*IOUNIT,*CNTRL,*TRANSP,*TDATA,*VECP,*SQ,*PM,*SUBSBC,*USER
,MZONE,*QPCOM,*QPPRNT,*CVGCOM,*CHEM,*THERMO
,GROL=*Q3MAP)
INTEGO.
TOS(Z=750978C,FILE22,JANAF)
DAYFILE(STRDAY)
EXIT.
TOAS(Z=750978C,ERRFTN,ERRLOD,FILE22,JANAF)
DAYFILE(STRDAY)
EXIT.
/EOR

            INTEG Input Data

            Chemically reacting flow model input data

/EOR
```

Fig. 2-2 - CYBER 203 Runstream

IDIM

The spatial dimension of the problem.

IDIM = 1 axisymmetric flow
= 2 two-dimensional flow
= 3 three-dimensional flow

NSPEC

The number of reactive chemical species in the problem.

NREAC

The number of chemical reaction mechanisms (equations) considered.

NCATS

The number of nonreacting catalytic or "third-body" species.

NSP

The number of special node terms.

MNB

The number of boundary node terms.

METHOD

Elliptic/Quasi-Parabolic flag.

METHOD ≤ 2 Elliptic run
> 2 Quasi-Parabolic run

IDYN

Dynamic assembly flag.

IDYN	= 0	Regular GIM code run
	≠ 0	Dynamic assembly GIM code run

2.5.5 Input Card Summary

The GIM code chemically reacting flow model requires some chemistry input data in addition to and immediately following the normal INTEG integration input data. This section presents a summary of the input cards and formats used to input this chemistry data. A description of each input variable and its options is presented in Section 2.5.6. After a user becomes familiar with the chemistry inputs, this summarized input guide can be used to quickly identify each card and its contents.

Several formats are used to input the chemistry data to the GIM code chemically reacting flow model. These include:

ALPHANUMERIC	A1, A6, and A8
INTEGER	I1 and I5
REAL	F5.0 and E10.0

Integers are always right justified in one or five column increments. Decimal or floating point data occupy five or ten columns each with, preferably, a decimal point punched on the card.

The GIM code chemically reacting flow model is activated by selecting the appropriate value for the INTEG input variable ISPEC (see Ref. 2-4) as follows:

ISPEC = 0 regular GIM code single gas calculation (no chemistry)

= 1 frozen flow calculation

= 2 equilibrium flow calculation

= 3 nonequilibrium finite rate reaction calculation

For ISPEC > 0, the input data shown on the following page must be provided:

CARD TYPE	VARIABLE LIST/FORMAT	
C1	NSPEC, NRSPC, NREAC, NCATS, NTIP, ITCHEM, ISTIFF, IXOPT, IOPT, IMOLE, ICHUN (11I5)	
C2	CSTOL(I), I=1,5 (5E10.0)	
C3	CPCF, HCF, SCF, RRCF (LCONV(I), I=1,4) (4E210.0,4A8)	
C4	{ LSPID(I), WM(I), HFM(I) (A6,4X,2E10.0)	} I=1,NSPEC
C5	[TIP(J), (CPHS(J,K,I),K=1,3), TIP(J+1), (CPHS(J+1,K,I),K=1,3] J=1,NTIP,2 (8E10.0) }	
C6	{ LSPID(I+NSPEC) (A6)	} I=1,NCATS
C7	WFM(I,J), J=1,NSPEC (16F5.0) }	
C8	[(RTYPE(I,J),I=1,2), (LREAC(I),I=1,78)] (2I1,78A1)	J=1,NREAC
C9	[(RRATC(I,K,J),I=1,5] K=1,1 or 2 (5E10.0)	J=1,NREAC
C10	{ NJ, INC, NTOT, ITYPE (4I5)	}
C11	CS(I), I=1,NSPEC (8E10.0) }	

[ ] denotes card is repeated one or more times as indicated.

{ } denotes card group is repeated one or more times as indicated.

2.5.6 Description of Input Data

This section presents a description of the input variables listed in Section 2.5.5. Each variable is identified as to its usage in the GIM code chemially reacting flow model with options and standard values also given. All 11 card types are not necessarily input for a given problem. Some of the control variables on card type C1, for example, dictate which options have been selected and hence which input cards are required. This information is given in the discussion of each variable to be input. Each input card which is read is also printed out to aid the user in debugging a problem setup.

CARD TYPE C1 - Chemistry Control Variables

FORMAT (8I5)

NSPEC

The total number of independent chemical species in the problem being run.

$$NSPEC \geq 1$$

Any number of species may be considered in a given problem, subject only to the limitations of storage and run time (CRUs) available. A value of NSPEC less than 1 is an error and terminates the run immediately.

NRSPC

The number of reactive chemical species (as opposed to inert species) in the problem being run.

$$1 \leq NRSPC \leq NSPEC$$

NRSPC should in general be set equal to NSPEC. However, if inert chemical species are present, then setting NRSPC less than NSPEC can save substantial amounts of computational resources.

NREAC

The number of chemical reaction mechanisms (equations) considered.

NREAC	≥ 1	chemically reacting flow
	≤ 0	frozen flow (no reactions)

Any number of reactions may be considered in a given problem, again subject only to the limitations of storage and run time.

NCATS

The number of nonreacting catalytic or "third-body" species.

$$\mathrm{NCATS} \geq 0$$

Any number of catalytic species may be included in a given problem.

NTIP

The number of thermodynamic interpolation points in the species thermodynamic data tables. The user must input a set of thermodynamic data tables for each of the NSPEC chemical species in the problem. These tables consist of the specific heat at constant pressure, sensible enthalpy, and entropy at each of NTIP temperature points. These data can either be read in as input or can be read from a previously created coded file named JANAF, depending on the sign of NTIP.

NTIP > 0	read data from input
NTIP < 0	read data from JANAF file

If NTIP is greater than 0, the JANAF file is automatically created for use on the next run. A value of NTIP equal to 0 is an error and terminates the run immediately.

ITCHEM

This variable controls frequency of the calls to the chemistry routines. The chemistry routines are called every ITCHEMth iteration (time step). Generally, for frozen flow (ISPEC = 1) or nonequilibrium flow (ISPEC = 3) ITCHEM should be set to 1 so that the chemistry routines are called on every iteration. For equilibrium flow (ISPEC = 2) or for flows where the chemistry is near steady state ITCHEM can be set to larger values. A value of ITCHEM equal to 0 deactivates the chemistry routines so that they are never called. In this case the species distributions will remain at their initial values.

ISTIFF

Stiff Chemistry Equation Option. If the magnitude of the species production term, $\dot{w}$ (and hence H), becomes large, a numerical solution of the species continuity equations can be difficult to obtain for all but the smallest of time steps. In order to overcome this severe time step restriction, the parameter ϕ can be adjusted toward a value of 1.0. This renders the treatment of the chemistry terms more implicit and easier to solve for larger time steps at the expense of losing second order accurte tracking of the transient behavior. Control of the parameter ϕ is selected via ISTIFF.

ISTIFF = 0	nonstiff equations; $\phi = 0.5$ for second order accurate trapezoidal-like integration of chemistry production terms.
= 1	stiff equations; $0.5 \leq \phi \leq 1.0$, calculated internally so that chemistry production terms are treated more implicitly as $|\dot{w}|$ increases.

IXOPT

Implicit/explicit chemistry integration option. The user can select the implicit chemistry solution technique, the explicit chemistry solution technique or a combination of the two through the use of IXOPT:

IXOPT = 1 explicit chemistry solution technique
= 0 implicit/explicit chemistry solution technique
= -1 implicit chemistry solution technique

If the user selects the combined explicit/implicit chemistry solution technique (IXOPT = 0), the program determines which technique to use on each time step based on the maximum local change of the species concentrations and the CSTOL tolerances (card type C2). Frozen flow (ISPEC = 1) automatically selects IXOPT = 1 for the explicit technique only.

IOPT

Chemical species output option. The user can select the type of chemical species data to be output with the usual flowfield data via IOPT:

IOPT = 0 flow field only; no chemistry data

= 1 flow field + species mass (or mole) fractions

= 2 flow field + species mass (or mole) fractions + species production rates

IMOLE

Mole fraction/mass fraction option. The GIM code chemically reacting flow model inputs and outputs the species concentrations in terms of mass fraction (by default). Input and output in terms of mole fractions can be selected using IMOLE as indicated below:

IMOLE	= 0	input and output in mass fractions
	= 1	input and output in mole fractions

ICHUN

Chemistry data units and unit conversion option. The GIM code chemically reacting flow model requires a variety of chemical information to describe the reactions and species involved. More often than not, these data as taken from JANAF tables, experimental calculations, and other sources is not in the correct set of units for use in the integrator module. Converting the data by hand before using it as input to the integration module can be tedious and time consuming. By selecting the appropriate ICHUN options and in conjunction with the conversion factors specified on card type C3, the user can input chemistry data in whatever units are convenient and allow the program to perform all data conversion calculations.

The initial value of ICHUN is 0 indicating no internal chemistry data conversion. The various ICHUN options can then be selected in any combination by adding the following values to ICHUN:

ICHUN	= 0	no chemistry data conversion; chemistry data used as input to the program
	+ 1	general chemistry data conversion; appropriate data items are multiplied by user specified conversion factors (see card type C3)
	+ 2	per mole to per unit mass conversion; appropriate data items are divided by species molecular weight (Note: All GIM code chemically reacting flow model calculations are performed internally on a per unit mass basis. Therefore, all chemistry data must be either input on that basis or converted to that basis.)
	+ 4	reaction rate per particle to per mole conversion; appropriate reaction rate data are multiplied by Avogadro's number

In addition to the value input for ICHUN, the sign of ICHUN also has significance. If ICHUN is input as a positive number, the chemistry data is printed out as input before any data conversion. If ICHUN is input as a negative number, the chemistry data are printed out both as input before data conversion and then again after data conversion has occurred.

CARD TYPE C2 - Chemistry Control Tolerances

FORMAT (4E10.0)

Note: Card type C2 may be left blank if desired in which case the indicated nominal values will be used for CSTOL(1-4).

CSTOL(1) (Nominal value = 1.0E-4)

Trace species tolerance. Species whose mass fraction falls below the specified value of CSTOL(1) at any node in the flow field are considered to be trace species at that node. Trace species are included in all chemistry calculations but are not included in algorithmic decisions in the chemistry subroutines.

CSTOL(2) (Nominal value = 0.10)

Explicit-to-implicit chemistry integration tolerance. If IXOPT is input as 0, the chemistry routines can switch from explicit integration of the species continuity equations to implicit integration. CSTOL(2) controls the point at which the switch is made. After each explicit chemistry integration step, the following criteria is examined:

$$\mathrm{MAX}\left|\frac{\Delta c_i}{c_i}\right| > \mathrm{CSTOL(2)} \qquad \begin{array}{l} \text{for all } c_i > \mathrm{CSTOL(1)} \\ i=1,\ \mathrm{NSPEC} \end{array}$$

If the criteria are satistied, then the switch is made from explicit chemistry integration to implicit chemistry integration on the next time step.

If the criteria are not satisfied, then the program continues to use explicit chemistry integration. If IXOPT is not input as 0, then no switching of chemistry integration scheme is possible and the value of CSTOL(2) is irrelevant.

CSTOL(3) (Nominal value = 1.0E-10)

Implicit-to-explicit chemistry integration tolerance. If IXOPT is input at 0, the chemistry routines can switch from implicit integration of the species continuity equations to explicit integration. CSTOL(3) controls the point at which the switch is made. Before each implicit chemistry integration step (immediately following the explicit provisional step), the following criteria are examined:

$$\mathrm{MAX}\left|\frac{\Delta c_i}{c_i}\right| < \mathrm{CSTOL(3)} \qquad \text{for all } c_i > \mathrm{CSTOL(1)}$$
$$i=1,\ \mathrm{NRSPC}$$

If the criteria are satisfied, then the switch is made from implicit chemistry integration to explicit chemistry integration on the next time step. If the criteria are not satisfied, then the program continues to use implicit chemistry integration. Care must be exercised in selecting a value for CSTOL(3), particularly for equilibrium and nonequilibrium flows. If the value of CSTOL(3) is too large, the program may switch from implicit chemistry integration to explicit chemistry integration while the species production terms are still quite active. This will result in numerical instability (time step criteria violation) and the calculation will "blow up." In flows with particularly violent reactions, a very small value for CSTOL(3) is recommended in order to avoid this difficulty, e.g.,

$$\mathrm{CSTOL(3)} = 1.0\mathrm{E}{-10}$$

If IXOPT is not input as 0, then no switching of chemistry integration scheme if possible and the value of CSTOL(3) is irrelevant.

CSTOL(4) (Nominal value = 1.0)

Chemistry iteration cutoff tolerance. During chemistry integration, the chemistry Eqs. (2.13) or (2.16) are solved iteratively using the method of successive substitutions or the Newton-Raphson method, respectively. These equations are iterated until the difference between successive iterates satisfies the following criteria:

$$\mathrm{MAX}\left|\frac{U_i^{(\ell+1)} - U_i^{(\ell)}}{U_i^{(\ell+1)}}\right| \leq \mathrm{CSTOL}(4) \qquad \begin{array}{l}\text{for all } c_i > \mathrm{CSTOL}(1) \\ i=1,\mathrm{NSPEC}\end{array}$$

Limited experience has demonstrated that one iteration is usually sufficient to ensure numerical stability. Additional iterations are costly and not useful unless an accurate time transient is sought or unless the equations are stiff. Therefore, if only the steady state solution is desired and if the equations are not particularly stiff, CSTOL(4) should be set to a large value (~1.0) so that the implicit chemistry routine will make only one iteration per time step. If CSTOL(4) is set to a lower value, more iterations will be made on each time step but under no circumstances will more than 10 iterations be made

CSTOL(5) (Nominal value = 0.10)

Chemistry Jacobian Matrix Update Tolerance. During chemistry integration when Eqs. (2.13) or (2.16) are being solved iteratively, the Jacobian matrix ($\partial H/\partial U$) can be calculated only once at the beginning of the iteration process or recalculated on every iteration. The former approach is computationally much less expensive than the latter but is not acceptable if the equations are stiff ($\partial H/\partial U$ changing rapidly as a function of U). CSTOL(5) establishes the criteria to select which approach to use. If ISTIFF≠0, the following criteria is examined:

$$\mathrm{MIN}\left|\frac{(\text{Convection + Diffusion Terms})_i}{(\text{Species Production Terms})_i}\right| < \mathrm{CSTOL}(5) \quad i=1,\mathrm{NRSPC}$$

If the criteria are satisfied, the equations are assumed to be stiff and the Jacobian matrix is recalculated on every iteration. If the criteria is not satisfied or if ISTIFF=0, the equations are assumed to be non-stiff and the Jacobian matrix is calculated only once at the beginning of the iteration process.

CARD TYPE C3 - Thermodynamic Conversion Factors

FORMAT (4E10.0,4A8)

Notes:
1. Input card type C3 only if MOD(CHUN ,2) = 0.
2. If card type C3 is omitted (see #1) or left blank, CPCF, HCF, SCF, and RRCF will be set to 1.0 internally and LCONV will be blanked.
3. CPCF, HCF, and SCF sould not be used to convert from a per mole to a per mass basis. Use the ICHUN option for this purpose.

CPCF

Specific heat conversion factor. CPCF should be set equal to the factor required to convert specific heat data from input units to the proper integrator module units ($ft^2\ sec^{-2}\ {}^oR^{-1}$ if IUNITS=1 or $cm^2\ sec^{-2}\ {}^oK^{-1}$ if IUNITS = 2). Each of the specific heat ordinates input on card type C5 or read from file JANAF will be multiplied by CPCF before use in the program.

Example: Specific heat data are taken from thermodynamic tables in units of cal/mole/^{o}K and IUNITS = 2.

CPCF should be set equal to 4.184×10^7 g cm^2 sec^{-2}/cal.

HCF

Enthalpy conversion factor. HCF should be set equal to the factor required to convert enthalpy data from input units to the proper integrator module units ($ft^2\ sec^{-2}$ if IUNITS = 1 or $cm^2\ sec^{-2}$ if IUNITS = 2). Each of the enthalpy ordinates input on card type C5 or read from file JANAF will be multiplied by HCF before use in the program.

Example: Enthalpy data are taken from thermodynamic tables in units of kcal/mole and IUNITS = 2.

HCF should be set equal to 4.184×10^{10} g $cm^2\ sec^{-2}$/kcal.

SCF

Entropy conversion factor. SCF should be set equal to the factor required to convert entropy data from input units to the proper integrator module units ($ft^2\ sec^{-2}\ {}^oR^{-1}$ if IUNITS = 1 or $cm^2\ sec^{-2}\ {}^oK^{-1}$ if IUNITS = 2). Each of the entropy ordinates input on card type C5 or read from file JANAF will be multiplied by SCF before use in the program.

Example: Entropy data are taken from thermodynamic tables in units of BTU/mole/^{o}R and IUNITS = 1.

SCF should be set equal to 2.5036×10^4 lbm $ft^2\ sec^{-2}$/BTU.

RRCF

Activation energy conversion factor. RRCF should be set equal to the factor required to convert activation energy data (card type C9) from input units to proper integrator module units ($ft^2\ sec^{-2}$ if IUNITS = 1 or $cm^2\ sec^{-2}$ if IUNITS = 2). Each of the reaction rate coefficients C_j input on card type C9 will be multiplied by RRCF before use in the program.

Example: Activation energy data are taken from thermodynamic tables in units of cal/mole and IUNITS = 1.

RRCF should be set equal to 9.9287×10^1 lbm $ft^2\ sec^{-2}$/cal.

LCONV

Conversion factor label. LCONV is a 4 word label which is used on the printout as a mnemonic device to describe the type of thermodynamic data conversions represented by the CPCF, HCF, SCF, and RRCF conversion factors. Any alphanumeric information can be used or LCONV can be left blasnk. LCONV is strictly a mnemonic device and in no way affects the calculations.

CARD TYPE C4 - Species Identification Label, Molecular Weight, and Heat of Formation

FORMAT (A6,4X,2E20.0)

Notes:

1. Input card types C4 and C5 only if NTIP > 0 on card C1.
2. For NTIP > 0, the input sequence is one card type C4 followed by several cards of type C5; then repeat the sequence NSPEC times, card C4 - then cards C5, card C4 - then cards C5, etc.
3. The number of cards of type C5 to be input after each card type C4 is equal to (NTIP-1)/2 + 1.
4. In the subsequent input description, the subscript I runs from 1 to NSPEC, indicating the sequence of NSPEC groups of cards type C4 and C5.

LSPID(I)

Species identification label for the I^{th} species. Any alphanumeric data up to six characters in length may be used. The explicit chemical formula for the species may be used but this is not required. For example, methane might be represented by either CH4 or MTHANE. Note however that whatever label is used for the I^{th} species in LSPID(I) must also be used on card type C8 to represent that species in any reaction mechanisms.

WM(I)

Molecular weight of the Ith species.

HFM(I)

Heat of formation of the Ith species. HFM(I) should be input in units consistent with the enthalpy ordinates input on card type C5. Like the enthalpy ordinates, HFM(I) will be multiplied by the HCF conversion factor if MOD(ICHUN,2) $\neq$ 0 and will be divided by WM(I) if MOD(ICHUN/2,2) $\neq$ 0.

CARD TYPE C5 - Species Thermodynamic Properties Data

FORMAT (8E10.0)

Notes

1. The number of cards of type C5 to be input (after each of the NSPEC card type C4) is equal to (NTIP-1)/2 + 1.
2. In the subsequent input description, the subscript J runs from 1 to NTIP (incremented by 2), indicating the sequence of NTIP thermodynamic abscissa and ordinate points for each of the NSPEC species.

TIP(J)

Temperature abscissa (Jth value). Note that TIP is not subscripted with the subscript I which implies that the same set of TIP must be input for each of the NSPEC species on card type C5. The NTIP values of TIP should span the range of temperatures expected over the entire flow field during the time integration. If the temperature at any node in the flow field exceeds the range of the TIP values during integration, an execution diagnostic message is printed and the calculation terminates (no extrapolation is performed). TIP values need not begin at zero degrees nor be equally spaced on input. However, TIP and its associated data ordinates will be extrapolated to zero degrees and interpolated to equally spaced abscissas internally before time integration begins. TIP should be input in unit of ^{o}R (IUNITS = 1) or ^{o}K (IUNITS = 2).

CPHS(J,K,I), K=1,3

Species thermodynamic data ordinates corresponding to the Jth temperature abscissa, TIP(J), for the Ith species. CPHS(J,K,I) data consist of the following items:

CPHS(J,1,I) = specific heat at constant pressure = $c_{p_i}(T_j)$

CPHS(J,2,I) = sensible enthalpy = $\int_{T_o}^{T_j} c_{p_i}(\xi)\, d\xi$

CPHS(J,3,I) = entropy = $s_i(T_j)$

The CPHS thermodynamic data ordinates for all species should be input in consistent units and are subject to data conversion via the CPCF, HCF, and SCF factors if MOD(ICHUN,2) $\neq$ 0 as well as per mole to per unit mass conversion if MOD(ICHUN/2,2) $\neq$ 0.

TIP(J+1

Temperature abscissa (J+1th value). See TIP(J) above.

CPHS(J+1,K,I), K=1,3

Species thermodynamic data ordinates (J+1th values). See CPHS(J,K,I) above.

CARD TYPE C6 - Catalytic Species Identification Label

FORMAT (A6)

Notes

1. Input card types C6 and C7 only if NCATS > 0 and NREAC > 0 on card C1.
2. For NCATS > 0, the input sequence is one card type C6 followed by one or more cards of type C7; then repeat the sequence NCATS times, card C6 - then cards C7, - then cards C7, etc.
3. The number of cards of type C7 to be input after each card type C6 is equal to (NCATS-1)/16 + 1.
4. In the subsequent input description, the subscript I runs from 1 to NCATS, indicating the sequence of NCATS groups of cards type C6 and C7.

LSPID(I+NSPEC)

Species identification label for the Ith catalytic species. Any alphanumeric data up to six characters in length may be used. The explicit chemical formula (if any) may be used, but this is not required. Note that whatever label is used for the Ith catalytic species in LSPID(I+NSPEC) must also be used on card type C8 to represent that catalytic species in any direction mechanism.

CARD TYPE C7 - Catalytic Species Weighting Factors

FORMAT (16F5.0)

Notes

1. The number of cards of type C7 to be input (after each of the NCATS card type C6) is equal to (NCATS-1)/16 + 1.
2. In the subsequent input description, the subscript J runs from 1 to NSPEC, indicating the NSPEC weighting factors for each of the NCATS catalytic species.

WFM(I,J)

Weighting factor for reactive species J associated with the Ith catalytic species. During reaction rate calculations, the presence of catalytic or "third-body" species is included as a fictitious mass fraction consisting of the weighted sum of the reactive species mass fractions. At each node in the flow field the Ith catalytic species mass fraction is determined as follows:

$$c_{cat_i} = \sum_{j=1}^{NSPEC} WFM_{ij} \cdot c_{reac_j}$$

No restrictions apply to the values of WFM(I,J).

CARD TYPE C8 - Reaction Mechanism Information

FORMAT (2I1, 78A1)

Notes

1. Input card type C8 only if NREAC > 0 on card C1.
2. For NREAC > 0, the input sequence is one card type C8 for each of the NREAC reactions under consideration.
3. In the subsequent input description, the subscript J runs from 1 to NREAC, indicating the sequence of NREAC cards of type C8.

RTYPE(I,J), I=1,2) (Type INTEGER variable)

Reaction rate constant type associated with reaction J. RTYPE(1,J) is associated with the forward reaction rate constant while RTYPE(2,J) is associated with the backward reaction rate constat. RTYPE values are selected depending on the algebraic form of the corresponding reaction rate constant calculation, as indicated below:

RTYPE = 0 $k = 0.0$ (no reaction - backward reaction only)

= 1 $k = A$ (constant)

= 2 $k = A(T-T_o)^B$

= 3 $k = A \exp(C/\Re/(T-T_o))$

= 4 $k = A(T-T_o)^B \exp(C/\Re/(T-T_o))$

= 5 $k = A(T-T_o)^B \exp(C/\Re/(T-T_o)^D)$

= 6 k = calculated from equilibrium constant (backward reaction only (Eqs. (2.4e) through (2.4g)).

Note that the value of RTYPE(I,J) must be in the following range:

$$1 \leq \text{RTYPE}(1,J) \leq 5$$
$$0 \leq \text{RTYPE}(2,J) \leq 6$$

LREAC(I), I=1,78

Reaction mechanism equation for reaction J. Each of the NREAC reactions should be input via LREAC on separate cards of type C8. Each equation can consist of up to 78 characters including blanks and must adhere to the following format:

SUM OF REACTANTS = SUM OF PRODUCTS

where each reactant and each product consists of an optional integer coefficient and a LSPID species identification label. If the optional integer coefficient is present, it must be separated from the LSPID labvel by an asterisk (*). Individual reactants and products are separated by a plus sign (+). In this format each reaction equation should resemble a FORTRAN-like expression, e.g.,

```
H2 + O2 = OH + OH
2 * H2O = 2 * OH + H2
```

As explained above, the characters *, +, and = have special significance and should only be used to delimit coefficient and species (*), different species (+), and reactants and products (=). In particular, these three special characters should not be used in any fashion in either the reactive species identification label (LSPID) on card type C4 or the catalytic species identification label on card type C6. Blanks are not significant and may be used for spacing as desired.

CARD TYPE C9 - Reaction Rate Coefficients

FORMAT (5E10.0)

1. Input card type C9 only if NREAC > 0 on card type C1.
2. For NREAC > 0, the input sequence consists of one or two cards of type C9 for each of the NREAC reactions under consideration. One card is always input; the second card is input only if RTYPE(2,J) is greater than 0 and less than 6 on card type C8.
3. In the subsequent input description, the subscript J runs from 1 to NREAC.

RRATC(I,1,J) I=1,5)

Forward reaction rate coefficients. RRATC(I,1,J) are the reaction rate coefficients for the forward reaction of reaction mechanism J. The RRATC(I,1,J) coefficients correspond to the rate coefficients in Eq. (2.4c) with

RRATC(1,1,J) = A'_j pre-exponential factor

RRATC(2,1,J) = B'_j temperature exponent

RRATC(3,1,J) = C'_j activation energy

RRATC(4,1,J) = D'_j temperature exponent

RRATC(5,1,J) = T'_{o_j} reference temperature

All five of these coefficients are input for each of the NREAC reactions. The value of RTYPE(1,J) on card type C8 determines which of the five are significant in the calculation of the forward reaction rate. RRATC(1,1,J) is subject to per particle to per mole conversion if MOD(ICHUN/4,2) = 0 and RRATC(3,1,J) is subject to data conversion via the RRCF factor if MOD(ICHUN,2) = 0.

RRATC(I,1,J) I=1,5

Backward reaction rate coefficients. RRATC(I,2,J) are the reaction rate coefficients for the backward reaction of reaction mechanism J. The RRATC(I,2,J) coefficients correspond to the rate coefficients in Eq. (2.4d) with

RRATC(1,2,J) = A''_j pre-exponential factor
RRATC(2,2,J) = B''_j temperature exponent
RRATC(3,2,J) = C''_j activation energy
RRATC(4,2,J) = D''_j temperature exponent
RRATC(5,2,J) = T''_{o_j} reference temperature

All five of these coefficients are input for each of the NREAC reactions when RTYPE(2,J) is greater than 0 and less than 6. Otherwise, this second card type C9 is omitted and the backward reaction rate is either identically zero (RTYPE(2,J) = 0) or is calculated from the equilibrium constant (RTYPE(2,J) = 6) using Eqs. (2.4e) through (2.4g). If RTYPE(2,J) is greater than 0 and less than 6, the value of RTYPE(2,J) on card type C8 determines which of the RRATC(I,2,J) coefficients are significant in the calculation of the backward reaction rate. RRATC(1,2,J) is subject to per particle to per mole conversion if MOD(ICHUN/4,2) $\neq$ 0 and RRATC(3,1,J) is subject to data conversion via the RRCF factor if MOD(ICHUN,2) $\neq$ 0.

CARD TYPE C10 - Species Initialization Control

FORMAT (4I5)

Notes

1. Any number of cards type C10 may be used to initialize the species mass/mole fraction distribution. All nodes can be input on a single card or each node can be input on a separate card. The usual case is somewhere between these two extremes.

2. If ITYPE = 0 is input on card type C10, then (NSPEC-1)/8 + 1 cards of type C11 must immediately follow. If ITYPE ≠ 0, then no cards of type C11 are input.

3. A -1 card (columns 4-5) must be input as the last card in a type C10 sequence to terminate reading of species mass/mole fraction initial data.

4. Cards type C10 (and C11 if required) are not input for a restart case (ISTART ≠ 0) unless changes are being made. The -1 card must be presnt even on a restart case.

5. For a quasi-parabolic run (METHOD > 2), one sequence of cards type C10 (and c11 if required) must be input with the other chemistry data (cards C1 through C9) to initialize the first plane. If there are added zones in the problem, then additional sequences of cards type C10 (and C11 if required) may be needed to initialize species mass/mole fraction in the added zone plane. If this is the case, additional cards of type C10 (and C11 if required) should follow after integrator module cards type 16 and 16a.

6. If IMOLE = 0 on card type C1, then species mass fractions must be input on card type C11. If IMOLE = 1 on card type C1, then species mole fractions must be input on card type C11.

NJ

Node number of the first nodal point to be initialized by this card type C10. (NJ = -1 terminates the input of card C10).

INC

Node number increment to NJ to be used for inputting a sequence of nodes on one card. Set INC = 0 if only one node is to be set by this card. If INC ≠ 0, it will be added to NJ to determine the next node to be initialized.

NTOT

The total number of nodes to be set by this card type C10.

ITYPE

Indicates the type of species mass/mole fraction initialization is to be done.

ITYPE = 0 allows the user to input the initial species mass/mole fraction distribution on cards of type C11

= 1 sets the species mass/mole fractions for this card type C10 input to the same values as input on the last card type C11

= 2 allows the user to code and execute subroutine USERIP in order to initialize the species mass/mole fractions.

CARD TYPE C11 - Species Mass/Mole Fraction Initial Values

FORMAT (8E10.0)

1. Cards of type C11 are input following a card type C10 only if ITYPE = 0 is input on card type C10.
2. If ITYPE = 0 on card type C10, then (NSPEC-1)/8 + 1 cards of type C11 must follow.
3. Cards of type C11 are not input on a restart case unless changes are being made to the species mass/mole fraction distributions.

4. If IMOLE = 0 on card type C1, then species mass fractions must be input on card type C11. If IMOLE = 1 on card type C1, then species mole fractions must be input on card type C11.

5. In the subsequent input description, the subscript I runs from 1 to NSPEC, indicating the NSPEC species mass/mole fraction initial values associated with the nodes specified on card type C10.

CS(I)

Initial mass/mole fraction value for species I at those noses specified on preceeding card type C10. CS(I) must be in the following range:

$$0.0 \leq CS(I) \leq 1.0$$

In addition, the CS(I) must obey the following relationship:

$$\sum_{I=1}^{NSPEC} CS(I) = 1.0$$

2.6 SAMPLE CALCULATIONS

The results from two sample calculations using the GIM code chemically reacting flow model are presented in this section. These two test cases include:

1. Premixed hydrogen-air ignition in a one-dimensional duct-like geometry using a five-species, two-reaction global chemistry model developed for this problem by the method of Appendix A; and

2. The hydrogen-air parallel-injection case of Burrows and Kirkov (Ref. 2-5) using the five-species, two-reaction global chemistry model developed by Rogers and Chinitz (Ref. 2-6).

The first case consists of the ignition of premixed hydrogen and air in a one-dimensional 40 cm x 10 cm duct-like configuration. Figure 2-3 shows

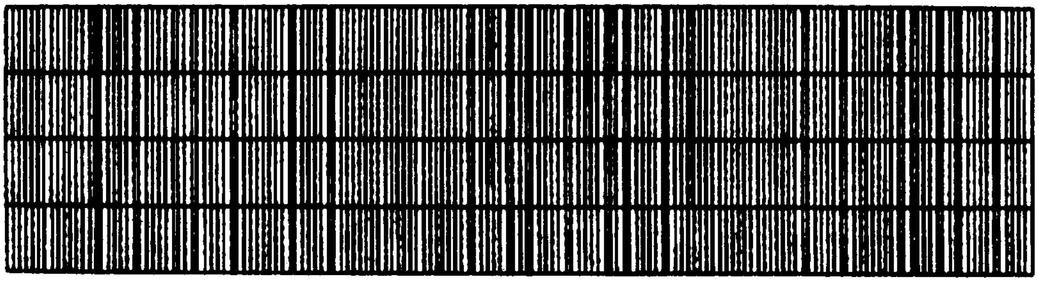

Fig. 2-3 - Premixed H_2-Air Case (Computational Grid)

the geometry and computational mesh used in this calculation. The global reaction mechanism was synthesized using the method of Appendix A for this geometry and flow conditions. The reaction mechanism consists of the five species N2, O2, H2, H2O, and OH and the following two reactions

$$H2 + O2 \overset{k_{F_1}}{\rightleftharpoons} OH + OH \qquad k_{F_1} = 4.171 \times 10^7 \ (T - 1000.0)^{0.98}$$

$$H2O + H2O \overset{k_{F_2}}{\rightleftarrows} OH + OH + H2 \qquad k_{F_1} = 1.054 \times 10^{-2} \ T^{5.87} \ \exp[- \frac{97748}{RT}]$$

where k_F and k_F are in units of cm^3/mole/sec. The inflow boundary conditions are given below:

$\rho = 3.204 \times 10^4 \ gm/cm^3$
$u = 1.464 \times 10^5 \ cm/sec$
$T = 1000 \ K$
$P = 1.013 \times 10^6 \ dyne/cm^2 = 1 \ atm$
$M = 2.25$

$$C_{N_2} = 0.76149 \quad C_{O2} = 23123 \quad C_{H2} = 0.00728 \quad C_{H2} = C_{OH} = 0$$

These same conditions were also used as the initialization for the remainder of the flow field. The integration was performed using the explicit chemistry solution option until the OH concentration reached a sufficient level for ignition to begin. At that point the code automatically switched to the implicit chemistry solution option and the calculation continued. The time step for this calculation was maintained at 0.95 times the flowfield CFL.

The results from this calculation presented in Figs. 2-4 through 2-8 show a sharp ignition front where the hydrogen-air combustion occurs. Figure 2-8 also presents a comparison with the results obtained from a spatial marching chemistry code (ALFA) for the same calculation. The discrepancy between the GIM code results and the results from the ALFA code solution are attributable to the inadvertent use of slightly different reaction rate coefficients in the two calculations.

The second sample calculation consists of the parallel injection case of Burrows and Kurkov (Ref. 2-5). In this case a cold sonic stream of hydrogen is injected parallel to a supersonic freestream of hot air. The resulting mixing and combustion are calculated and compared with the experimental data. Figure 2-9 shows the geometry of the test section used by Burrows and Kurkov to obtain the experimental results. A sparse version of the computational grid used in this calculation is shown in Fig. 2-10. This grid only displays every third node in the x-direction and every fifth node in the y-direction. The actual grid used in the calculation is thus much more dense, consisting of 109 cross planes with 56 nodes per plane. The nodes are clustered around the hydrogen jet near the inflow region in order to resolve the mixing that takes place. A Baldwin-Lomax turbulence model (see Section 5) was used to simulate the mixing process. Because the mixing and combustion takes place in a region close to the lower channel wall, the

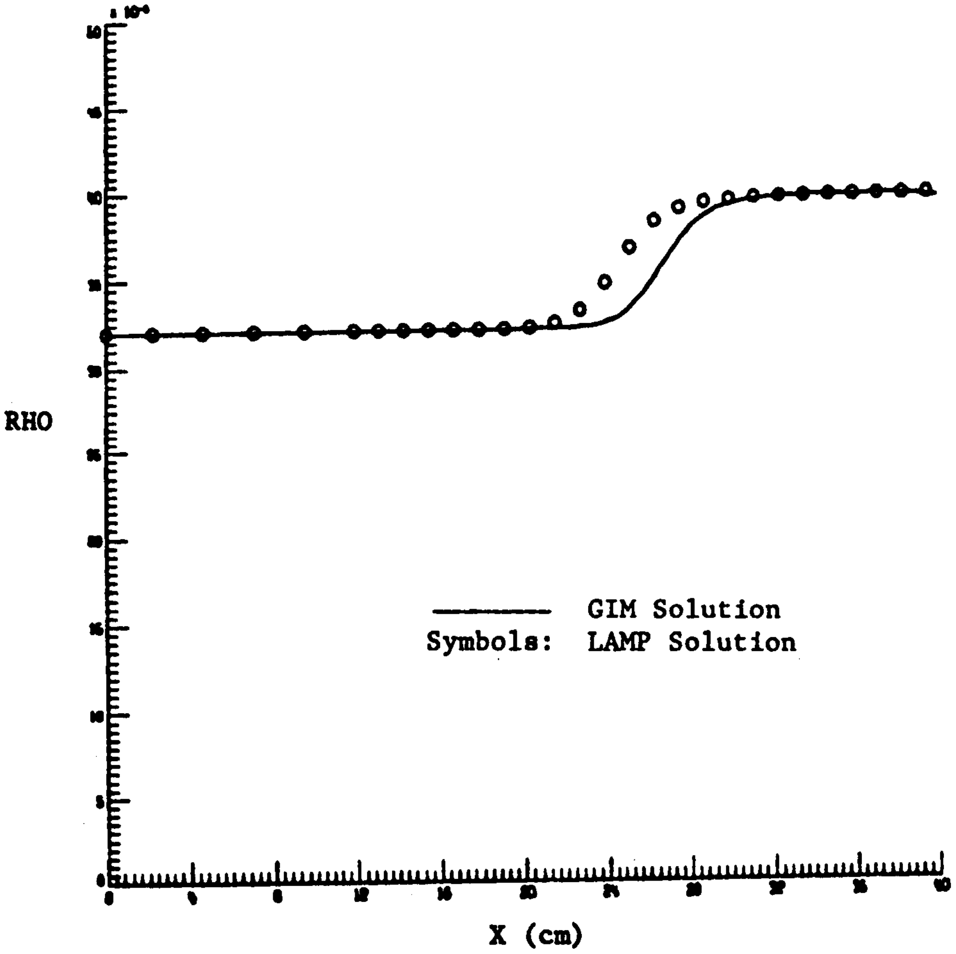

Fig. 2-4 - Premixed H_2-Air Case (Density vs X)

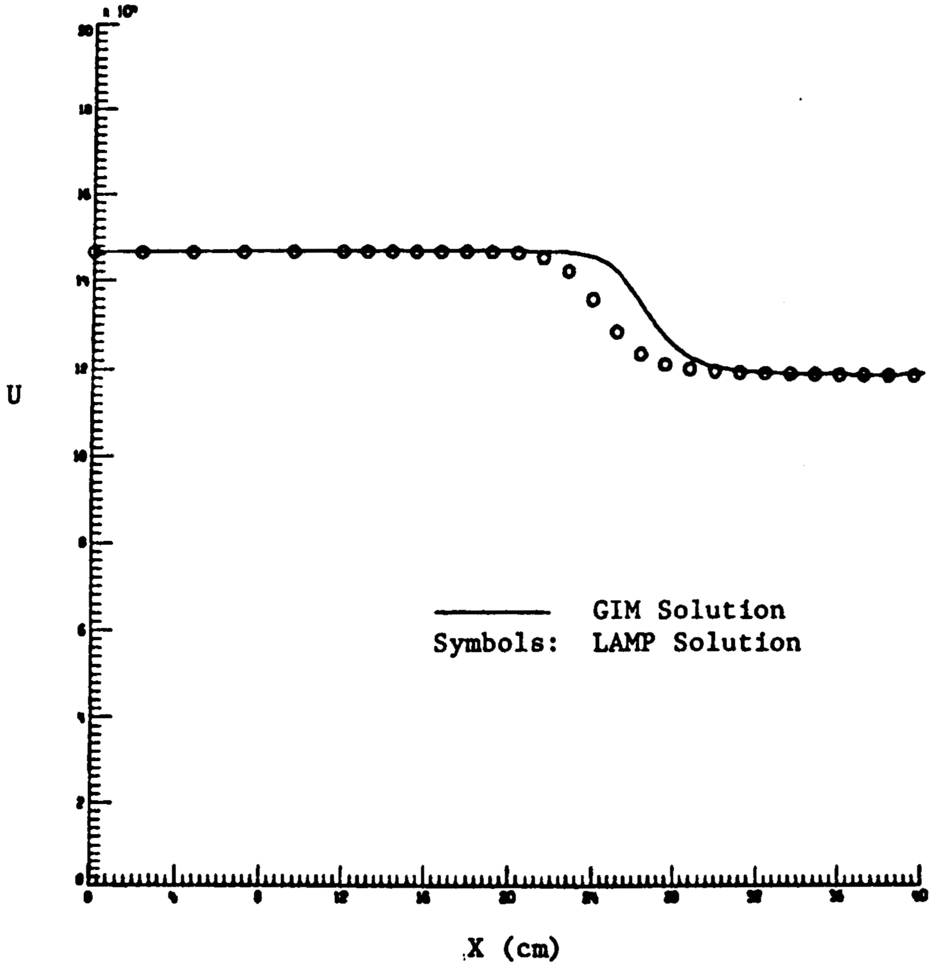

Fig. 2-5 - Premixed H_2-Air Case (Velocity vs X)

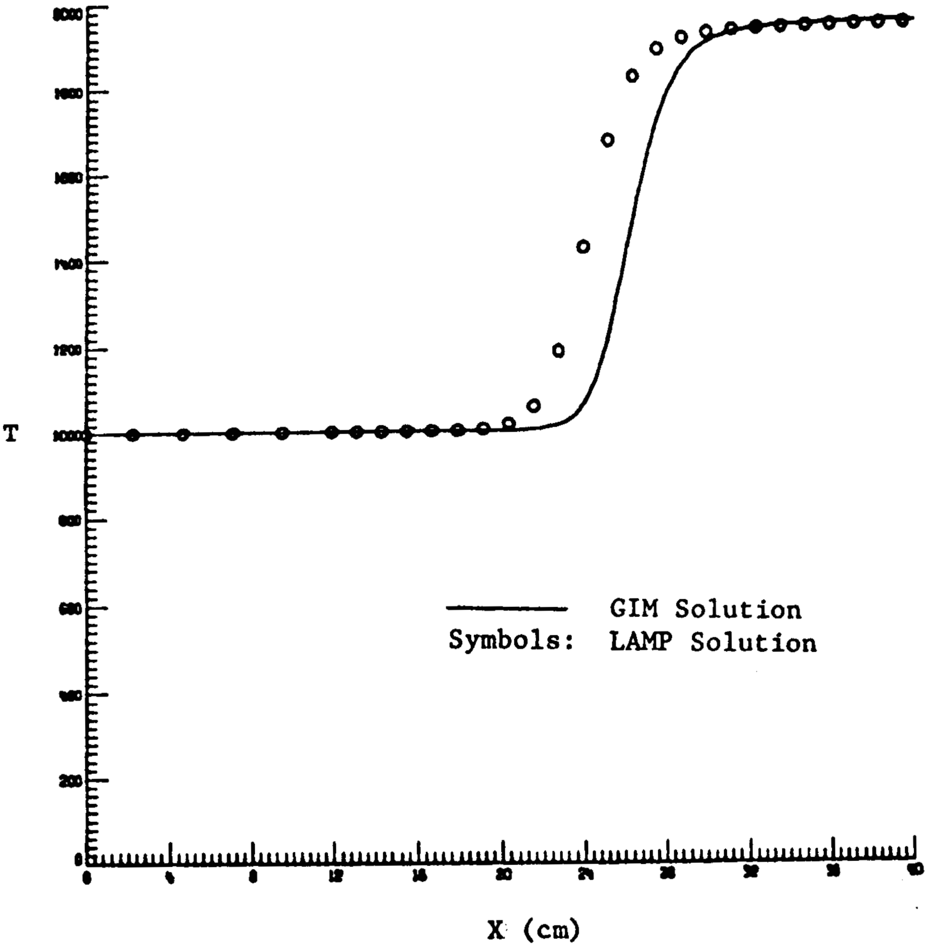

Fig. 2-6 - Premixed H_2-Air Case (Temperature vs X)

]

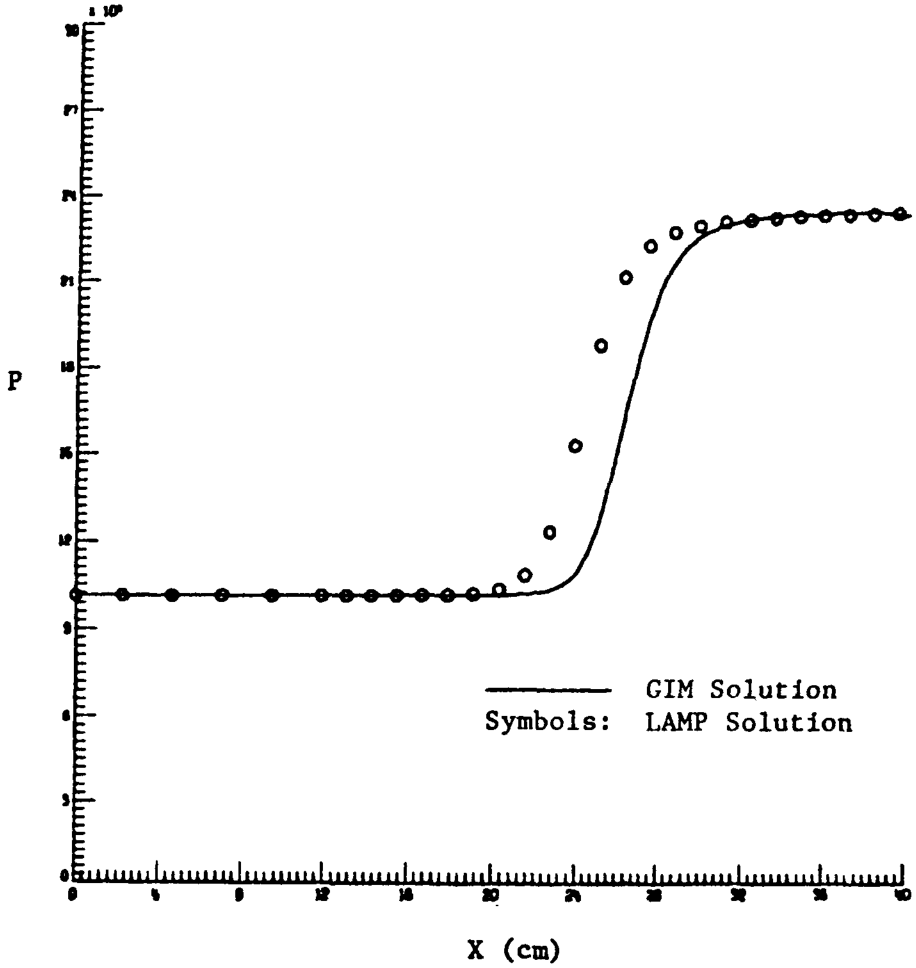

Fig. 2-7 - Premixed H_2-Air Case (Pressure vs X)

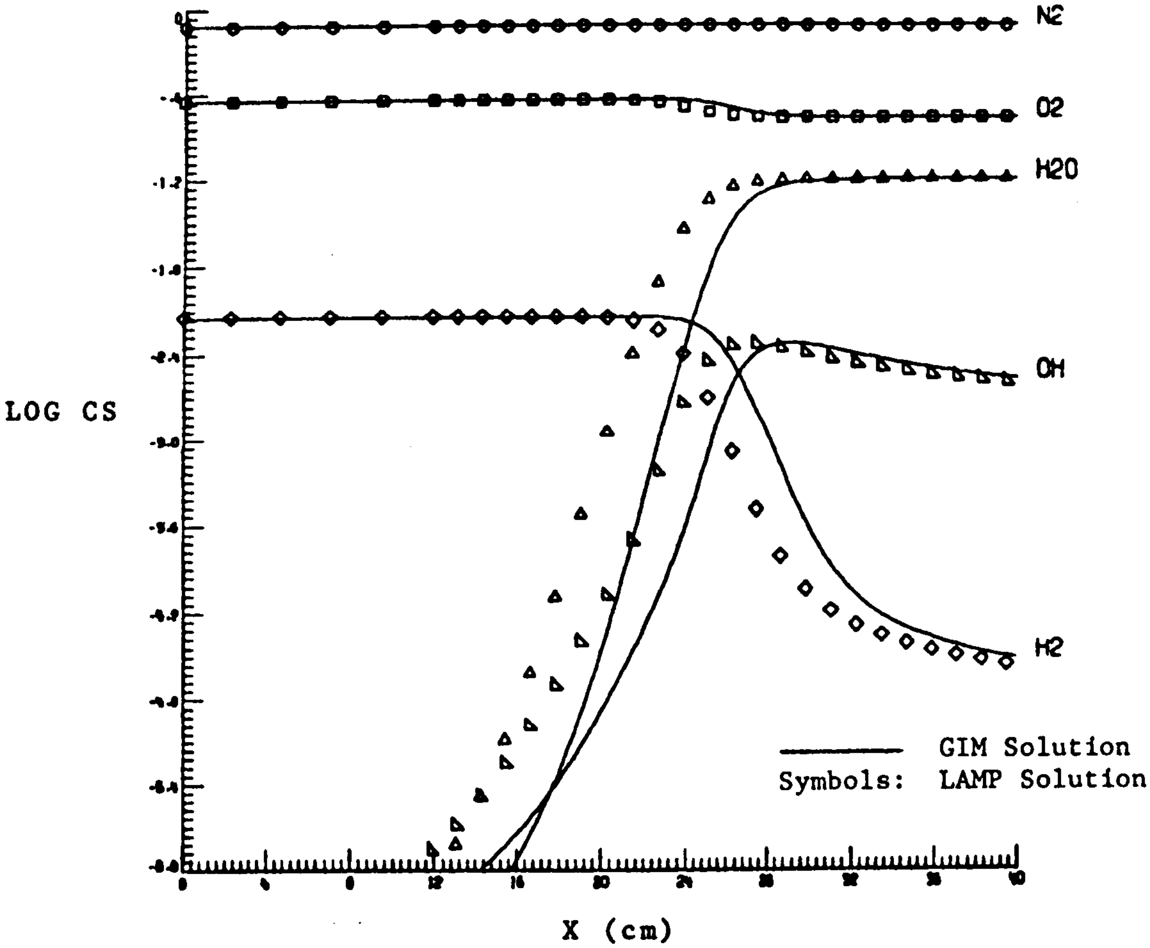

Fig. 2-8 - Premixed H_2-Air Case (Log Mass Fraction vs X)

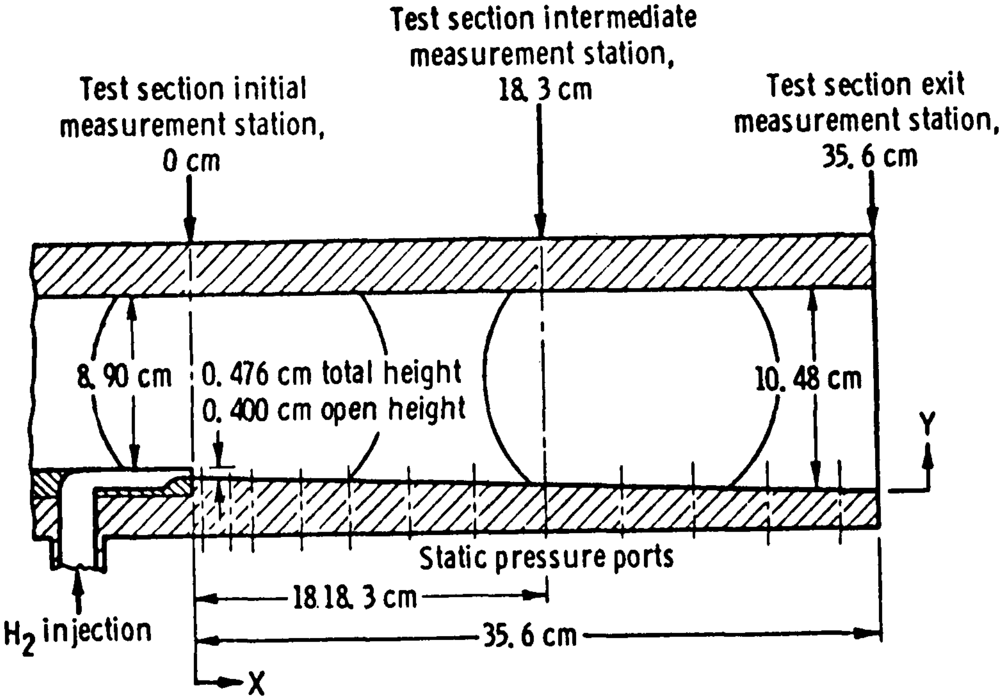

Fig. 2-9 - Parallel Injection Case (Test Section Geometry)

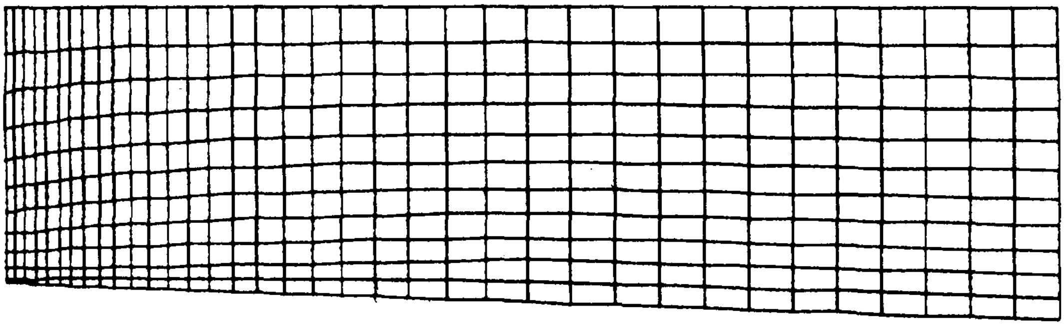

Fig. 2-10 - Parallel Injection Case (Computational Grid (Coarse)) upper boundary was treated as an inviscid free-slip/tangency boundary in order to avoid the necessity of resolving the boundary layer there. The lower channel wall was treated at a no-slip constant temperature boundary.

The flowfield conditions for this case are given below:

	Hydrogen Jet	Free Stream
Mach Number	1.00	2.44
Temperature (K)	254	1270
Velocity (cm/sec)	1.216×10^5	1.764×10^5
Pressure (dyne/cm^2)	1.1×10^6	1.1×10^6
Mass Fractions:		
C_{H2}	1.000	0
C_{O2}	0	0.258
C_{N2}	0	0.486
C_{H2O}	0	0.256
C_{OH}	0	0

The global hydrogen-air reaction mechanism developed by Rogers and Chinitz (Ref. 2-6) was used in this second sample calculation. This particular reaction mechanism consists of the five species N2, O2, H2, H2O, and OH and the following two reactions:

$$H2 + O2 \overset{k_{F_1}}{\rightleftarrows} 2\ OH \qquad k_{F_1} = 1.3823 \times 10^{48}\ T^{-10}\ \exp[\frac{-4865}{RT}]$$

$$2\ OH + H2 \overset{k_{F_2}}{\rightleftarrows} 2\ H2O \qquad k_{F_2} = 2.7166 \times 10^{64}\ T^{-13}\ \exp[\frac{-42500}{RT}]$$

where k_{F_1} is in units of cm^3/mole/sec and k_{F_2} is in units of cm^6/$mole^2$/sec. These reaction rate coefficients resulted in a set of very stiff species continuity equations and required the use of the implicit chemistry solution option (IXOPT = -1) and the stiff equation option (ISTIFF = 1) throughout the calculation. The integration was performed using the flowfield results from a standard GIM code binary gas integration run (with the same geometry and boundary conditions) as te initialization for this reacting case. The flow field was also initially "seeded" with small concentrations of OH in order to lessen the stiffness of the species continuity equations. The time step for this calculation was maintained at 0.75 times the flowfield CFL.

The results from this second calculation are presented in Figs. 2-11 through 2-16 for the test section exit station, x = 35.6 cm. The results show a very hot region of hydrogen-air combustion approximately 2.0 cm above the lower channel wall. Figure 2-16 shows a comparison of the GIM code solution with the Burrows and Kirkov experimental data. The comparison is relatively good although some of the calculated peaks in the H2O, N2, and O2 distributions are not quite as high as those indicated by the experimental data.

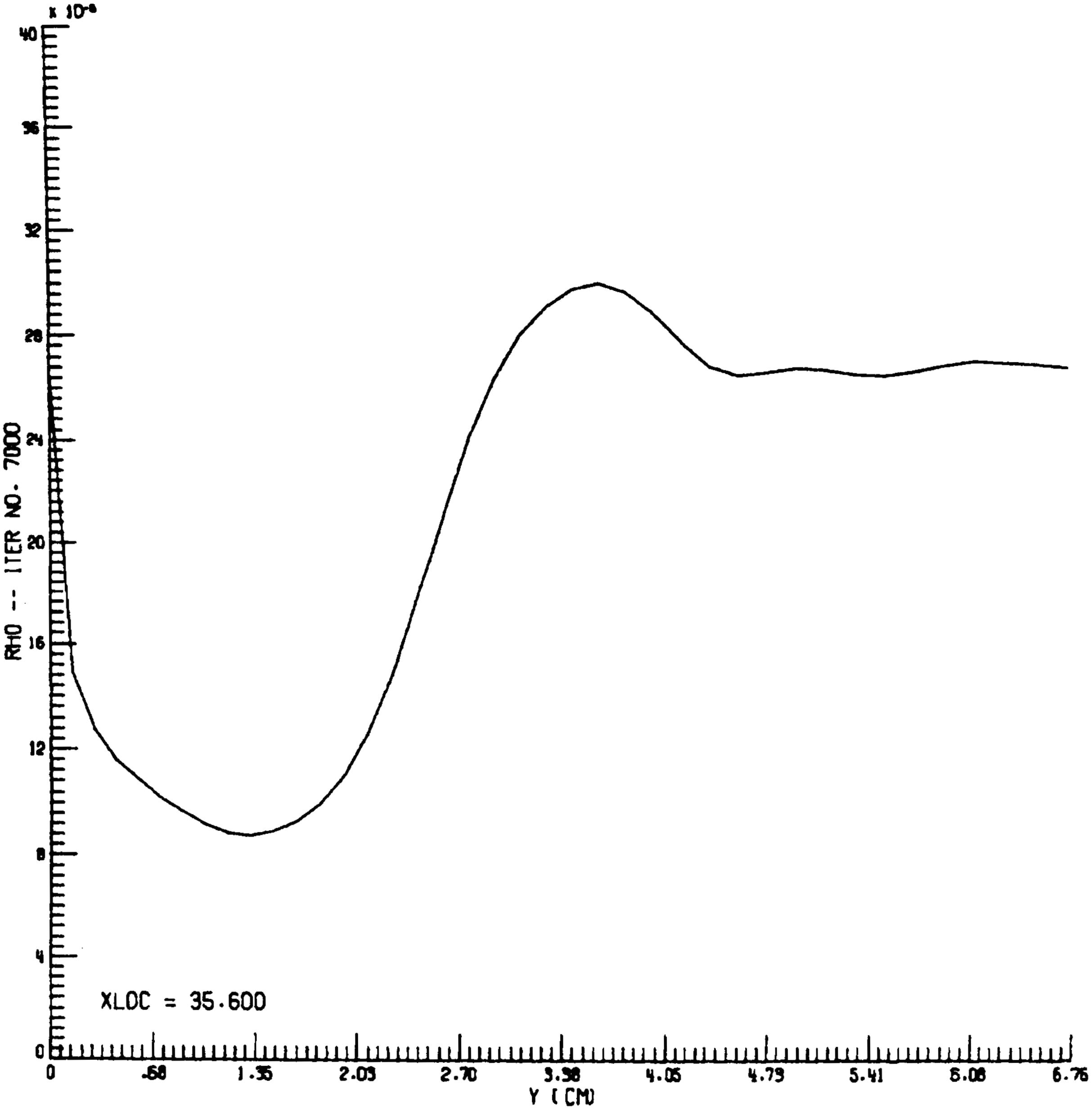

Fig. 2-11 - Parallel Injection Case (Density vs Y)

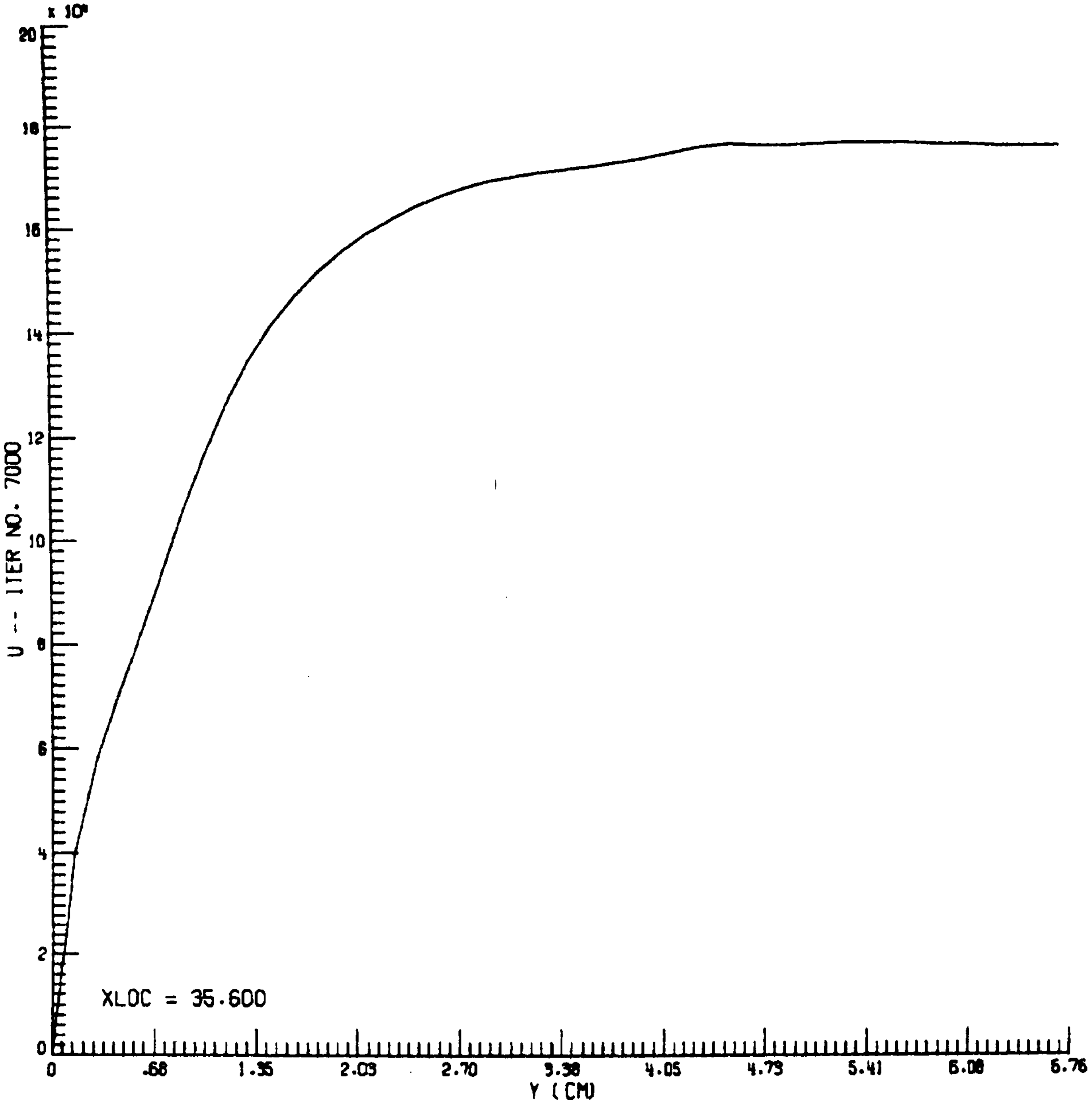

Fig. 2-12 - Parallel Injection Case (Velocity vs Y)

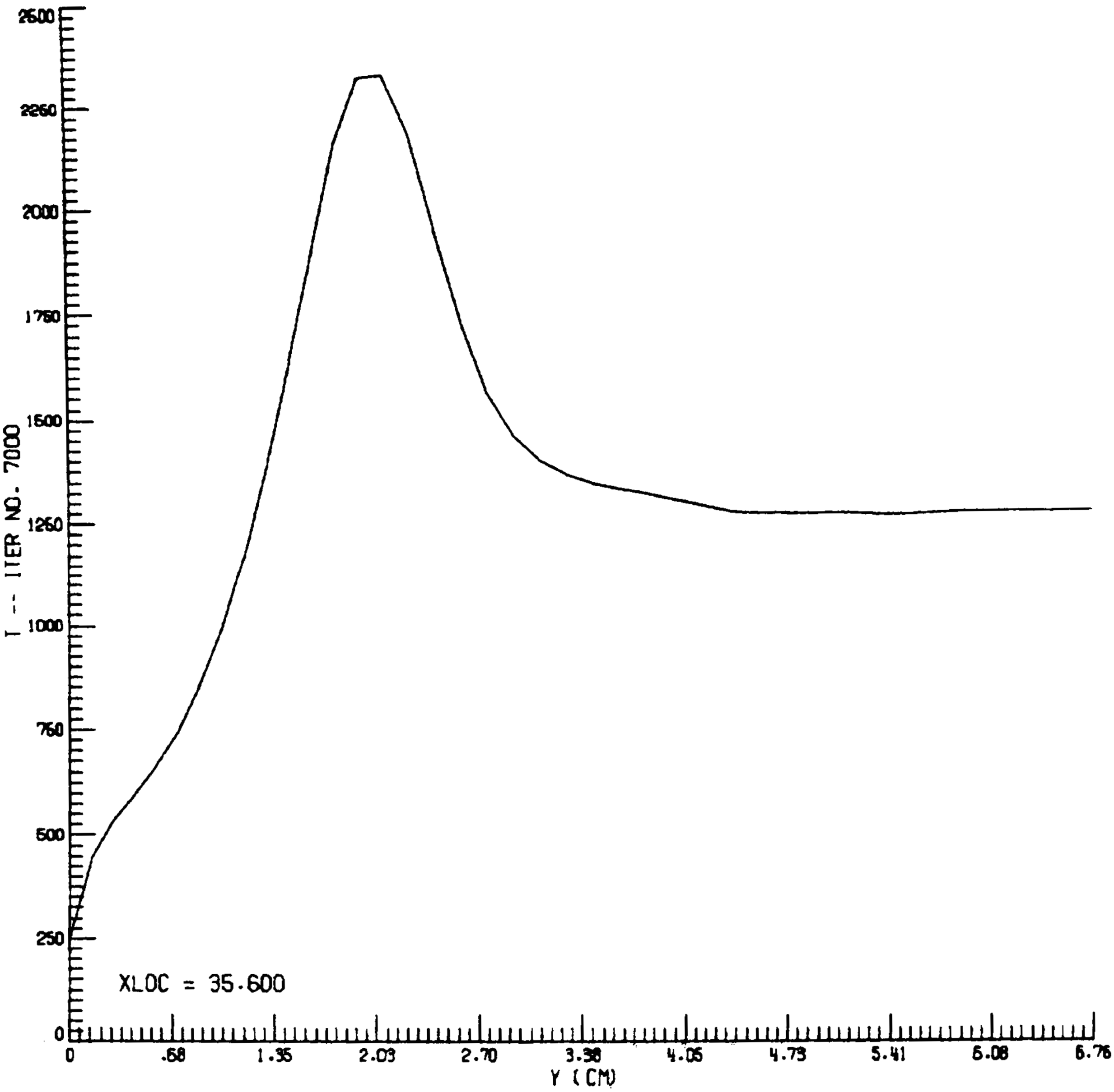

Fig. 2-13 - Parallel Injection Case (Temperature vs Y)

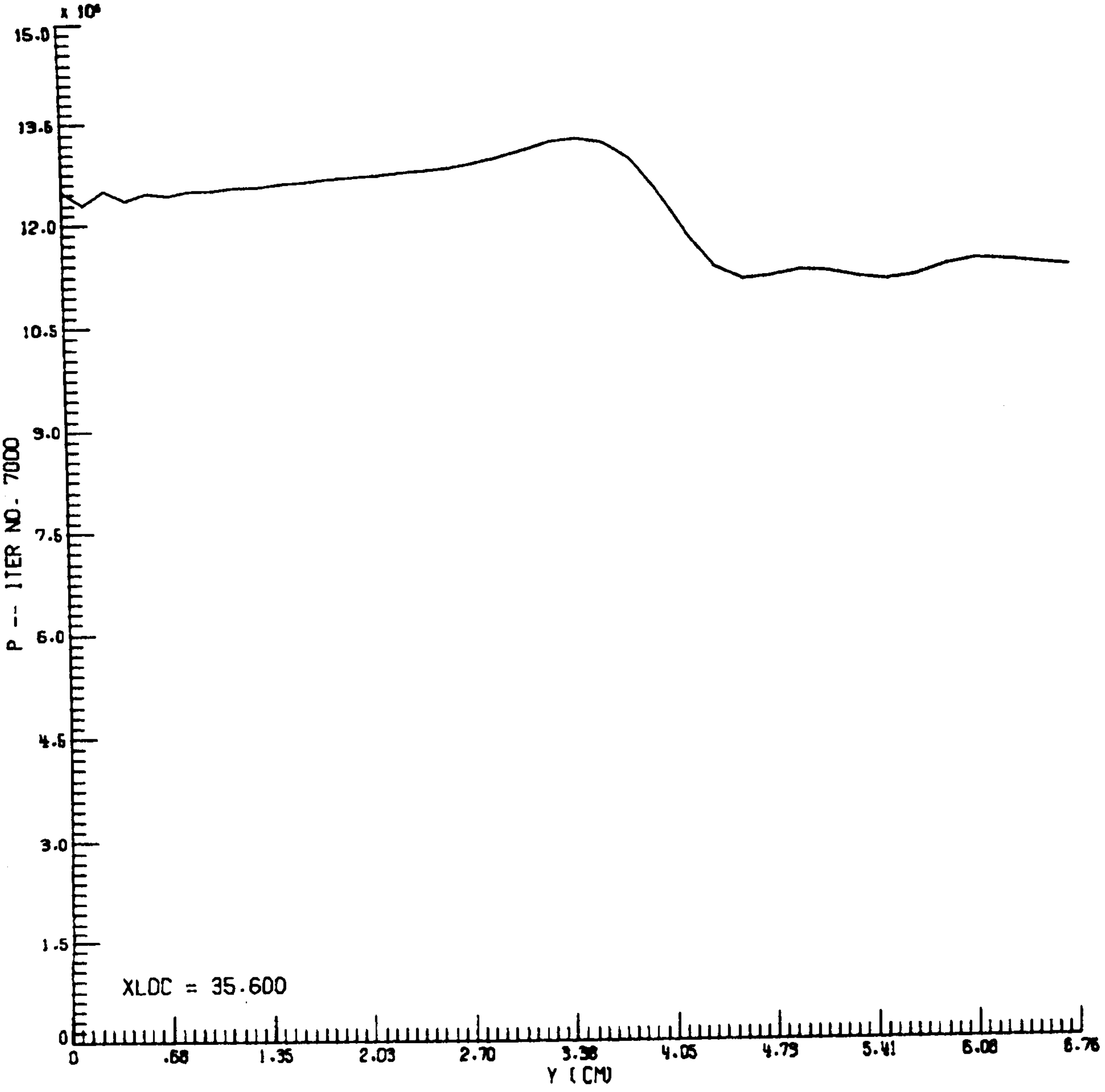

Fig. 2-14 - Parallel Injection Case (Pressure vs Y)

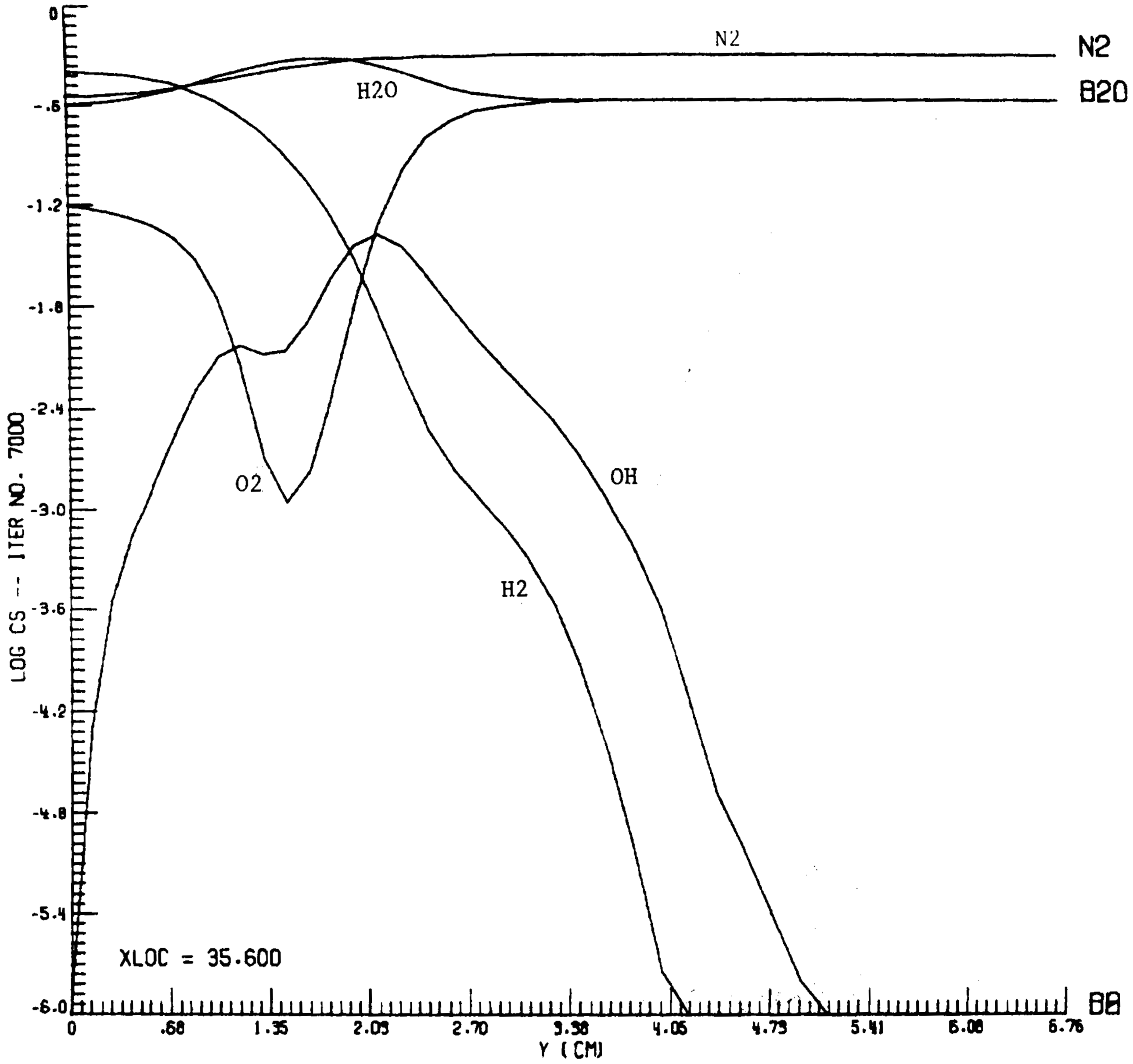

Fig. 2-15 - Parallel Injection Case (Log Mass Fraction vs Y)

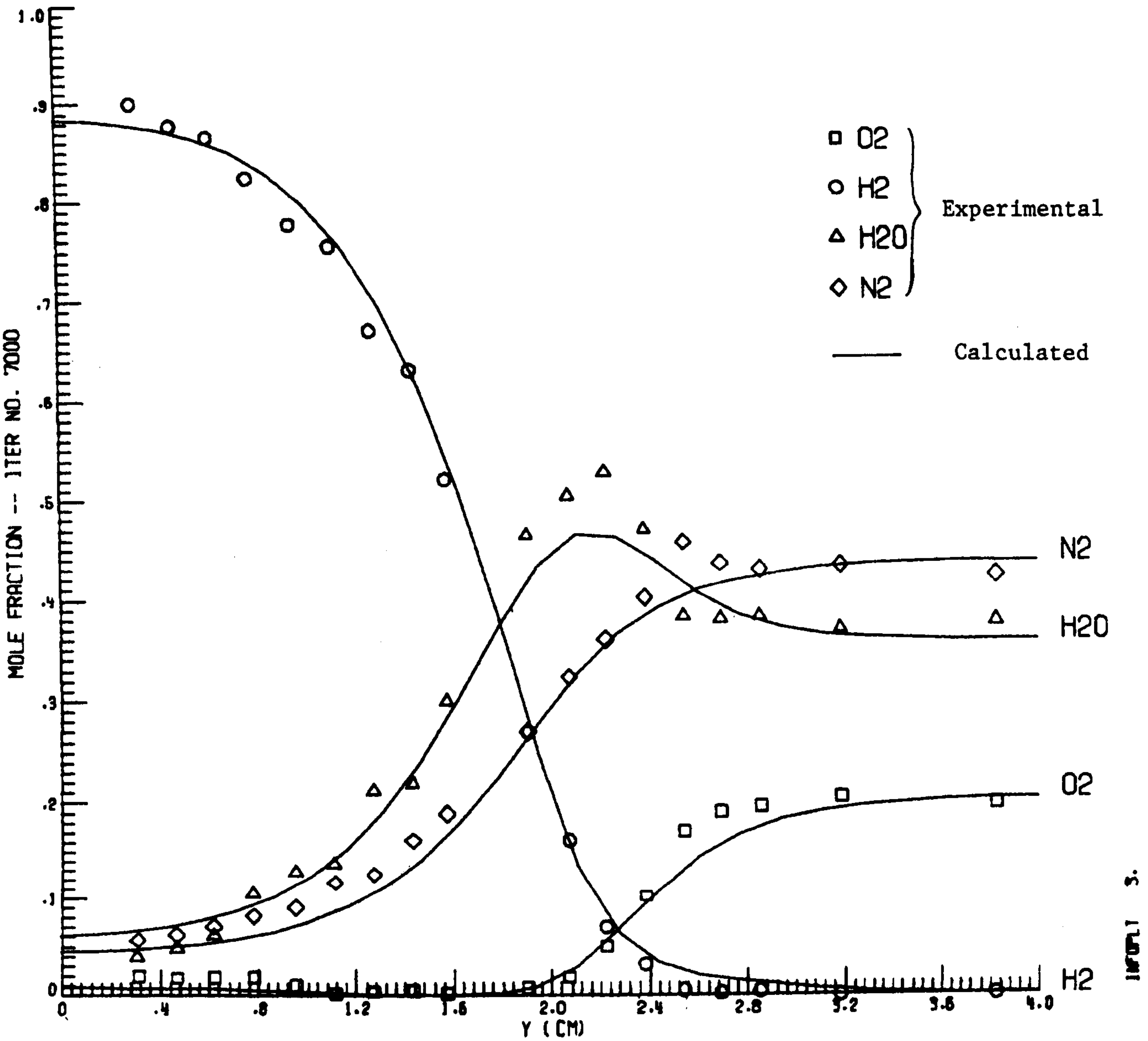

Fig. 2-16 - Parallel Injection Case (Experimental and Calculated Mass Fraction vs Y)

2.7 NOMENCLATURE

English Symbols

a	acoustic velocity
A	temperature/enthalpy quadratic equation coefficient; Eq. (2.21c)
A_j'	forward reaction rate coefficient, reaction j; Eq. (2.4c)
A_j''	backward reaction rate coefficient, reaction j; Eq. (2.4d)
B	temperature/enthalpy quadratic equation coefficient; Eq. (2.21d)
B_j'	forward reaction rate exponent, reaction j; Eq. (2.4c)
B_j''	backward reaction rate exponent, reaction j; Eq. (2.4d)
c_i	mass fraction of species i
C_{p_i}	specific heat at constant pressure of species i
C	temperature/enthalpy quadratic equation coefficient; Eq. (2.21e)
C_j'	forward reaction rate coefficient, reaction j; Eq. (2.4c)
C_j''	backward reaction rate coefficient, reaction j; Eq. (2.4d)
C:	denotes corrector step
CH:	denotes chemistry step
D_j'	forward reaction rate exponent, reaction j; Eq. (2.4c)
D_j''	backward reaction rate exponent, reaction j; Eq. (2.4d)
$\mathcal{D}_{d_1}, \mathcal{D}_{d_2}, \mathcal{D}_{d_3}$	artificial numerical diffusion coefficients for x_1, x_2, and x_3 components

$\mathcal{D}_r$	real diffusion coefficient
$\mathcal{D}_1,\mathcal{D}_2,\mathcal{D}_3$	sum of real and artificial diffusion coefficients
exp	exponential function
E_j	vector of flux terms; Eq. (2.6b)
$\mathcal{E}$	total internal energy per unit mass
ΔG_j	change in Gibbs' free energy for reaction j; Eq. (2.4g)
h_{f_i}	enthalpy of formation per unit mass of species i
$h_i(T)$	enthalpy per unit mass of species i at temperature T
$h_{i,j}$	enthalpy per unit mass ordinate of species i at temperature abscissa T_j
h_{o_i}	enthalpy per unit mass at reference temperature T_o of species i
$\overline{h}_f$	enthalpy of formation per mole of species i
$\overline{h}_o$	enthalpy per mole at reference temperature T_o of species i
$(\overline{h}_i - \overline{h}_{o_i})$	enthalpy per mole based on reference enthalpy $\overline{h}_{o_i}$ of species i
$h_{\text{flow field}}$	enthalpy per unit mass as computed from flowfield variables; Eq. (2.18a)
h_{specie}	enthalpy per unit mass as computed from species variables; Eq. (2.18b)
H	vector of production terms, Eq. (2.6b)
$(\partial H/\partial U)$	Jacobian matrix of vector H
I	identity matrix
J	number of discrete equally spaced temperature abscissa
k	coefficient of thermal conductivity
k_{b_j}	backward reaction rate constant for reaction j; Eq. (2.4d)

k_{f_j}	forward reaction rate constant for reaction j; Eq. (2.4c)
K_{c_j}	concentration equilibrium constant for reaction j; Eq. (2.4e)
K_{p_j}	pressure equilibrium constant for reaction j; Eq. (2.4f)
$\bar{m}_i$	molecular weight of species i
M	number of reactions
$\mathbf{M}$	implicit coefficient matrix; Eq. (2.23b)
N	number of species
p	pressure
P:	denotes predictor step
q	velocity magnitude
q_1,q_2,q_3	heat flux per unit area for x_1, x_2, x_3 coordinate directions
R	gas constant for mixture $= \sum_{i=1}^{N} c_i \frac{\Re}{\bar{m}_i}$
$\Re$	universal gas constant
RHS	implicit right-hand side vector; Eq. (2.23b)
$\bar{s}_i$	entropy per mole of species i
t	time
Δt	time step
T	temperature
T_j	temperature abscissa, j^{th} value
T_o	reference temperature
T'_{o_j}	forward reaction rate reference temperature, reaction j; Eq. (2.4c)
T''_{o_j}	backward reaction rate reference temperature, reaction j, Eq. (2.4d)
ΔT	temperature increment

u_1, u_2, u_3	velocity components
U	vector of conserved variables; Eq. (2.6b)
$\mathcal{U}$	implicit time derivative vector; Eq. (2.23b)
δU^{n+1}	finite difference time derivative of conserved variables at time level n+1
ΔU^{n+1}	change in conserved variables at time level n+1
$\dot{w}_i$	chemistry production term for species i; Eq. (2.4b)
x_1, x_2, x_3	coordinate directions
X_j	reaction components defied by Eq. (2.25b)

Greek Symbols

δ_{ij}	Kronecker delta = 1 for $i = j$, = 0 for $i = j$
ε	artificial diffusion constant
λ	coefficient of bulk viscosity
ρ	mass density
μ	coefficient of viscosity
ν'_{ij}	stoichiometric coefficient for species i as a reactant in reaction j
ν''_{ij}	stoichiometric coefficient for species i as a product in reaction j
$\Delta \nu_{ij}$	$\nu''_{ij} - \nu'_{ij}$
τ_{ij}	stress tensor; Eq. (2.2b)

Operators

$B[\ \ ]$	boundary condition operator
$\partial^B/\partial x_j$	backward spatial difference operator for coordinate direction j
$\partial^F/\partial x_j$	forward spatial difference operator for coordinate direction j

Superscripts

(ℓ)	ℓ^{th} implicit chemistry iteration for time level n+1 time
n	level n
$\overline{n+1}$	first provisional time level (predictor step)
$\overline{\overline{n+1}}$	second provisional time level (corrector step)
n+1	time level n+1
overbar	molar basis

2.8 REFERENCES FOR SECTION 2

2-1. MacCormack, R.W., "The Effect of Viscosity in Hypervelocity Impact Cratering," AIAA Paper No. 69-354, May 1969.

2-2. McRae, G.J., W.R. Goodin, and J.H. Seinfeld, "Numerical Solution of the Atmospheric Diffusion Equation for Chemically Reacting Flows," J. Comp. Physics, Vol. 45, No. 1, January 1982, pp. 1-42.

2-3. Forester, C.K., "Higher Order Monotonic Convective Differencing Schemes," J. Comp. Physics, Vol. 23, No. 1, January 1977, pp. 1-22.

2-4. Stalnaker, J.F., M.A. Robinson, E.G. Rawlinson, P.G. Anderson, A.W. Mayne, and L.W. Spradley, "Development and Application of the GIM Code for the CYBER 203 Computer," NASA CR-3652, December 1982.

2-5. Burrows, M.C., and A.P. Kurkov, "Analytical and Experimental Study of Supersonic Combustion of Hydrogen in a Vitiated Airstream," NASA TM X-2828, September 1973.

2-6. Rogers, R.C., and W. Chinitz, "On the Use of a Global Hydrogen-Air Combustion Model in the Calculation of Turbulent Reacting Flows," AIAA Paper No. 82-0112, January 1982.

3. THE GIM HYPERBOLIC STEADY STATE EULER SOLVER

3.1 METHODOLOGY

The success of the General Interpolants methodology in developing computer codes for three-dimensional flowfield calculations in arbitrary geometric domains has lead to an elliptic unsteady Navier-Stokes solver for complete viscous, compressible flow analysis and an iterative quasi-unsteady parabolic Navier-Stokes solver for viscous flows with a predominant flow direction along which second order effects can be neglected. Although the latter method has been used extensively (Refs. 3-1 through 3-4) to solve the completely inviscid supersonic Euler equations, the iterative procedure is unnecessary for such flows since the equations are hyperbolic in the flow direction and it adds considerable computational cost. The impetus for using the quasi-parabolic code in the inviscid mode was to take advantage of the geometric versatility of the GIM approach. This section reports on a non-iterative hyperbolic steady-state Euler equation solver developed through the General Interpolants Method which has the following among its many features:

- The geometric versatility of all GIM derivatives
- The second order accuracy, efficiency and highly vectorizable characteristics of a MacCormack predictor-corrector solution algorithm
- The advantages of the new technique for progressive assembly of the GIM difference analogs (see Appendix D)
- Continuous monitoring of the marching stepsize with the capability to interpolate intermediate cross planes to prevent violation of stability limits

- Entropy consistent inviscid boundary conditions
- Shock-capturing techniques
- Integration of the equations in the Cartesian physical domain.

This solver has proven to be quite accurate and efficient in axisymmetric, two- and three-dimensional test cases. The next subsection details the finite difference model. The following two subsections describe the stepsize control mechanism and the boundary conditions, respectively.

3.1.1 The Finite Difference Model

The Euler equations for three-dimensional compressible inviscid gas dynamics are

$$\frac{\partial U}{\partial t} + \frac{\partial E}{\partial x} + \frac{\partial F}{\partial y} + \frac{\partial G}{\partial z} = 0 \tag{3.1}$$

where

$$U = \begin{bmatrix} \rho \\ \rho u \\ \rho v \\ \rho w \\ \rho\mathcal{E} \end{bmatrix} \qquad E = \begin{bmatrix} \rho u \\ \rho u^2 + P \\ \rho uv \\ \rho uw \\ \rho Hu \end{bmatrix}$$

$$F = \begin{bmatrix} \rho v \\ \rho vu \\ \rho v^2 + P \\ \rho vw \\ \rho Hv \end{bmatrix} \qquad G = \begin{bmatrix} \rho w \\ \rho wu \\ \rho wv \\ \rho w^2 + P \\ \rho Hw \end{bmatrix}$$

and where

ρ = mass density
H = total enthalpy
P = pressure
$\mathcal{E}$ = total energy
u = x-component of velocity
w = z-component of velocity
v = y-component of velocity
x,y,z,t = space and time coordinates

and

$$P = \left(\frac{\gamma - 1}{\gamma}\right) \rho \left[H - \frac{u^2 + v^2 + w^2}{2} \right] \quad \text{(ideal gas law)}$$

Application of the General Interpolants methodology (Ref. 3-5) using the weight functions derived for the progressive assembly of the derivative-taking analogs (Appendix D) results in the following finite difference analog of the Euler equations at node N.

$$\left[\frac{\Delta(x,y,z)}{\Delta(\eta_1,\eta_2,\eta_3)}\right]_N \dot{U}_N + \left[\frac{\Delta(E,y,z)}{\Delta(\eta_1,\eta_2,\eta_3)}\right]_N + \left[\frac{\Delta(x,F,z)}{\Delta(\eta_1,\eta_2,\eta_3)}\right]_N + \left[\frac{\Delta(x,y,G)}{\Delta(\eta_1,\eta_2,\eta_3)}\right]_N = 0 \qquad (3.2)$$

where the terms in brackets are the assembled finite difference Jacobians:

$$\frac{\Delta(f,g,h)}{\Delta(\eta_1,\eta_2,\eta_3)} = \sum_{e=1}^{8} \alpha_e \left[\frac{\delta(f,g,h)}{\delta(\eta_1,\eta_2,\eta_3)}\right]^e$$

and

$$\left[\frac{\delta(f,g,h)}{\delta(\eta_1,\eta_2,\eta_3)}\right]^e$$

is the element finite difference Jacobian for element e as described in Appendix D. The α_e are the arbitrary weighting factors which determine the direction of the differencing and

$$\sum_{e=1}^{8} \alpha_e = 1 \tag{3.3}$$

One choice of weighting factors which satisfy Eq. (3.3) is a set of tri-linear interpolants:

$$\begin{array}{llll} \alpha_1 = (1 - \theta_1)\,(1 - \theta_2)\,(1 - \theta_3) & & \alpha_5 = (1 - \theta_1\,(1 - \theta_2)\,\theta_3 \\ \alpha_2 = \theta_1\,(1 - \theta_2\,(1 - \theta_3) & & \alpha_6 = \theta_1\,(1 - \theta_2)\,\theta_3 \\ \alpha_3 = \theta_1\,\theta_2\,(1 - \theta_3) & & \alpha_7 = \theta_1\,\theta_2\,\theta_3 \\ \alpha_4 = (1 - \theta_1\,\theta_2\,(1 - \theta_3) & & \alpha_8 = (1 - \theta_1)\,\theta_2\,\theta_3 \end{array} \tag{3.4}$$

where the θ_i govern the differencing direction in η_i as follows:

$\theta_i = 0$ - forward η_i differences
$\theta_i = 1/2$ - centered η_i differences
$\theta_i = 1$ - backward η_i differences

Thus, the coefficient of $\dot{U}_N$ in Eq. (3.2) can be viewed as an interpolated control volume for the discrete difference model.

For the steady-state Euler equations we set $\dot{U}_N = 0$. The finite difference model is a spatial marching version of the MacCormack explicit predictor-corrector scheme (Ref. 3-6). To implement this scheme we choose $\theta_1 = 0$ for both steps and θ_2 and θ_3 are chosen to yield the classic alternating differences on the predictor and corrector steps. The choice of cross-flow differencing is completely arbitrary and user input. The resulting algorithm may be written

Predictor:

$$\bar{E} = E^n + \sum_{e=1}^{8} \alpha_e \left\{ \delta_2^e E^n \left[\frac{\delta(y^n,z^n)}{\delta(\eta_3,\eta_1)}\right]^e + \delta_3^e E^n \left[\frac{\delta(y^n,z^n)}{\delta(\eta_1,\eta_2)}\right]^e \right.$$

$$\left. + \left[\frac{\delta(x^n,F^n,z^n)}{\delta(\eta_1,\eta_2,\eta_3)}\right]^e + \left[\frac{\delta(x^n,y^n,G^n)}{\delta(\eta_1,\eta_2,\eta_3)}\right]^e \right\} \Big/ \sum_{e=1}^{8} \alpha_e \left[\frac{\delta(z^n,y^n)}{\delta(\eta_2,\eta_3)}\right]^e \qquad (3.5a)$$

Corrector:

$$E^{n+1} = \frac{1}{2} \left\{ E^n + \bar{E} + \right.$$

$$\sum_{e=1}^{8} \bar{\alpha}_e \left\{ \delta_2^e \bar{E} \left[\frac{\delta(y^n,z^n)}{\delta(\eta_3,\eta_1)}\right]^e + \delta_3^e \bar{E} \left[\frac{\delta(y^n,z^n)}{\delta(\eta_1,\eta_2)}\right]^e \right.$$

$$\left. + \left[\frac{\delta(x^n,F,z^n)}{\delta(\eta_1,\eta_2,\eta_3)}\right]^e + \left[\frac{\delta(x^n,y^n,\bar{G})}{\delta(\eta_1,\eta_2,\eta_3)}\right]^e \right\} \Big/ \sum_{e=1}^{8} \alpha_e \left[\frac{\delta(z^n,y^n)}{\delta(\eta_2,\eta_3)}\right]^e \qquad (3.5b)$$

where, again, the terms in brackets are the two and three-dimensional Jacobian determinants and δ_i^e is the appropriate two-point difference operator in the η_i direction for element e. α_e and $\bar{\alpha}_e$ are the predictor and corrector weighting factors, respectively. The overbar (—) represents predicted values. The marching proceeds down η_1 grid lines from station n to station n+1.

Notice that the metric information is evaluated at station n on both steps. This is done, first, because the advanced geometry lies outside the domain of dependence of both the partial differential equations and the difference equations, and, secondly, from the realization that the actual advancement of the solution occurs on the corrector step. The primitive variables are decoded from the flux vector E assuming supersonic flow in the x direction.

The geometric versatility of the other GIM derivatives was maintained by retaining the terms in $\delta_1^e F$ and $\delta_1^e G$. This does not require the cross-flow mesh to be orthogonal to the x axis. It does, however, require an iterative procedure for non-orthogonal meshes. This iteration converges quickly (<5 iterations) and is a small penalty to pay for the increased geometric power.

This algorithm readily lends itself to vectorization on the CYBER 200 series of supercomputer. This efficiency along with the proven accuracy of the technique far outweigh the limitations placed on the marching stepsize by its explicit nature and preclude the use of much less computationally efficient implicit methods.

3.1.2 Hyperbolic Stability Analysis

As is the case in all explicit hyperbolic marching algorithms, the magnitude of the spatial or marching step size used in the GIM code steady state marching algorithm is constrained by the hyperbolic nature of the flow field. The maximum allowable spatial step size is given by the CFL criteria, i.e., the domain of dependence of the partial differential equations, which comprises the area enclosed by the intersection of the Mach conoid through the solution point and the previous initial value surface, must be contained within the domain of dependence of the finite difference equations (Ref. 3-7). This concept is shown geometrically in Fig. 3-1.

The equation of the Mach conoid is given by (Ref. 3-7):

$$[u^2 - (V^2 - a^2)]\,(dx)^2 + [v^2 - (V^2 - a^2)]\,(dy)^2 + [w^2 - (V^2 - a^2)]\,(dz)^2 + 2\,uv\,dx\,dy + 2\,uw\,dx\,dz + 2\,vw\,dy\,dz = 0 \qquad (3.6)$$

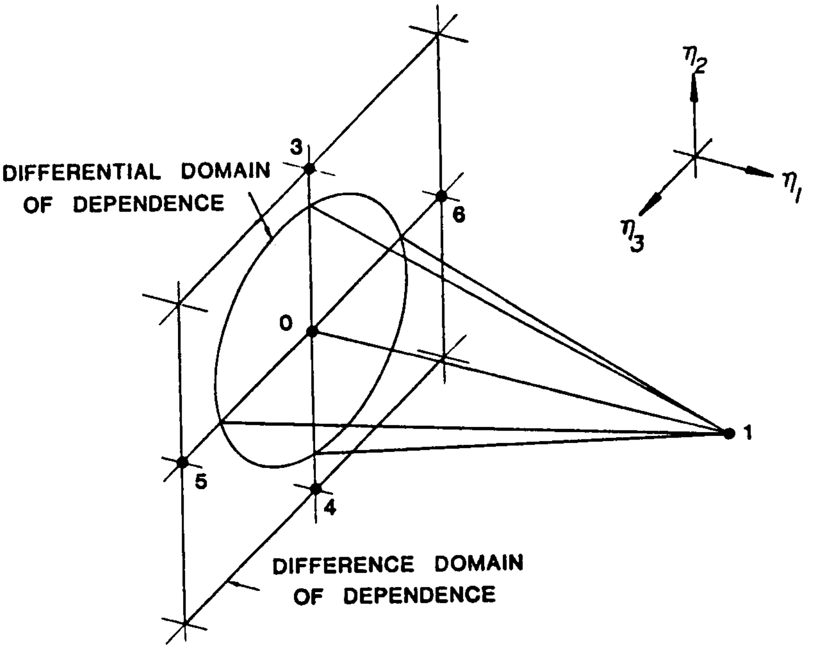

Fig. 3-1a - Hyperbolic Stability Analysis (Stable Spatial Step Size)

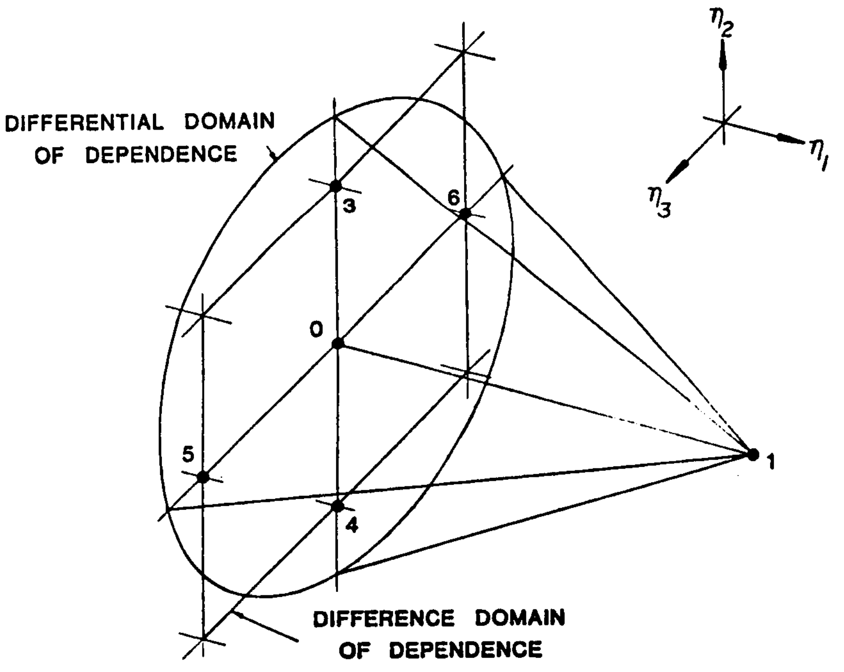

Fig. 3-1b - Hyperbolic Stability Analysis (Unstable Spatial Step Size) where V is the velocity magnitude and a is the speed of sound. Let the intersection of the Mach conoid from a node on the solution surface (point 1 in Fig. 3-1) with the grid line passing through the previous solution node and any connected node (point 0 and points 3,4,5, and 6 in Fig. 3-1) be designated by x and let its position be defined in terms of a parameter θ, then

$$\bar{x} = \begin{bmatrix} x \\ y \\ z \end{bmatrix} = (1 - \theta) \begin{bmatrix} x_o \\ y_o \\ z_o \end{bmatrix} + \theta \begin{bmatrix} x_c \\ y_c \\ z_c \end{bmatrix} \tag{3.7}$$

where subscript c denotes any connected node. On the Mach conoid, let the differentials be approximated by differences, i.e.,

$$\begin{bmatrix} dx \\ dy \\ dz \end{bmatrix} \cong \begin{bmatrix} \Delta x \\ \Delta y \\ \Delta z \end{bmatrix} = \begin{bmatrix} x_1 \\ y_1 \\ z_1 \end{bmatrix} - \begin{bmatrix} x \\ y \\ z \end{bmatrix} \tag{3.8}$$

Then Eqs. (3.7) and (3.8) together yield

$$\begin{aligned} \begin{bmatrix} \Delta x \\ \Delta y \\ \Delta z \end{bmatrix} &= \begin{bmatrix} x_1 \\ y_1 \\ z_1 \end{bmatrix} - \begin{bmatrix} (1 - \theta)x_o + \theta x_c \\ (1 - \theta)y_o + \theta y_c \\ (1 - \theta)y_o + \theta z_c \end{bmatrix} \\ &= \begin{bmatrix} x_1 - x_o \\ y_1 - y_o \\ z_1 - z_o \end{bmatrix} - \theta \begin{bmatrix} x_c - x_o \\ y_c - y_o \\ z_c - z_o \end{bmatrix} \\ &= \begin{bmatrix} \Delta x_1 \\ \Delta y_1 \\ \Delta z_1 \end{bmatrix} - \theta \begin{bmatrix} \Delta x_c \\ \Delta y_c \\ \Delta z_c \end{bmatrix} \end{aligned} \tag{3.9}$$

Equation (3.6) can then be approximated by

$$A\Delta x^2 + B\Delta x\ \Delta y + C\Delta y^2 + D\Delta y\ \Delta z + E\Delta z^2 + F\Delta x\ \Delta z = 0 \tag{3.10}$$

where

$A = u^2 - (V^2 - a^2)$ $B = 2uv$ $C = v^2 - (V^2 - a^2)$

$D = 2vw$ $E = w^2 - (V^2 - a^2)$ $F = 2uw$

If the definitions of Δx, Δy, and Δz given by Eq. (3.9) are substituted into Eq. (3.10) and like powers of θ are collected, the results is given by

$$\mathcal{A}\,\theta^2 - \mathcal{B}\theta + \mathcal{C} = 0$$

where

$$\begin{aligned}
\mathcal{A} &= A\ \Delta x_c^{\ 2} + B\ \Delta x_c\ \Delta y_c + C\ \Delta y_c^{\ 2} + D\Delta y_c\Delta z_c + E\Delta z_c^{\ 2} + F\Delta x_c\ \Delta z_c \\
\mathcal{B} &= 2A\Delta x_1\Delta x_c + B(\Delta x_1\ \Delta y_c + \Delta x_c\ \Delta y_1) + 2C\ \Delta y_1\ \Delta y_c \\
&\quad + D(\Delta y_1\Delta z_c + \Delta y_c\ \Delta z_1) + 2E\ \Delta z_1\Delta z_c + F(\Delta x_1\Delta z_c + \Delta x_c\ \Delta z_1) \\
\mathcal{C} &= A\Delta x_1^2 + B\ \Delta x_1\Delta y_1 + C\Delta y_1^{\ 2} + D\Delta y_1\Delta z_1 + E\Delta z_1^{\ 2} + F\Delta x_1\ \Delta z_1
\end{aligned} \tag{3.11}$$

Equation (3.11) is a simple quadratic equation in θ with the solution given by

$$\theta = \frac{\mathcal{B} \pm \sqrt{\mathcal{B}^2 - 4\mathcal{A}\mathcal{C}}}{2\mathcal{A}} \tag{3.12}$$

If $\theta \leq 1$, then the differential domain of dependence is contained within the difference domain of dependence (Fig. 3-1a) and the step between node 0 and node 1 is stable. If $\theta > 1$, then the differential domain of dependence is not entirely contained within the difference domain of dependence (Fig. 3-1b) and the step between node 0 and node 1 will be unstable. Because the above analysis is approximate, a user supplied safety factor is applied to the value of θ determined by Eq. (3.12) in order to ensure that marginal stability does not present a problem.

If the above analysis indicates that the marching step size associated with the previously computed "primary" geometry is unstable, the GIM code steady state marching algorithm can automatically supply intermediate or "secondary" solution surfaces to ensure that the spatial marching proceeds in a stable fashion. The geometry of any required secondary solution surfaces is obtained via linear interpolation between primary geometry surfaces.

3.1.3 Decode Procedures

After the E vector has been obtained at a new station, the primitive variables ρ, u, v, w, H, and P must be decoded. This is accomplished in the following six steps:

Given

$$E = \begin{bmatrix} E_1 \\ E_2 \\ E_3 \\ E_4 \\ E_5 \end{bmatrix} = \begin{bmatrix} \rho u \\ \rho u^2 + P \\ \rho uv \\ \rho uw \\ \rho uH \end{bmatrix} \tag{3.13}$$

then the primitive variables are given by

1. $v = E_3/E_1$
2. $w = E_4/E_1$
3. $H = E_5/E_1$
4. $u = \left(\frac{\gamma}{\gamma+1}\right)\left(\frac{E_2}{E_1}\right) + \sqrt{\left(\frac{\gamma}{\gamma+1}\right)^2\left(\frac{E_2}{E_1}\right)^2 - 2\left(\frac{\gamma-1}{\gamma+1}\right)\left[H - \frac{1}{2}(v^2 + w^2)\right]}$ (3.14)
5. $\rho = E_1/u$
6. $P = \rho\left(\frac{\gamma-1}{\gamma}\right)\left[H - \frac{1}{2}(u^2 + v^2 + w^2)\right]$

This decode procedure is used after both the predictor and corrector steps in order to obtain the primitive variables from the E vector.

3.1.4 Boundary Conditions

After the primitive variables are obtained from the decode procedure, the boundary conditions must be enforced. In the inviscid flow of an ideal gas this consists of requiring that the component of velocity normal to any solid boundary vanish, i.e., the so-called free-slip tangency boundary condition. In the GIM code steady state marching algorithm, this is accomplished using a variation of Abbett's method (Ref. 3-8) described below.

At any solid boundary, the normal component of velocity must vanish, i.e.,

$$\bar{q} \cdot \bar{n} = 0 \qquad (3.15)$$

where $\bar{q}$ is the velocity vector with Cartesian components (u,v,w) and n is the outward pointing (into the computational domain) unit normal vector with components (n_x, n_y, n_z). In general, the velocity vector components obtained from the decode procedure, Eq. (3.14), will not satisfy Eq. (3.15) identically but will be rotated out of the surface tangent plane by a small angle δ. This angle can be determined by

$$\delta = \sin^{-1} \left(\bar{q} \cdot \bar{n} / q\right) \tag{3.16}$$

where q is the magnitude of the velocity.

If δ is positive, then Abbett's method indicates that an expansion wave is necessary to rotate the velocity vector back into the tangent plane but if δ is negative, then a compression wave is required. In practice, this means correcting the values of ρ, u, v, w, and P, calculated from MacCormack's method, by using shock wave and expansion wave properties. This is accomplished as follows:

1. Calculate ρ, u, v, w, H, and P from Eqs. (3.5a, 3.5b) and (3.14).
2. Calculate δ using Eq. (3.16).
3. If δ is positive, go to step 5.
4. δ negative indicates compression wave required.
   a. Compute oblique shock wave angle θ for deflection angle $|\delta|$ and Mach number $M^2 = q^2/(\gamma P/\rho)$ using Eqs. (150) from Ref. 3-9:

$$\sin^6\theta + b \sin^4\theta + c \sin^2\theta + d = 0$$

where

$$b = -\frac{M^2 + 2}{M^2} - \gamma \sin^2 \delta$$

$$c = \frac{2M^2 + 1}{M^4} + \left[\frac{(\gamma+1)^2}{4} + \frac{\gamma-1}{M^2}\right] \sin^2\delta \tag{3.17}$$

$$d = -\frac{\cos^2\delta}{M^4}$$

There are three roots of Eq. (3.17), the smallest of which corresponds to a decrease in entropy and is therefore discarded. The largest root corresponds to a strong oblique shock and is also discarded. The intermediate root corresponding to a weak oblique shock is the one of interest.

b. Compute the corrected static pressure P_c using Eq. (128) from Ref. 3-9:

$$P_c = P \frac{2\gamma M^2 \sin^2\theta - (\gamma-1)}{\gamma+1} \qquad (3.18)$$

c. Compute the entropy increase across the shock using Eq. (144) from Ref. 3-9:

$$\frac{\Delta s}{c_v} = \ln\left[\frac{2\gamma M^2 \sin^2\theta - (\gamma-1)}{\gamma + 1}\right] - \gamma \ln\left[\frac{(\gamma+1)M^2 \sin^2\theta}{(\gamma-1)M^2 \sin^2\theta + 2}\right] \qquad (3.19)$$

d. Compute the corrected density ρ_c using fundamental relationships:

$$\rho_c = \rho_u \left(\frac{P_c}{P_u}\right)^{1/\gamma} e^{-\left(\frac{\Delta s}{\gamma c_v}\right)} \qquad (3.20)$$

where subscript u indicates values immediately upstream.

e. Go to step 6.

5. δ positive indicates expansion wave required.

   a. Compute the total pressure P_{tot} based on upstream properties:

$$P_{tot} = P_u \left[1 + \frac{\gamma-1}{2} M_u^2 \right]^{\frac{\gamma}{\gamma-1}}$$

$$M_u^2 = q_u^2/(\frac{\gamma P}{\rho})_u \qquad (3.21)$$

   where subscript u indicates values immediately upstream.

   b. Compute the corrected Mach number M_c for deflection angle δ and Mach number $M^2 = q^2/(\gamma P/\rho)$ using Prandtl-Meyer Eq. (8.13) from Ref. (3-10):

$$\delta = \sqrt{(\frac{\gamma+1}{\gamma-1})} \left\{ \tan^{-1} \left[(\frac{\gamma-1}{\gamma+1}) (M_c^2-1) \right]^{1/2} - \tan^{-1} (M_c^2-1)^{1/2} \right\}$$

$$- \sqrt{(\frac{\gamma+1}{\gamma-1})} \left\{ \tan^{-1} \left[(\frac{\gamma-1}{\gamma+1}) (M^2-1) \right]^{1/2} - \tan^{-1} (M^2-1)^{1/2} \right\} \qquad (3.22)$$

   (Solution by Newton-Raphson iteration.)

   c. Compute the corrected static pressure P_c using isentropic relationships:

$$P_c = P_{tot} \left[1 + \frac{\gamma-1}{2} M_c^2 \right]^{-(\frac{\gamma}{\gamma-1})} \qquad (3.23)$$

d. Compute the corrected static density ρ_c using isentropic relationships:

$$\rho_c = \rho_u \left(\frac{P_c}{P_u} \right)^{1/\gamma} \tag{3.24}$$

e. Go to step 6.

6. Compute the corrected velocity magnitude q_c using total enthalpy relationship:

$$q_c = \sqrt{2\left[H - \left(\frac{\gamma}{\gamma-1}\right) \left(\frac{P_c}{\rho_c}\right) \right]} \tag{3.25}$$

7. Compute the tangential components of velocity u_T, v_T, and w_T by discarding the normal components and calculate the tangential velocity magnitude q_T:

$$\begin{aligned} u_T &= u - (\bar{q} \cdot \bar{n})\, n_x \\ v_T &= v - (\bar{q} \cdot \bar{n})\, n_y \\ w_T &= w - (\bar{q} \cdot \bar{n})\, n_z \\ q_T &= (u_T^2 + v_T^2 + w_T^2)^{1/2} \end{aligned} \tag{3.26}$$

8. Compute the corrected velocity componenst u_c, v_c, and w_c by scaling the tangential components by the ratio (q_c/q_T):

$$\begin{aligned} u_c &= \left(\frac{q_c}{q_T}\right) u_T \\ v_c &= \left(\frac{q_c}{q_T}\right) v_T \\ w_c &= \left(\frac{q_c}{q_T}\right) w_T \end{aligned} \tag{3.27}$$

The above procedure varies somewhat from that described by Abbett (Ref. 3-8) but retains the essential features. Unlike Abbett's approach which applied the boundary condition once after the predictor step and then dispensed with the corrector step, the GIM code steady state marching algorithm applies the above procedure after both predictor and corrector steps. The boundary geometry of the current station is used on the predictor step since the corrected flowfield boundary values will be used with metric and flow field information from the current station to compute the corrector step. After the corrector step has advanced the solution to the next station, then boundary geometry from the new station is used to correct the flowfield boundary values at the new station.

3.2 USER'S GUIDE

3.2.1 General

As detailed in previous sections, the GIM code steady state marching algorithm employs progressively assembled finite difference analogs during the integration process. This procedure differs considerably from that employed in the standard GEOM-MATRIX/MATQP-INTEG GIM code sequence. This resulted in the development of two new GIM code modules, GEOMD and INTEGH, for use in steady state marching problems. GEOMD is a specialized version of the standard GIM code GEOM module designed for use exclusively with integration modules that utilize progressively assembled finite difference analogs. INTEGH is the steady state hyperbolic integration module for the Euler equations. These two new modules are used together without any intervening matrix module. Both modules are described below together with a summary of the required input. Only those input items that differ from the standard GEOM and INTEG input are described in detail. For a detailed description of other input items and conventions, the user is referred to previously published GIM code literature (Refs. 3-11, 3-12, and 3-13).

3.2.2 Dynamic Dimensioner for GEOMD (DYNMAT)

GEOMD uses the same dynamic dimensioning module as does GEOM, namely DYNMAT (Ref. 3-13). All input is identical. The user should, however, set up the dynamic dimensioning input data as if running a quasi-parabolic (QP) problem.

3.2.3 Geometry Module (GEOMD)

The geometry module used with the GIM hyperbolic Euler solver (GEOMD) is a modification of the standard GIM GEOM module. Due to the use of progressively assembled difference analogs, all of the time consuming element matrix computations were removed, and no MATRIX module is required. The output has been made more readable and completely mirrors the input.

The purpose of the GEOMD module is two-fold: (1) construct the computational mesh via trivariate blending, and (2) provide the integration module with connectivity information for each node (i.e., an array which for each node gives the node numbers of its nearest neighboring nodes along the three coordinate lines).

The output information is essentially the same as in other versions with two minor exceptions. First, the boundary node counter which previously counted nodes with non-interior boundary flags (i.e., IB=9) now counts non-interior nodes and nodes with a connectivity which differs from the natural numbering scheme within any zone. This number can still be safely input as MNB in the dynamic dimensioner for the integration module. Secondly, these interior nodes with irregular connectivity are assigned a new boundary condition flag of IB=-9. This is ignored in the integrator, but allows these nodes to be traced in the GEOMD output.

GEOMD creates only a formatted FILE20 output file which contains geometry and connectivity information with several user input options. These are detailed in the following discussion of the input changes.

Chart 3-1 gives an abbreviated description of the GEOMD input data. The input changes from previous documentation are given in the following.

Card 2:	IFMT replaces ISTEP. IFMT controls the output to FILE20
IFMT=0	Full GIM code output with coordinates, flow angles, normal components and boundary condition flags
=1	Only Cartesian coordinates
>1	Cartesian coordinates and boundary flags
IMATRX=0	Connectivity array is computed and appended to FILE20 at each output record
=1	No connectivity array.

Card Type	
1	HEADER(I)*, I=1,72 (12A6)
2	NZONES, IDIM, IFMT, IMATRX, IMATE (5I5)
3	IWRITE, LWRITE, NWRITE (3I5)
4	NSECTS (I5)
5	MAPE(I), I=1,12 (12I5)
6	MAPS(I), I=1,6 (6I5)
7	(IBWL(I), I=1,6), ITRAIN (7I5)
8	(NNOD(I), I=1,3), (ISTRCH(I), I=1,3) (6I5)
9	DIVPI(I), I=1,3 (3E10.4)
10	[AETA(J,I), I=1, NNOD(J)], J=1, IDIM (8E10.4)
11	[(AC(I,K,J), I=1,8), K=1,5], J=1,4, or 12 (8E10.4)
12	[AS(I,J), I=1,8], J=1,6 (8E10.4)
13	(PT(I,J), I=1,5), J=1,4, or 8 (8E10.4)
14	[(PMAX(I,K,J) I=1,5), ETAMAX(K,J), K=1,4], J=1,4 or 12 (6E10.4)

Chart 3-1 - GEOMD Input Guide

---

[*] See GIM documentation for explanation of FORTRAN symbols, NASA CR 3157 and CR3369.

Card 3: Output Control

IWRITE and LWRITE are now incremental indices. This aids in limiting connectivity and debug output.

IWRITE=0 No intermediate print.

=N Intermediate print for every N^{th} node

LWRITE=0 No connectivity printout

=N Print connectivity array for every N^{th} node

Finally, notice that the card carrying the analog choice flags has been removed since the analog calculations are no longer performed in this module.

The GEOMD module is FORTRAN 5 compatible and can be run on any serial computer. In particular, the CYBER 730-Z machine at NASA-Langley can be used for most two-dimensional problems and three-dimensional problems with no more than approximately 900 nodes in a cross plane.

3.2.4 Dynamic Dimesioner for INTEGH (DYNDIM)

INTEGH uses the same dynamic dimensioning module as does INTEG, namely DYNDIM (Ref. 3-13). All dynamic dimensioner input, which should be set up as if running a quasi-parabolic (QP) problem, is identical except for the last input item, IDYN. This variable must be set to 1 for use with INTEGH, as opposed to the value of 0 used with the standard INTEG module.

3.2.5 Integration Module (INTEGH)

The GIM code steady state hyperbolic integration module, INTEGH, is used to integrate the Euler equations by the methodology described previously. The equations are integrated in space starting from the first upstream station (or plane) with a user-supplied flow field initialization.

The solution is then progressively "marched" downstream one plane at a time, the solution on each plane serving as the initial value surface for the integration to the next plane. The geometry and nodal connectivity information supplied by GEOMD via FILE20 is used to progressively assemble the finite difference analogs as required for each plane.

Since the geometry information is constructed by GEOMD before the integration process begins, it is quite possible that the spatial step size between the nodes of two planes may exceed that required for stability with the given flow field. The user can, therefore, direct INTEGH to monitor the spatial step size for stability considerations using the analysis of section 3.1.2 (see METHOD on card H2 below). Then if INTEGH detects that the spatial step size between two primary planes (supplied by GEOMD) is too large for stable integration at one or more nodes, it will supply intermediate "ghost" or secondary planes by interpolating between the primary planes. This ensures that the integration can continue in a stable manner with the given geometry. If the user is certain that the geometry and anticipated flow field conditions are such that the spatial step size will always be within stable limits, then INTEGH can also be directed to circumvent the stability analysis at each plane. However, limited experience has indicated that the calculations will fall apart almost immediately if the user is incorrect and the spatial step size is too large for stable integration.

In some instances, the integration process may not be able to successfully march to the next plane due to the presence of non-hyperbolic conditions, e.g., subsonic flow, flow reversal (separation), etc. INTEGH will normally detect these non-hyperbolic conditions, print an error message, and terminate the calculations. The user can, however, direct INTEGH to attempt to march through these regions (see NHPLIM on card H2 below). This can sometimes be accomplished successfully if the region of non-hyperbolic conditions is not too large or too severe in content.

C-2

Because it is a spatial marching integrator as opposed to the time-dependent integration of the standard INTEG module, the boundary condition treatment in INTEGH is of necessity somewhat different than that found in INTEG (see Section 3.1.4 for details). Because of this different treatment, all solid boundaries are treated as free-slip/tangency surfaces. Therefore, the user should note that INTEGH will only recognize and enforce boundary conditions of type 1 (axis node), type 3 (three-dimensional corner node), type 4 (free-slip/tangency node), and type 8 (free boundary node). Type 2 boundary conditions (no-slip/stagnation node) are treated as type 4. Type 0 boundary conditions (constant node) are not recognized at all and must not be used. In particular, the initial or inflow plane and the last or outflow plane should be treated with a type 9 boundary condition (no constraints) and not type 0, type 8, etc.

The input data required for INTEGH are summarized in Chart 3-2 . In much the same manner as with a quasi-parabolic integration run, the user supplies INTEGH with the geometry information from GEOMD on FILE20, the initial flowfield values on the first plane or inflow surface, and other necessary control variables. Many of these input variables for INTEGH are identical to those required for standard INTEG runs and are described in detail in Refs. 3-11, 3-12, and 3-13. Therefore, only those input variables peculiar to INTEGH are described in detail below.

Card H2:	METHOD controls the mode of operation of INTEGH.
METHOD = 1	No check of spatial step size for stability. Cross planes must be orthogonal to the x-axis.
= 2	Spatial step size checked for stability on each cross plane - secondary planes used if necessary. Cross planes must be orthogonal to the x-axis.
= 3	No check of spatial step size for stability. Cross planes need not be orthogonal to the x-axis.

Card Type	Parameter/Format
H1	ITITLE(I), I=1,80 (80A1)
H2	IDIM,METHOD,ITMAX,ITSAVE,ISTART,IOTYPE,IUNITS, IVISC,NHPLIM (9I5)
H3	DXFAC,EITOL (2E10.0)
H4	NPLT(I),MI2(I),MI3(I),NATT(I),L2(I),L3(1), I=1,NZONES+1 (6I5)
H5	GAM,WM,RK,EMU (4E10.0)
H6	KC(I), I=1,6 (6A5)
H7	NJ,INC,NTOT,ITAN,ITYPE (5I5)
H8	RI,UI,VI,WI,PI (5E10.0)
H9	N1,IC,NT,NP1,NPL,LSP (6I5)

Chart 3.2 - INTEGH Input Guide

= 4 Spatial step size checked for stability on each cross plane - secondary planes used if necessary. Cross planes need not be orthogonal to the x-axis.

ITMAX limits the number of iterations used to solve equations (3.5a, 3.5b) when cross planes are not orthogonal to the x-axis. ITMAX is ignored if METHOD .LT. 3.

ITMAX = Maximum number of iterations permitted. Nominal value = 5.

ITSAVE determines whether or not the flow field will be saved on FILE22.

ITSAVE = 0 Flow field not saved on FILE22.

= 1 Flow field saved on FILE22.

ISTART selects a cold start run or a restart run.

ISTART = 0 Cold start run.

= N Restart run beginning at plane number N. Flow field data read from FILE22.

IVISC selects the use of pseudo-viscous terms to assist in the capturing of strong shocks.

IVISC = 0 No pseudo-viscous terms used.

= 1 Pseudo-viscous terms used to assist capturing of strong shocks.
(Note: This option which uses a variation of Harten's method of Ref. 3-14 is not well exercised and should not be used at this time.)

NHPLIMM selects the number of cross planes in which non-hyperbolic conditions can occur before terminating the calculations.

NHPLIM = 0 Terminate calculations upon encountering non-hyperbolic conditions.

= N Up to N cross planes with non-hyperbolic conditions can be encountered before calculations will be terminated.

Card H3: DXFAC is a safety factor (analogous to DTFAC used in INTEG) applied to the spatial step size calculated from the stability analysis. DXFAC is ignored if METHOD = 1 or 3. Nominal value = 0.9 - 1.0.

EITOL is a relative tolerance used to terminate the iteration procedure used in equations (3.5a,3.5b) on cross planes which are non-orthogonal to the x-axis. EITOL is ignored if METHOD = 1 or 2. Nominal value = 1.0E-05.

Card H5: GAM is ratio of specific heats (same as GAMS1 in INTEG)

WM is the molecular weight of the fluid (same as WM1 in INTEG). WM can be left blank in which case RK must be supplied.

EMU is a multiplicative coefficient used with the pseudo-viscous option (IVISC = 1). Nominal value = 0.5 - 1.0
(Note: This option which uses a variation of Harten's method of Ref. 3-14 is not well exercised and should not be used at this time.)

Card H9: N1 is the node number of the first nodal point on this card to be printed during ouput. N1 = -1 terminates the reading of cards of type H9.

IC is the nodal number increment to N1 at which output is desired.

NT is the total number of nodes to be printed by this card type H9.

NP1 is the first plane to be effected by the values of N1, IC, and NT on this card.

NPL is the last plane to be effected by the values of N1, IC, and NT on this card.

LSP selects the printing or suppression of secondary plane output associated with planes NP1 through NPL. LSP is ignored if METHOD = 1 or 3.

LSP = 0 No secondary plane output is printed.

= 1 All secondary plane output associated with planes NP1 through NPL is printed.

3.3 SAMPLE CALCULATION: SHOCK EXPANSION TEST CASE

Figure 3-2 illustrates the details of a sample calculation performed with the GIM code steady state spatial marching algorith (INTEGH). This test case consists of uniform Mach 2.4 flow in a two-dimensional channel which encounters a 14.04 deg ramp followed by a complementing 14.04 degree turn back to the initial flow direction. An oblique shock wave with pressure ratio of approximately 2.3 forms at the intersection of the ramp and lower channel wall. This shock wave continues downstream and after reflecting off of the upper channel wall interacts with the expansion fan formed where the ramp turns back parallel to the upper channel wall. Figure 3-3 shows the computational grid consisting of 85 cross planes with 41 modes per plane. Figure 3-4 presents the velocity vectors computed by INTEGH. The dense packing of the velocity vectors highlights the well-defined shock wave. The expansion fan although present is less clearly discernable. Both the shock wave and the expansion fan can be seen, however, in Fig. 3-5 which is the same velocity vector plot as Fig. 3-4 but with every other vector masked out. Figures 3-6, 3-7, and 3-8 show the pressure, Mach number, and density contours, respectively, for this shock-expansion test case. The pressure and density contours have been normalized by their inflow values. Computational time for this case was approximatey 10^{-4} CPU sec per node. Due to the short vector lengths encountered (41 nodes per cross plane), it is anticipated that INTEGH will be even more efficient for larger problems.

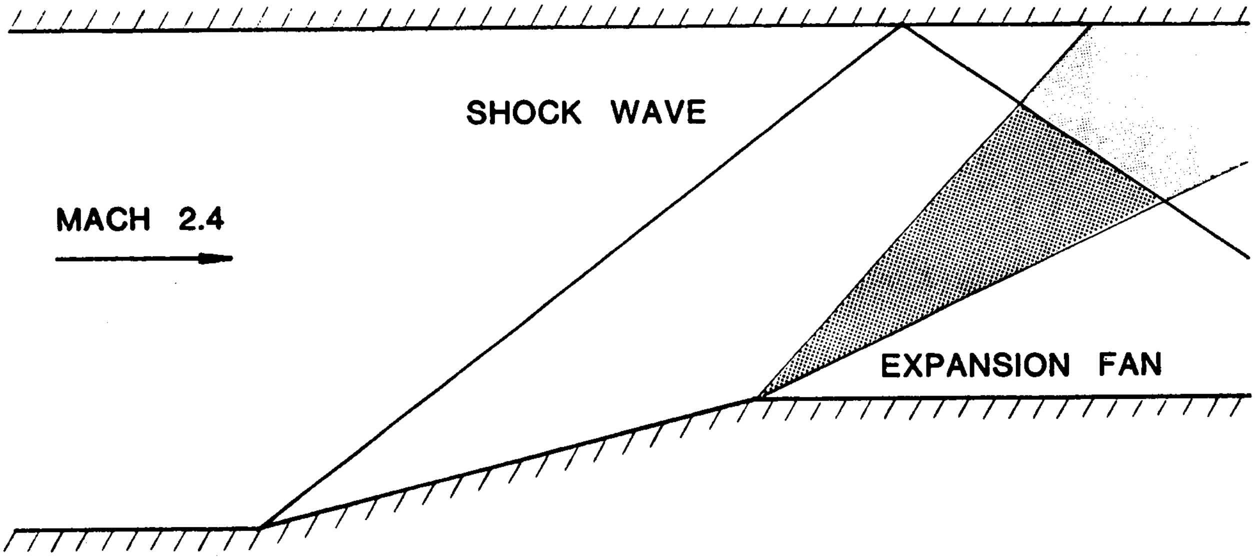

Fig. 3-2 - Shock Expansion Test Case (Diagram of Solution)

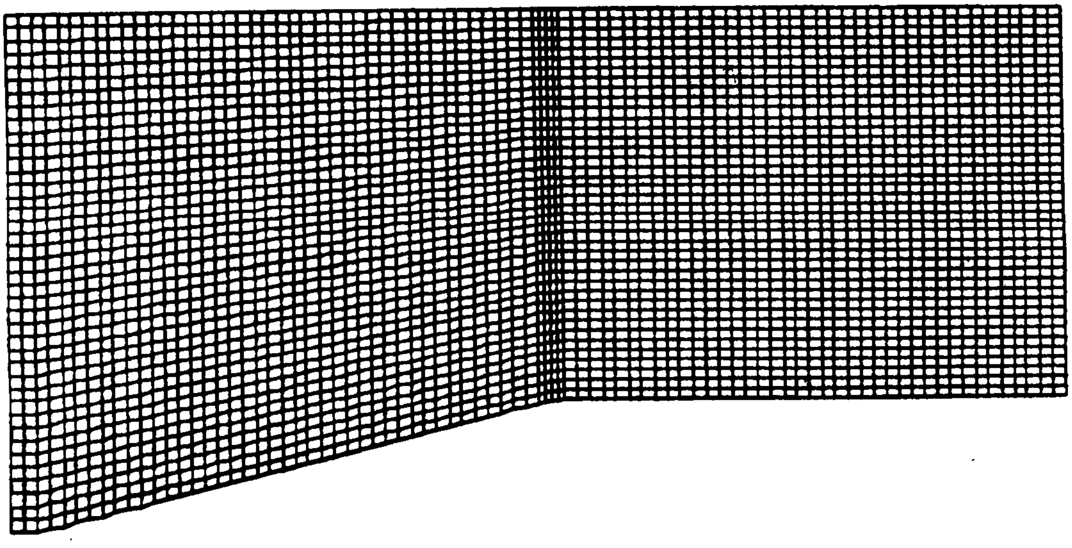

Fig. 3-3 - Shock Expansion Test Case (Computational Grid)

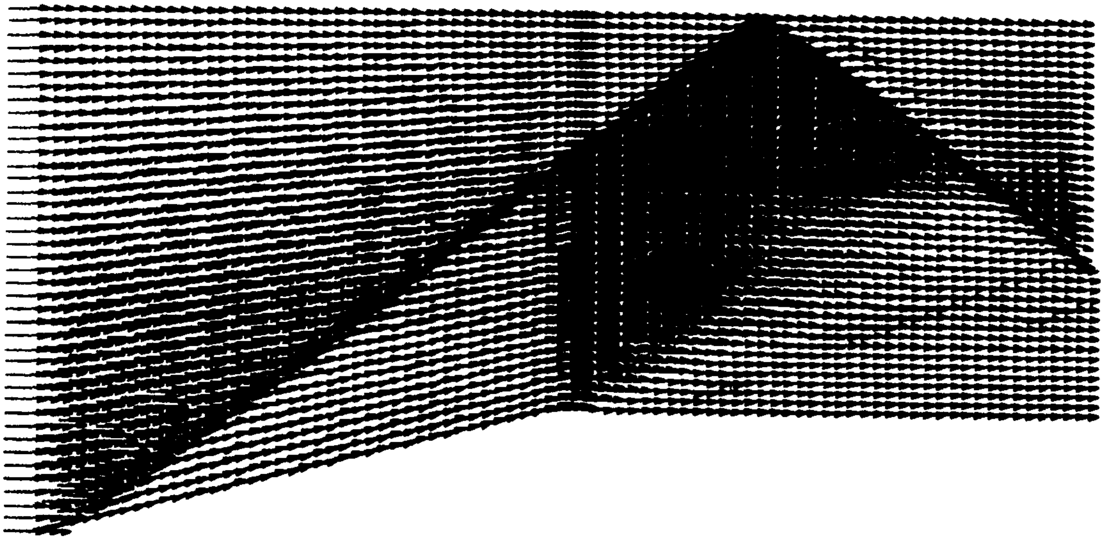

Fig. 3-4 - Shock Expansion Test Case (Velocity Vectors - Dense)

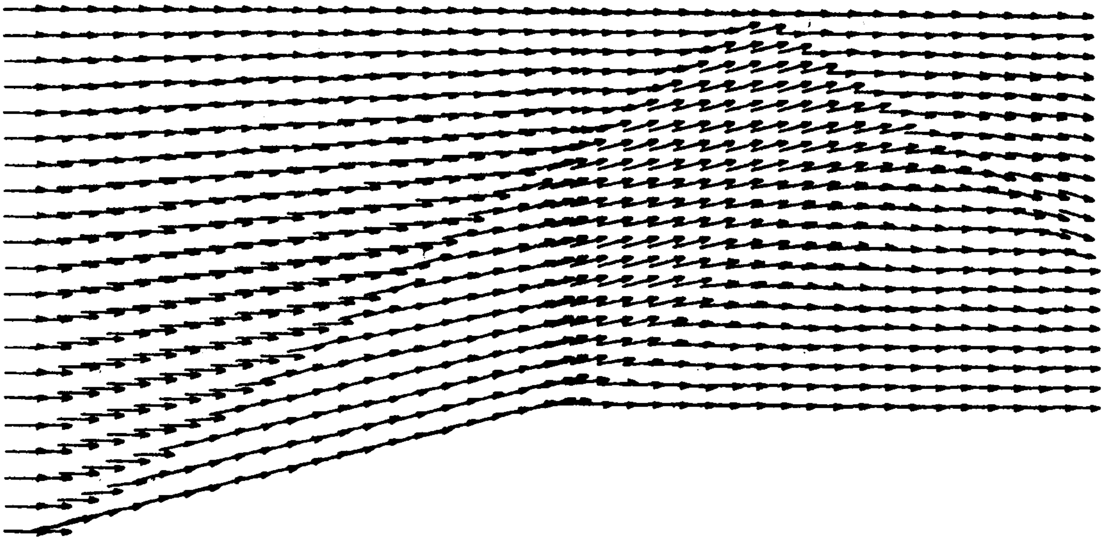

Fig. 3-5 - Shock Expansion Test Case (Velocity Vectors - Sparse)

PRESSURE CONTOURS STEADY STATE

ID	P/PO
1	1.1718
2	1.6967
3	2.0216
4	2.4465
5	2.8714
6	3.2963
7	3.7212
8	4.1461
9	4.5710
10	4.9959

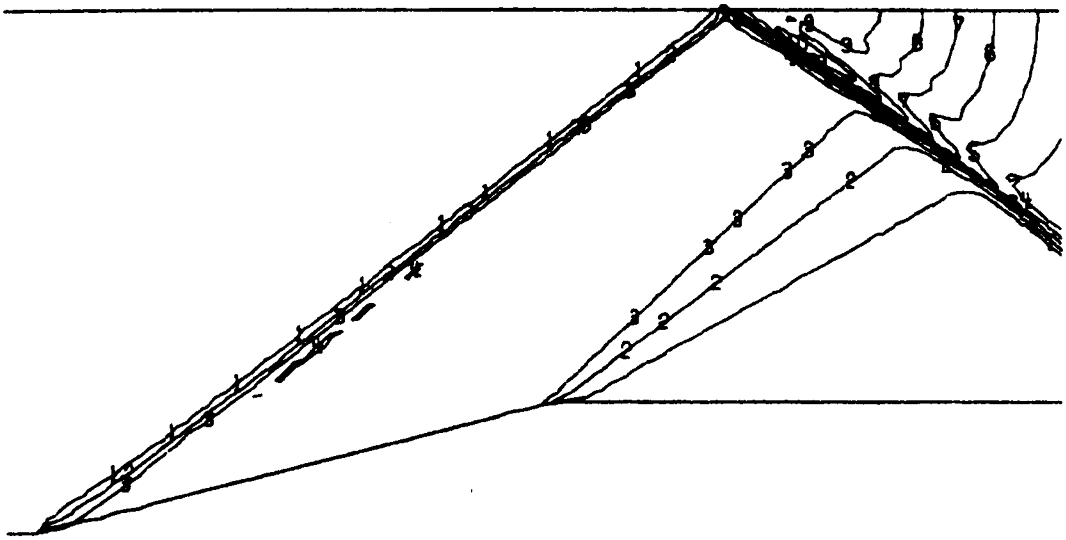

Fig. 3-6 - Shock Expansion Test Case (Pressure Contours)

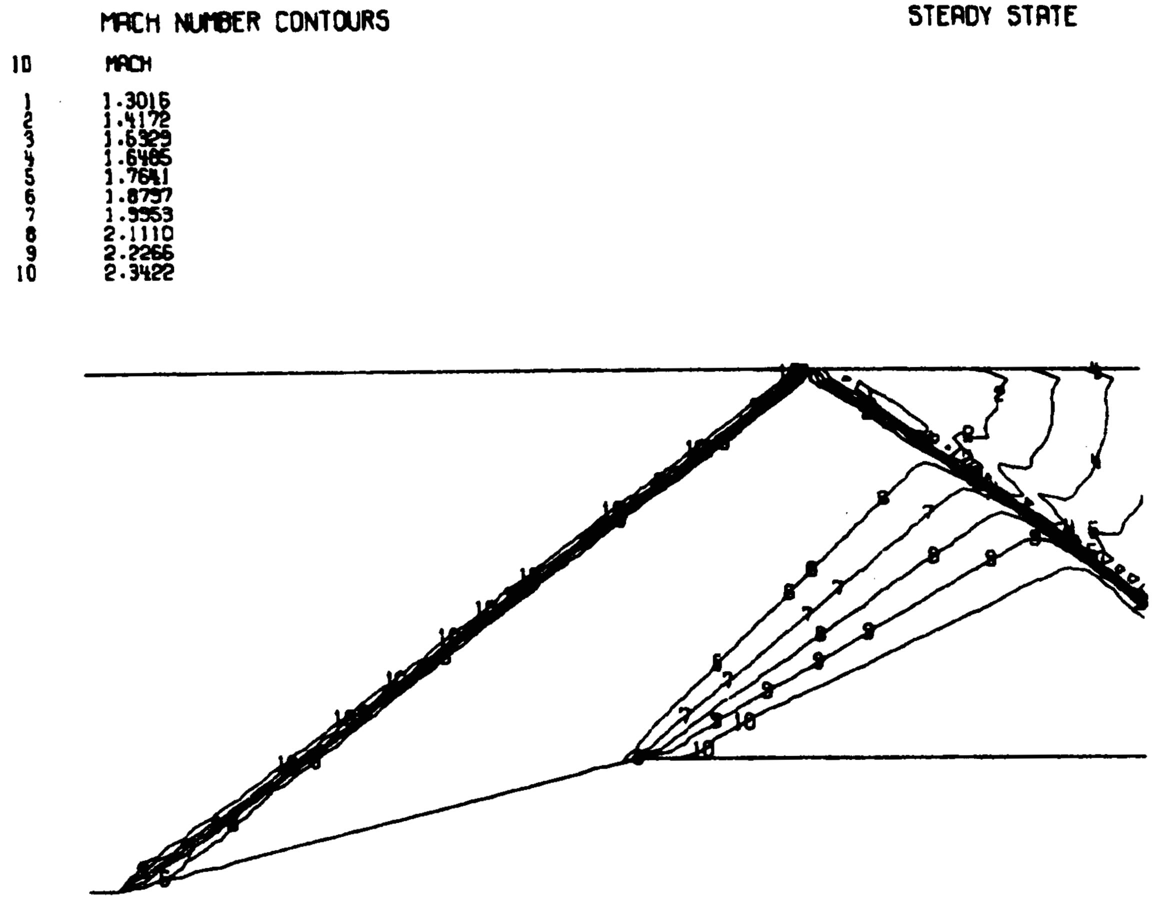

Fig. 3-7 - Shock Expansion Test Case (Mach Number Contours)

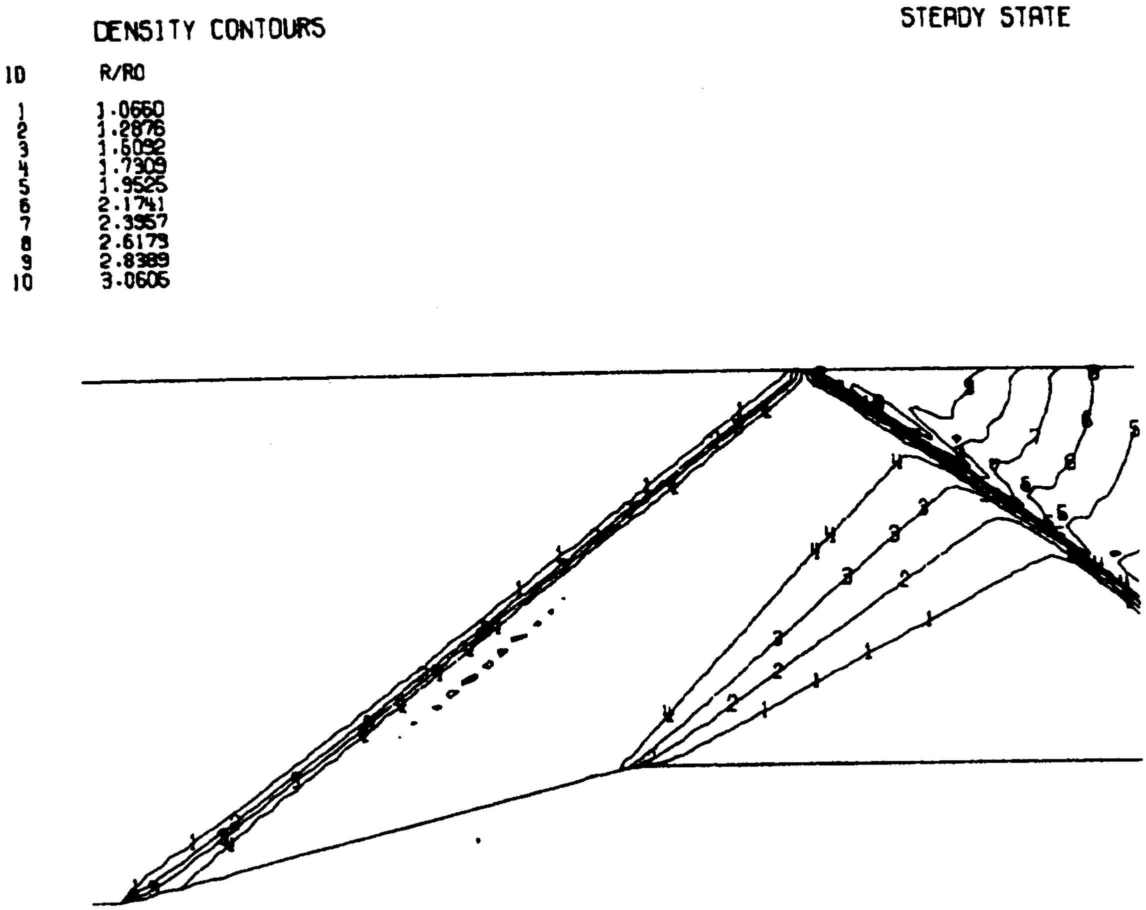

Fig. 3-8 - Shock Expansion Test Case (Density Contours)

3.4 REFERENCES FOR SECTION 3

3-1. Spradley, L.W., J.F. Stalnaker, and A.W. Ratliff, "Hyperbolic/Parabolic Development for the GIM-STAR Code," NASA CR-3369, Langley Research Center, Hampton, Va., December 1980.

3-2. Spradley, L.W., J.F. Stalnaker, and K.E. Xiques, "A Quasi-Parabolic Technique for Computation of Three-Dimensional Viscous Flows," AIAA Paper 81-0113, St. Louis, January 1981; also AIAA J., Vol. 20, No. 1, pp. 31-32, January 1982.

3-3. Xiques, K.E., E.G. Rawlinson, J.F. Stalnaker, and L.W. Spradley, "Computation of Three-Dimensional Inviscid Flow over a Hypersonic Missile Configuration Using the GIM Code," AIAA Paper 82-0248, Orlando, January 1982.

3-4. Stalnaker, J.F., and K.E. Xiques, "High Speed Aerodynamic Applications of the GIM Code," AIAA Paper 83-1801, Danvers, Mass., 1983.

3-5. Prozan, R.J., L.W. Spradley, P.G. Anderson, and M.L. Pearson, "The General Interpolants Method," AIAA Paper 7-642, Albuquerque, June 1977.

3-6. MacCormack, R.W., "The Effect of Viscosity in Hypervelocity Impact Cratering," AIAA Paper No. 69-354, May 1969.

3-7. Zucrow, M.J., and J.D. Hoffman, Gas Dynamics, Vol. II, Wiley, New York, 1977.

3-8. Abbett, M.J., "Boundary Condition Computational Procedures for Inviscid, Supersonic Steady Flowfield Calculations," Report No. 71-41, Aerotherm Corp., Mountain View, Calif., 30 November 1971. (Available as NASA CR-114446.)

3-9. "Equations, Tables, and Charts for Compressible Flow," NACA Report 1135 (1953).

3-10. Zucrow, M.J., and J.D. Hoffman, Gas Dynamics, Vol. I, Wiley, New York, 1976.

3-11. Spradley, L. W., and M.L. Pearson, "GIM Code User's Manual for the STAR-100 Computer," NASA CR-3157, November, 1979.

3-12. Spradley, L. W., J.F. Stalnaker, and A.W. Ratliff, "Hyperbolic/Parabolic Development for the GIM-STAR Code," NASA CR-3369, December, 1980.

3-13. Stalnaker, J. F., M.A. Robinson, E.G. Rawlinson, P.G. Anderson, A.W. Mayne, and L.W. Spradley, "Development and Application of the GIM Code for CYBER 203 Computer," NASA CR-3652, December, 1982.

3-14. Harten, A., "High Resolution Schemes for Hyperbolic Conservation Laws," J. Computational Physics, Vol. 49, No. 3, March 1983, pp. 357-393.

4. INVESTIGATION OF A SOLUTION-ADAPTIVE GRID ALGORITHM FOR THE GIM CODE

4.1 INTRODUCTION

The starting point of a numerical scheme for a digital computer is an array of finite points used to discretize the continuum. The treatment of fluid flows by these finite differencing methods has advanced tremendously in recent years due to production of advanced computing machines such as the CDC CYBER 203 and the CRAY. In a sense the machine advancements have preceded the methods advancements. The pacing item appears to be the very starting point itself, the generation of a finite mesh of points on which to write the discrete equation set.

We will not attempt to give a complete literature review in this report, as a separate report would be required for the extensive number of papers. The NASA-sponsored meetings at Langley (Reference 4-1) and Ames (Reference 4-2) contain articles of significance. The AIAA-sponsored meetings on Computational Fluid Dynamics (References 4-3 through 4-5) contain some articles on adaptive and multi-grid methods. The symposium, organized by Mississippi State University and sponsored by AFOSR and NASA (Ref. 4-6) provides a timely forum for this important topic of grid generation.

The GIM (Ref. 4-3) code solves the multi-dimensional Navier-Stokes equations for arbitrary geometric domains. The geometry module in the GIM code generates two- and three-dimensional grids over specified flow regions, establishes boundary condition information and computes finite difference analogs for later use in the numerical integration solution module. The grid generation technique can be classified as an algebraic equation approach as opposed to a differential equation approach. The grid algorithm uses multi-variate blending function interpolation of vector-valued functions which define the shape of the edges and surfaces bounding the flow domain. By employing blending functions which conform to the cardinality conditions, a unit cube can be mapped onto the flow domain, thus producing an intrinsic coordinate system for the region of interest. The intrinsic coordinate system facilitates grid spacing control to allow for nonuniform distribution of nodes in the flow domain.

The current state of the art in Computational Fluid Dynamics relies on grids that are fixed in time, i.e., stationary Eulerian frames. Optimum use of computer storage and CP time cannot be made a priori on a fixed grid. The advanced algorithms will require time-dependent grids that adapt themselves to the physics of the flow. The grid movement terms are well known and a number of codes already exist with these terms programmed. What is missing is a methodology, even an algorithm, to cluster the points, i.e., supply values for these known terms in the equations and to control movement of the points.

The objectives, then, of this research are:

- To fill some of the information gaps which exist in adaptive grid generation technology
- To provide a consistent treatment of grid generation and error control on physical domains, with nonuniform spacing
- To develop a practical algorithm for a self-adapting grid for Navier-Stokes solutions.

Our development will rely heavily on the General Interpolants Method (GIM) methodology, but the formulation and algorithm will be GIM independent for use by the general community.

4.2 FORMULATION

This work begins by considering the Euler equations in two space dimensions and time. Extension to viscous flows and the Navier-Stokes equations is straightforward. The basic equation set in x,y coordinates is

$$\frac{\partial U}{\partial t} + \frac{\partial E}{\partial x} + \frac{\partial F}{\partial y} = 0$$

$$U = \begin{bmatrix} \rho \\ \rho u \\ \rho v \\ \rho \mathcal{E} \end{bmatrix} \tag{4.1}$$

$$E = \begin{bmatrix} \rho u \\ \rho u^2 + P \\ \rho u\, v \\ (\rho \mathcal{E} + P)\, u \end{bmatrix} \qquad F = \begin{bmatrix} \rho v \\ \rho v u \\ \rho v^2 + P \\ (\rho \mathcal{E} + P)\, v \end{bmatrix}$$

Here x,y,t are the spatial coordinates and t is time. The flow variables are ρ = density, u,v = velocity components in x,y directions, respectively, $\mathcal{E}$= total energy and P = static pressure.

A set of "boundary conforming" coordinates is generated by a geometry module GIM code to simplify the boundary condition procedures and difference scheme. A computation domain is constructed with uniformly spaced rectangular coordinates and the physical coordinates are mapped onto this domain.

$$(x,y,t) \longrightarrow (\xi, \eta, \tau)$$

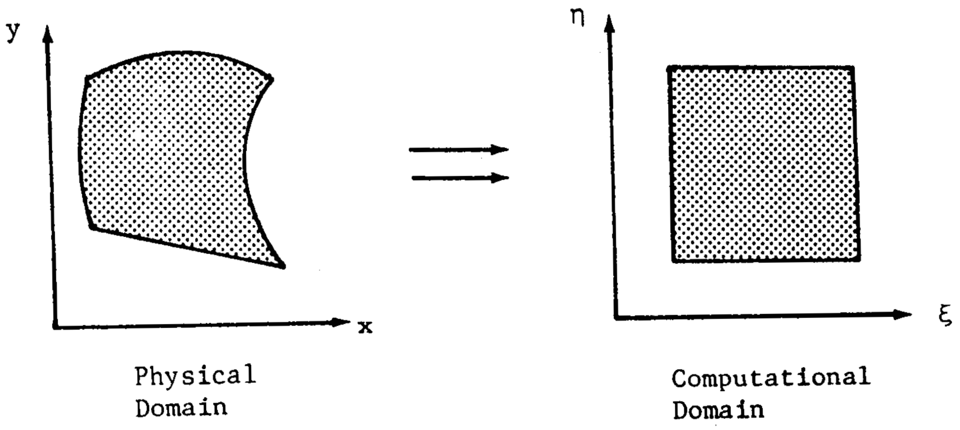

Insertion of a general curvilinear coordinate transformation, keeping all time-dependent terms, results in the following equation set:

$$\frac{\partial U^*}{\partial \tau} + \frac{\partial E^*}{\partial \xi} + \frac{\partial F^*}{\partial \eta} = 0$$

where

$$\begin{aligned} U^* &= JU \\ E^* &= y_\eta[E - x_\tau U] - x_\eta[F - y_\tau U] \\ F^* &= x_\xi[F - y_\tau U] - y_\xi[E - x_\tau U] \end{aligned} \qquad (4.2)$$

Here J is the determinate of the transformation Jacobian

$$J = x_\xi y_\eta - x_\eta y_\xi \tag{4.3}$$

and x_ξ, y_ξ, x_η, y_η are the metric coefficients and

$$x_\tau = \frac{\partial x}{\partial \tau}, \; y_\tau = \frac{\partial y}{\partial \tau}$$

are the coordinate movement velocities in the x,y directions, respectively.

Thus the coordinates in physical space can move in time according to the prescription for x_τ, y_τ. This can be from a moving boundary or from interior point movement via an adaptive grid algorithm. At each time step, the physical grid is moved and remapped onto the fixed computational grid via the metrics and the Jacobian. The finite difference program for solving the equations is thus unaltered, and the effects of coordinate movement is taken into account in the metric data.

Generation of these metric data, and in particular the Jacobian J, must be done with extreme caution. This is discussed in detail by Thomas and Lombard (Reference 4-7) where they introduce the Geometric Conservation Law (GCL). In this procedure, a differential equation is solved for the Jacobian J using the same difference scheme as used on the flow equations. This results in total consistency of numerics and preserves uniform flow exactly. In an adaptive grid scheme this will be very important to a good working code. We thus append the following equation to our set.

$$\frac{\partial J}{\partial \tau} + \frac{\partial}{\partial \xi}\left[x_\eta y_\tau - y_\eta x_\tau\right] + \frac{\partial}{\partial \eta}\left[y_\xi x_\tau - x_\xi y_\tau\right] = 0 \tag{4.4}$$

To complete the formulation, we need a prescription for determining the coordinate movement x_τ, y_τ. For the first version of the GIM adaptive grid code, we use the scheme of Rai and Anderson (References 4-8 and 4-9). In one space dimension, this scheme is simply written as

$$x_\tau\Big|_i = K x_\xi \left[\sum_{j=i+1}^{N} f_{ij} - \sum_{j=1}^{i-1} f_{ij} \right] \tag{4.5}$$

$$f_{ij} = \frac{|e_j| - |\bar{e}|}{r_{ij}^M}$$

where e_j is a measure of the error at node j, r_{ij} is a distance between nodes i and j, and K,M are chosen constants. The current code uses this scheme in one of three ways:

- Coordinate movement in x direction only
- Coordinate movement in y direction only, and
- Coupled movement in both directions.

The functions e_j present one of the major difficulties in using this scheme. Accurate determination of the truncation error in our scheme has not been done yet. In the current code, the e_j functions are set to the local pressure gradient,

$$e_j = \frac{\partial P}{\partial \xi}\Big|_j$$

Control of the grid speeds, x_τ, y_τ is also a concern with this scheme. Control of the speed is currently done with the constant K, chosen a priori in the manner of Rai and Anderson (References 4-5 and 4-6).

The MacCormack explicit, unsplit, finite difference scheme (Reference 4-10) is used to solve all differential equations. Boundary conditions consist of fixed in-flow, supersonic one-sided out-flow and solid wall free-slip (tangency). The grid velocities are forced to obey wall tangency so that the boundary points stay in the domain.

The computation proceeds as follows:

- An initial grid is prescribed on physical space by the grid coordinate generator.
- These coordinates are mapped (numerically) onto the computational domain and the metric data calculated. The Jacobian J is initialized by the algebraic definition (Eq. (4.3)).
- The grid velocities are set to zero.
- Equation set (4.2) is formed and solved for U^* by the MacCormack method. Note that $U^* = (\rho J, \rho u J, \rho v J, \rho \mathcal{E} J, J)$.
- Boundary conditions are applied.
- The vector U^* is decoded for ρ, u, v, $\mathcal{E}$, J.
- The pressure P is determined from the ideal gas law.
- Grid velocities are updated from Eq. (4.5).
- The coordinates x,y are moved using a first-order scheme

$$x^{n+1} = x^n + x^n_\tau \, \Delta\tau,$$

$$y^{n+1} = y^n + y^n_\tau \, \Delta\tau$$

- New metrics are determined, x_ξ, x_η , y_ξ , y_η from the known coordinate transformation.
- Equations (1) are formed (now with $x_\tau \neq 0$, $y_\tau \neq 0$).
- The solution process is repeated until convergence is achieved to steady state or for a fixed number of time steps.

4.3 RESULTS

An example case, simple in nature, is shown here to illustrate that this formulation does work. This example case is a standing shock wave in a duct.

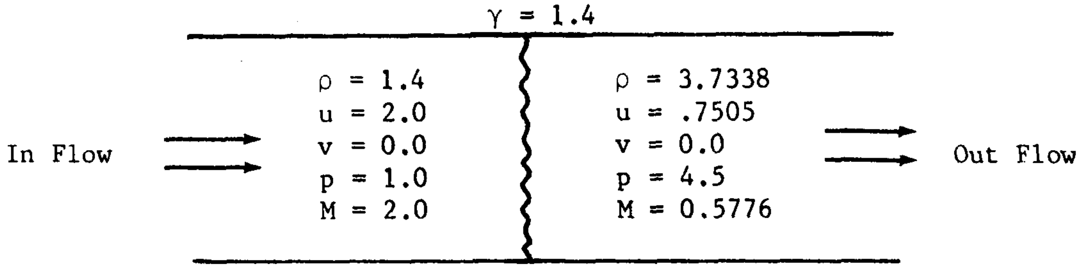

The shock was placed in the axial center of a fixed grid of 26 x 5 points (5 points in y direction for simplicity). The code was run until the grid velocity x_τ dropped six orders of magnitude from its peak value.

Converged results are shown in Figure 4-1. The left figure is the MacCormack solution for a fixed grid, i.e., $x_\tau = 0$ for all τ. The right figure shows the result for an adaptive grid. The plots are pressure versus x with the grid point positions shown at the bottom for reference. As seen here, the grid motion resulted in points being moved closer to the shock discontinuity and also resulted in a smoother calculated shock, i.e., the overshoot is almost gone.

Figure 4-2 shows the same problem run with 51 axial points to test the algorithm on a finer mesh. The left figure shows virtually the same results for grid movement, but of course, a steeper calculated shock. The right plot on Figure 4-2 is an example of this problem when the constraint on x was relaxed. The grid speeds get too fast, the points cross one another, and the entire solution goes unstable.

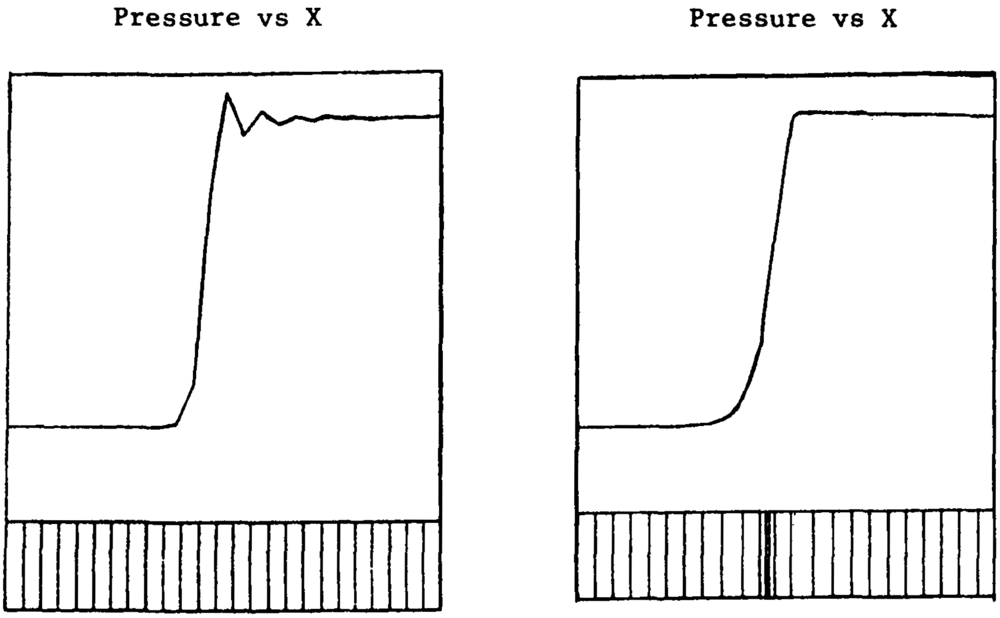

Fixed Grid **Adaptive Grid**

Figure 4-1. One-dimensional shock tube problem-adaptive grid solution

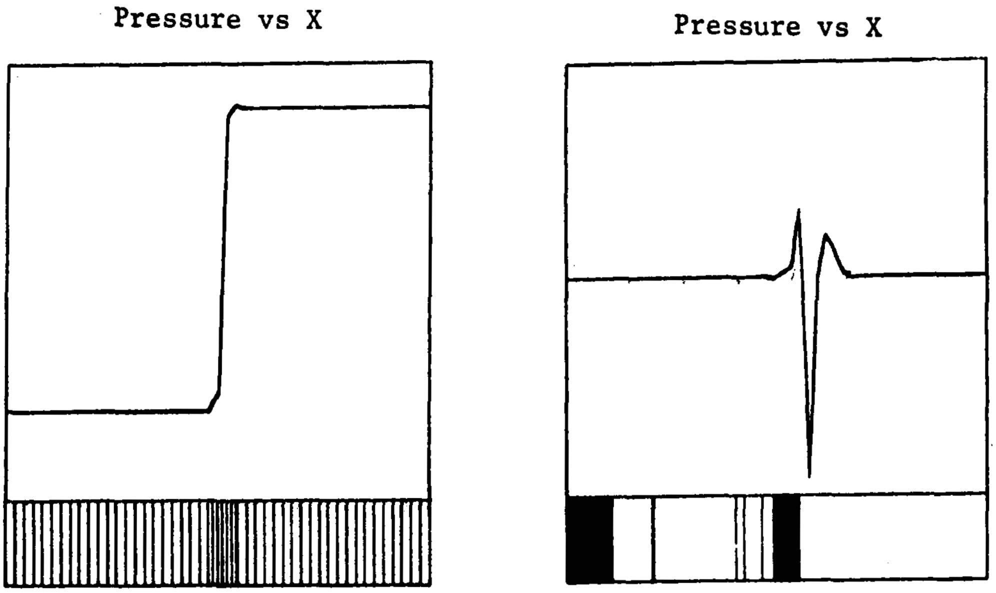

Converged Case
(Fine Mesh)

Unstable Case
(Too Little Constraint on x_T)

Figure 4-2. One-dimensional shock tube problem-adaptive grid solution

4.4 EXTENSION TO HIGHER DIMENSIONS

The work on adaptive grids done under the NASA-Langley contract was restricted to the one-dimensional development. This work is currently being extended under Lockheed's Independent Research Program. Two- and three-dimensional formulations have been accomplished and coding is now in progress. Documentation of the multi-dimension work will be done under the Independent Research Program.

4.5 REFERENCES FOR SECTION 4

1. Spradley, L.W., J.F. Stalnaker and A.W. Ratliff, "Solution of the Three-Dimensional Navier-Stokes Equations on a Vector Processor," AIAA J., Vol. 19, No. 10, October 1981.
2. Spradley, L.W., J.F. Stalnaker, and K.E. Xiques, "Quasi-Parabolic Technique for Spatial Marching Navier-Stokes Computations," AIAA J., Vol. 19, No. 12, December 1981.
3. Anderson, P.G., and L.W. Spradley, "Finite Difference Grid Generation by Multivariate Blending Function Interpolation, NASA CP-2166, October 1980.
4. Thomas, P.D., and C.K. Lombard, "Geometric Conservation Law and Its Application to Flow Computations on Moving Grids," AIAA J., Vol. 17, No. 10, October 1979.
5. Rai, M.M., and D.A. Anderson, "The Use of Adaptive Grids in Conjunction with Shock Capturing Methods," AIAA Paper 81-1012, June 1981.
6. Rai, M.M. and D.A. Anderson, "Grid Evaluation in Time Asymptotic Problems," J. Comp. Physics, Vol. 43, 1981, pp. 327-344.
7. MacCormack, R.W., "The Effect of Viscosity in Hypervelocity Impact Cratering," AIAA Paper 69-354, May 1969.

5. TURBULENCE MODELING IN THE GIM CODE

5.1 INTRODUCTION

This section updates the modifications and additions to the GIM code turbulence models since their last documentation (Ref. 5-1). The algebraic eddy viscosity model of Baldwin and Lomax (Ref. 5-2) has been extended to two-dimensional flows bounded by more than one wall. The option is also provided to apply the model selectively in different regions of the flow. These changes are discussed in the next section. The third section details the final form of the wall function boundary conditions chosen for the turbulent kinetic energy (TKE) differential equation model, and describes their use and initialization.

The turbulence models exist as files of UPDATE directives to the basic GIM code INTEG module. This approach was adopted so as to not adorn the basic module with often unused subroutines and so that the models could be coded in a manner compatible with the INTEG module but not necessarily with each other since only one is used at a time.

5.2 IMPROVEMENTS TO THE BALDWIN/LOMAX MODEL

The Baldwin/Lomax algebraic eddy viscosity model in the GIM code has been extended to allow the user to apply the model within as many as ten different regions along a cross-flow line of nodes. This approach allows the user to compute in regions with more than one wall and/or selectively apply the model to different regions of the flow domain. As previously documented, the model can be used for axisymmetric and two-dimensional flows in either the quasi-parabolic or elliptic modes of GIM calculation. It is assumed that one set of grid lines lies approximately in a cross-flow direction (η_2 for QP calculations).

These features are implemented by modifying DATA statements within the UPDATE file itself. The variables which need to be changes are

JREG = The number of regions along a line of nodes

J1RG(I) = The starting node for Region I along a line of nodes

JLRG(I) = The number of nodes included in Region I.

These variables are presently set for one region extending over the full line of nodes. J1RG is a local node number; i.e., $1 \leq$ J1RG $\leq$ number of nodes in the cross-flow η direction.

Experience indicates that the model must be modified to some extent for almost every calculation performed. This is a result of the coupling of the generality of the GIM methodology and the specific nature of most algebraic turbulence models. To provide further versatility (especially in geometrically complex problems requiring more than one zone), the user can modify the defining statements of the following two variables:

JFRST = The global (GEOM-assigned) starting node number in the region along the line of nodes being computed.

NNY = The number of nodes to be included in the computation.

In the general case NNY = JLRG.

A simple example of flow in a region between two walls may serve to clarify the use of these regions. The problem is illustrated in Fig. 5-1. η_1 is the streamwise direction and η_2 is the cross-flow direction. Here we choose to divide the flow into two regions at the 25th node along the 50 node η_2 line. The modified DATA statements in the update file for this case should appear as

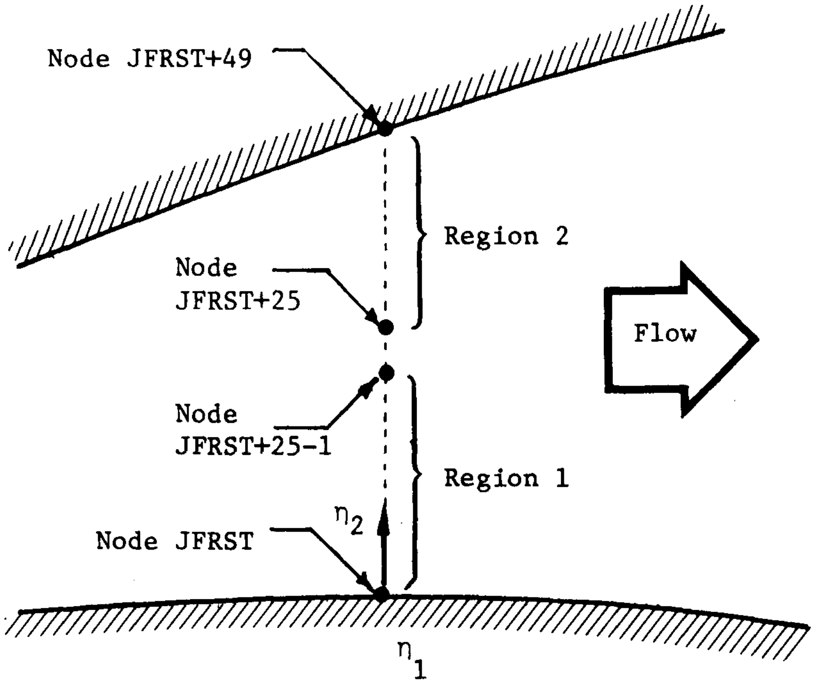

Fig. 5-1 - Flow in a Two-Dimensional Region Bounded by Two Walls

```
DATA JREG/2/
DATA J1RG/1,26,8*0/
DATA JLRG/25,25,8*0/.
```

In the event that the minimum velocity within the region, which the model uses as a reference location, does not occur at one of the end points of the region (for example, this situation could occur in wake flows) the model will subdivide the region at the minimum point automatically.

Finally, a word of caution. Although the above may seem complex, it has been found to be a coding arrangement ammenable to the modifications which seem necessary with almost every new problem. It was coded in this form so as not to disturb the input to the baseline model and at the same time to require considerable user preparation prior to modification.

5.3 BOUNDARY CONDITIONS FOR THE GIM/TKE MODEL

The boundary conditions for the two-equation turbulent kinetic energy TKE model in the GIM code have been finalized. They consist of wall function descriptions of the behavior of the momentum, turbulent kinetic energy, k, and the rate of dissipation of the turbulent kinetic energy, ε. These conditions override the type 2 (no-slip) boundary conditions in the code when the TKE model updates are applied. The model can be used for axisymmetric, two- and three-dimensional elliptic or quasi-parabolic calculations. This section will describe the form of these boundary conditions and their application in the code. To date, no test cases have been run using this model and the need for artificial damping to stabilize the time-iterative solution of these equations has not been studied. The form of the damping terms has not been derived.

Wall function boundary conditions for differential equation turbulence models allow these more complex and storage-intensive models to be computed without resolving the behavior of the laminar sublayer which necessitates very fine meshes and large number of nodes. It is assumed that the first node off the wall in such calculations lies either in the laminar sublayer or the logarithmic "law-of-the-wall" region. The wall functions in the GIM/TKE model are modeled after those of Taylor, Thomas, and Morgan (Ref. 5-3) written in a compressible form. These functions are applied at type 2 boundaries for the momentum, k and ε equations. The wall functions are given in Fig. 5-2. For the momentum equations the computed flow direction is constrained to be tangent to the wall and the magnitude of the momentum is computed from the wall function.

The variable viscosity flags are input as follows for the GIM/TKE model:

Momentum:

$$\rho q^{+} = \begin{cases} \rho\eta^{+} & ; \quad 0 \le \eta^{+} < 5 \\ \rho(5.0 \; \ell n\eta^{+} - 3.05)\,(\tau_w/|\tau_w|); & 5 \le \eta^{+} < 30 \\ \rho(2.5 \; \ell n\eta^{+} + 5.5)\,(\tau_w/|\tau_w|) & ; \quad \eta^{+} < 30 \end{cases}$$

Turbulent Kinetic Energy

$$(\rho k)_w = |\tau_w|/C_\mu^{1/2}$$

Dissipation of TKE

$$(\rho\varepsilon)_w = C_\mu \, (k_w)^{3/2}/\kappa\eta$$

where

$$\tau_w = \mu_L \, (\vec{n} \cdot \nabla)\,(\vec{t} \cdot \vec{V}) \qquad \eta^{+} = (\rho\eta/\mu_L)\sqrt{|\tau_w|/\rho}$$

$$q^{+} = \rho q/\sqrt{|\tau_w|/\rho} \qquad q = |\vec{V}|$$

$$\kappa = 0.42$$

Fig. 5-2 - GIM/TKE Wall Functions

$$VF(3) = C_\mu = 0.09$$

$$VF(4) = C_{\varepsilon 1} = 1.44$$

$$VF(5) = C_{\varepsilon 2} = 1.92$$

$$VF(6) = Pr_t = 0.9$$

$$VF(7) = \mu_T/\mu_L = 10 \text{ to } 100$$

$$VF(8) = q'/q = \text{a few percent}$$

where C_μ, $C_{\varepsilon 1}$ and $C_{\varepsilon 2}$ are constants in the model, Pr_t is the turbulent Prandtl number, μ_T/μ_L is the ratio of turbulent to laminar viscosity, and q'/q is the ratio of turbulent fluctuations of velocity to the magnitude of velocity. The latter two quantities are used in initialization of the turbulence quantities. Throughout the flow k and ε are initialized from input flow quantities as

$$k = \frac{1}{2} [q \cdot (q'/q)]^2$$

$$\varepsilon = \rho C_\mu k^2/\mu_T$$

where μ_T is determined from μ_L and VF(7). These quantities are insufficient to initialize the magnitude of the momentum at the wall points. Here we must assume the normal distance of the first node point from the wall. In the code it is assumed that the first node is one-tenth the normal grid spacing from the wall, i.e.,

$$\eta_w = (n_x \Delta x + n_y \Delta y + n_z \Delta z)/10$$

where n_x, n_y, and n_z are the components of the normal to the surface at the wall node and Δx, Δy and Δz are the grid spacings at that node. The dimensionless speed becomes

$$q^+ = \sqrt{\frac{2}{C_\mu^{1/2}}}/(q'/q)$$

from this the dimensionless normal distance from the wall can be calculated from the wall functions as

$$\eta^+ = \begin{cases} q^+ & ; \quad 0 \le q^+ < 5 \\ \exp[(q^+ + 3.05)/5.0] & ; \quad 5 \le q^+ < 14 \\ \exp[(q^+ - 5.5)/2.5] & ; \quad q^+ \ge 14 \ . \end{cases}$$

Finally, the dimensional speed at the wall becomes

$$q = \frac{\mu_T}{\rho} \frac{\eta^+}{\eta_w} \frac{q^+}{(\mu_T/\mu_L)}$$

The energy is initialized consistant with the input pressure and density and the above speed. It is necessary for the user to input type 0 (fixed) boundaries in a consistant fashion.

5.4 REFERENCES FOR SECTION 5

5-1. Stalnaker, J.F., M.A. Robinson, E.G. Rawlinson, P.G. Anderson, A.W. Mayne, and L.W. Spradley, "Development and Application of the GIM Code for the CYBER 203 Computer," NASA CR-3652, December 1982.

5-2. Baldwin, B.S., and H. Lomax, "Thin Layer Approximation and Algebraic Model for Separated Turbulent Flow," AIAA Paper 78-257, Huntsville, Ala., January 1978.

5-3. Taylor, C., C.E. Thomas, and K. Morgan, "Modeling Flow over a Backward-Facing Step Using the F.E.M. and the Two-Equation Model of Turbulence," International Journal for Numerical Methods in Fluids, Vol. 1, No. 4, October-December 1981, pp. 295-304.

Appendix A

GENERATION OF RATE CONSTANTS FOR A GLOBAL HYDROGEN-AIR COMBUSTION MODEL

Appendix A

A.1 INTRODUCTION

The analysis of non-reacting flow fields is still a difficult task, even with modern computational techniques. The task is even more difficult when reacting flows have to be considered. Realistic modeling of finite rate reaction systems usually requires the consideration of numerous chemical species, and often even more numerous reaction processes describing the interaction of the various species. This, in some cases, drastically increases computational time, and always increases program storage requirements. It is therefore of interest to devise procedures which can be used to establish reduced or global reaction models which are capable to faithfully reproduce the results of detailed and complete models, in spite of using only a limited number of species and reaction equations. Provided that such a global mechanism can be defined, which is probably more a matter of proper judgement than of computation, a systematic procedure to evaluate the necessary global rate constants is described here. The specific case of hydrogen-air combustion in a supersonic flow is considered, but the procedure should be applicable to arbitrary reaction systems.

A.2 METHODOLOGY

The application of the methodology to be described assumes the availability of a time-dependent finite rate reaction computer code which can compute the evolution of the species composition and the temperature as a function of time during a combustion process. A one-dimensional, inviscid pre-mixed calculation suffices for this purpose.

Let us assume that the full set of species and reactions to be reduced (or "globalized") is given by m = 1,...,NR reactions involving i = 1,...,NS species, i.e.,

$$\sum_i \nu_{i,m} A_i \overset{k_{f,m}}{\rightleftharpoons} \sum_i \nu'_{i,m} A_i \tag{A.1}$$

where the A_i denotes the species chemical symbol and the $\nu_{i,m}$ and $\nu'_{i,m}$ are the stoichiometric coefficients of the reactants and the products for the m^{th} reaction, respectively. $k_{f,m}$ denotes the forward rate constant for the m^{th} reaction.

The net rate of production for any species A_i participating in reaction m (i.e., $\nu'_{i,m} - \nu_{i,m} \neq 0$) is then given by

$$\dot{w}_{i,m} = (\nu'_{i,m} - \nu_{i,m}) \dot{w}_m \tag{A.2}$$

where

$$\dot{w}_m = k_{f,m} \left[\prod_i C_i^{\nu_{i,m}} - \frac{1}{K_{c,m}} \prod_i C_i^{\nu'_{i,m}} \right] \tag{A.3}$$

and where we have made use of the relation relating the forward and backward rate constants through the concentration equilibrium constant, viz.

$$K_{c,m} = \frac{k_{f,m}}{k_{b,m}} \tag{A.4}$$

The total net rate of production for species from the set of m reactions is then given by summing the contributions $w_{i,m}$ from (A.2) over all m reactions, i.e.,

$$\dot{w}_i = \sum_m \dot{w}_{i,m} \tag{A.5}$$

Now let us assume that the above described full set ($i=1,\ldots,NS$, $m=1,\ldots,NR$) is to be replaced by an equivalent, but reduced set of $j=1,\ldots,\widehat{NS}$ species and $n=1,\ldots,\widehat{NR}$ reactions, where $\widehat{NS} < NS$ and, preferrably, $\widehat{NR} \ll NR$. The question that arises is, what are the rate constants for the postulated reduced set of reactions? Assuming that by some reasoning a reduced set of species and reactions has been defined, the latter is described by

$$\sum_j \nu_{j,n} A_j \xrightleftharpoons{k_{f,n}} \sum_j \nu'_{j,n} A_j \tag{A.6}$$

and, as before,

$$\dot{w}_{j,n} = (\nu'_{j,n} - \nu_{j,n}) \dot{w}_n \tag{A.7}$$

where

$$\dot{w}_n = k_{f,n} \left[\prod_i C_j^{\nu_{j,n}} - \frac{1}{K_{c,n}} \prod_j C_j^{\nu'_{j,n}} \right] \tag{A.8}$$

Again, the total net rate of production for species j from the reduced set of reactions is obtained as before by summing the contributions of all n reactions such that

$$\dot{w}_j = \sum_n \dot{w}_{j,n} = \sum_n \Delta\nu_{j,n} \dot{w}_n \tag{A.9}$$

where $\Delta\nu_{j,n}$ is defined as

$$\Delta\nu_{j,n} \equiv \nu'_{j,n} - \nu_{j,n} \tag{A.10}$$

For j species comprising the reduced or "globalized" set, Eq. (A.9) represents a set of j simultaneous linear equations for the unknown $\dot{w}_n$, i.e.,

$$(\Delta\nu_{j,n}) \dot{w}_n = \dot{w}_j \tag{A.11}$$

where $(\Delta\nu_{j,n})$ represents a coefficient matrix, and $\dot{w}_n$ and $\dot{w}_j$ represent column vectors.

In general, provided that n=j and that the coefficient matrix is non-singular the above set can be solved, either by successive elimination (triangulation) or by using Cramer's rule, in which case the solution is

$$\dot{w}_n = (\Delta\nu_{j,n})^{-1}\,\dot{w}_j \tag{A.12}$$

where

$$(\Delta\nu_{j,n})^{-1} = \frac{(\Delta\nu_{n,j})}{|\Delta\nu_{j,n}|} \tag{A.13}$$

Since the reduced or globalized set is supposed to be equivalent to the original full set, we must prescribe that the net rates of production from the reduced set be equal to those of the full set for the species retained, i.e.,

$$\dot{w}_j = \dot{w}_i \qquad (j=i=1,\ldots,\hat{NS}) \tag{A.14}$$

and, similarly, that the concentrations be equal, i.e.,

$$C_j = C_i \qquad (j=i=1,\ldots,\hat{NS}) \tag{A.15}$$

Using these equivalency conditions, the left hand side of Eq. (A.8) is determined by Eq. (A.12), while the bracketed term on the right hand side of Eq. (A.8) is determined by the known concentrations from the full set calculations. Hence we can solve for the unknown rate constant $k_{f,n}$, i.e.,

$$k_{f,n} = \frac{\dot{w}_n}{\prod_j C_j^{\nu_{j,n}} - \frac{1}{K_{c,n}} \prod_j C_j^{\nu'_{j,n}}} \tag{A.16}$$

where, according to Eq. (A.15), the C_j are the concentrations as determined from the full set.

The procedure is completed by plotting and curve fitting the $k_{f,n}$ as a function of temperature. Other parameters such as fuel to oxidizer ratio may have to be incorporated to generalize the applicability of the rate constants thus derived.

Several problems can arise with the solution of the set of linear simultaneous equations represented by Eq. (A.11), depending on the number of species j, and the number of reactions n, comprising the "globalized" set. If $j > n$, obviously the set is over-determined, and we have a choice of species production rates to be used to determine the reaction rates w_j. If $j < n$, there are more unknowns than equations. The solution to this problem is to specify n-j rate constants, leaving j equivalent rate constants to be determined. Even if $j=n$, the coefficient matrix $(\nu_{j,n})$ is not necessarily nonsingular. The reason for this is as follows. If we consider j species composed of i elements, we can generally write i algebraic equations for elemental conservation. This means that j-i rate equations are sufficient to compute the species composition of the gas, that is, only j-i equations are linearly independent. Considering the present application this means that again in Eq. (A.11) $n < j$, which is the case discussed first.

The specific example of hydrogen-air combustion described in the next section will clarify the application of the methodology just described.

A.3 HYDROGEN-AIR COMBUSTION

The configuration chosen to test the general methodology was a relatively simple one, namely premixed, one-dimensional supersonic flow of a hydrogen-air mixture in a constant area channel. Detailed combustion calculations were performed using the ALFA code (Ref. A-1). Species considered consisted of N_2, O_2, H_2, H_2O, OH, O, H, H_2O_2 and HO_2. While N_2 was considered to be inert concentrations of the remaining species were calculated using a set of reactions for hydrogen-oxygen combustion adapted* from those given by Beach, Mackley, Rogers, and Chinitz (Ref. A-2). The full set as used is given in Table A-1.

On the basis of arguments presented by Rogers and Chinitz (Ref. A-3), the global model was selected to consist of two reactions, namely

$$H_2 + O_2 \overset{k_{f,1}}{\rightleftarrows} 2\ OH \tag{A.17}$$

$$2\ H_2O \overset{k_{f,2}}{\rightleftarrows} 2\ OH + H_2 \tag{A.18}$$

The second reaction actually being the reverse of the one given in Ref. A-3 so to conform to the reaction rate input format of the ALFA code (since the reactions can proceed either way, the form chosen is immaterial). Species involved in the global model thus consist of N_2, O_2, H_2, OH, and H_2O, i.e., five species as compared to nine in the full set, with a reduction in reactions from 18 to 2.

Application of the previously described methodology to determine the unknown rate constants $k_{f,1}$ and $k_{f,2}$ is straightforward.

From Eqs. (A.8) and (A.9) we find that

$$\dot{w}_1 = k_{f,1} \left(C_{H_2} C_{O_2} - \frac{1}{K_{c,1}} C_{OH}^2\right) \tag{A.19}$$

$$\dot{w}_2 = k_{f,2} \left(C_{H_2O}^2 - \frac{1}{K_{c,2}} C_{OH}^2 C_{H_2}\right) \tag{A.20}$$

---

*See Appendix B, Table B-1a and associated text for discussion.

Table A-1 - DETAILED HYDROGEN-AIR COMBUSTION KINETICS MECHANISM

	REACTIONS BEING CONSIDERED									KF=A*EXP(B/RT**M)/T**N			
										A*	N	B	M
1	H2	+	O2			=	OH	+	OH	1.024E+13	0.00	-43000.0	0.00
2	H	+	O2			=	OH	+	O	6.023E+10	-1.00	-14900.0	0.00
3	OH	+	H2			=	H2O	+	H	1.084E+09	-1.30	-3650.0	0.00
4	O	+	H2			=	OH	+	H	1.807E+10	-1.00	-8900.0	0.00
5	OH	+	OH			=	H2O	+	O	6.023E+07	-1.30	0.0	0.00
6	H	+	OH	+	M	=	H2O	+	M	2.213E+22	2.00	0.0	0.00
7	H	+	H	+	M	=	H2	+	M	6.530E+17	1.00	0.0	0.00
8	H	+	O2	+	M	=	HO2	+	M	2.104E+18	1.00	0.0	0.00
9	HO2	+	OH			=	H2O	+	O2	4.999E+13	0.00	-1000.0	0.00
10	HO2	+	H			=	H2	+	O2	2.530E+13	0.00	-700.0	0.00
11	HO2	+	H			=	OH	+	OH	1.988E+14	0.00	-1800.0	0.00
12	HO2	+	O			=	OH	+	O2	4.999E+13	0.00	-1000.0	0.00
13	HO2	+	HO2			=	H2O2	+	O2	1.988E+12	0.00	0.0	0.00
14	HO2	+	H2			=	H2O2	+	H	3.012E+11	0.00	-18700.0	0.00
15	H2O2	+	OH			=	HO2	+	H2O	1.024E+13	0.00	-1900.0	0.00
16	H2O2	+	H			=	OH	+	H2O	4.999E+14	0.00	-10000.0	0.00
17	H2O2	+	O			=	OH	+	HO2	1.988E+13	0.00	-5900.0	0.00
18	H2O2	+	M			=	OH	+	OH + M	1.205E+17	0.00	-45500.0	0.00

---

*Units: cm^3/mol-sec or cm^6/mol^2-sec.

and

$$\begin{aligned} \dot{w}_{O_2} &= -\dot{w}_1 \\ \dot{w}_{H_2} &= -\dot{w}_1 + \dot{w}_2 \\ \dot{w}_{H_2O} &= -2\,\dot{w}_2 \\ \dot{w}_{OH} &= 2\,\dot{w}_1 + 2\,\dot{w}_2 \end{aligned} \qquad (A.21)$$

Since the net production rates of O_2, H_2, H_2o and OH are known from the full set calculations, we can determine $\dot{w}_1$ and $\dot{w}_2$. As seen from Eq. (A.21) we have four equations for two unknowns, two of the equations providing our unknowns directly, i.e.,

$$\begin{aligned} \dot{w}_1 &= -\dot{w}_{O_2} \\ \dot{w}_2 &= -\frac{1}{2}\,\dot{w}_{H_2O} \end{aligned} \qquad (A.22)$$

Alternatively we can use the second and the fourth equation to obtain

$$\begin{aligned} \dot{w}_1 &= \frac{1}{4}\,\dot{w}_{OH} - \frac{1}{2}\,\dot{w}_{H_2} \\ \dot{w}_2 &= \frac{1}{4}\,\dot{w}_{OH} + \frac{1}{2}\,\dot{w}_{H_2} \end{aligned} \qquad (A.23)$$

Thus, from Eqs. (A.19), (A.20), and (A.23)

$$k_{f,1} = \frac{\frac{1}{4}\,\dot{w}_{OH} - \frac{1}{2}\,\dot{w}_{H_2}}{C_{H_2}\,C_{O_2} - \frac{1}{K_{c,1}}\,C_{OH}^2} \qquad (A.24)$$

$$k_{f,2} = \frac{\frac{1}{4}\dot{w}_{OH} + \frac{1}{2}\dot{w}_{H_2}}{C^2_{H_2O} - \frac{1}{K_{c,2}} C^2_{OH} C_{H_2}} \qquad (A.25)$$

where the right hand sides are completely determined from the full set calculations.

A.4 RESULTS

Results from the full set calculations are shown in Figs. A-1 and A-2. Initial conditions were T = 1000K, p = 760 torr, M = 2.24 and an equivalence ratio of $\phi = 0.25$ (initial calculations with higher equivalence ratios produced too large a heat release with choking of flow as a result). As seen from Fig. A-1, this case is characterized by a definite ignition delay ($0 < x \leq 22$ cm), before the temperature gradient shows any change (at constant velocity the distance of 22 cm corresponds to a delay time of 0.15 msec). The combustion front is centered around x = 29 cm, and combustion is basically complete at x = 40 cm.

Figure A-2 shows the species distributions through the combustion front. The two species not shown (H_2O_2 and HO_2) never reach relative concentrations of 10^{-4}. Note that in the evaluation of $k_{f,1}$ and $k_{f,2}$ (the global rate constants) we ignore the existence of the minor species H_2O_2 and HO_2, as well as O and H, including their transient peaks.

Global rate constants $k_{f,1}$ and $k_{f,2}$ were evaluated simultaneously with the results just shown. They are plotted in Figs. A-3 and A-4, respectively. Note that $k_{f,1}$ is plotted versus T = T-T (initial). From the results it can be seen that $k_{f,1}$ increases by almost three orders of magnitude while the temperature increases by only one degree during the ignition delay period. It was found impossible to fit this behavior with any of the standard rate constant formats ($k = A.T^N \exp(B/T)$). As shown in Fig. A-3, $k_{f,1}$, however, displays a reasonable behavior when plotted

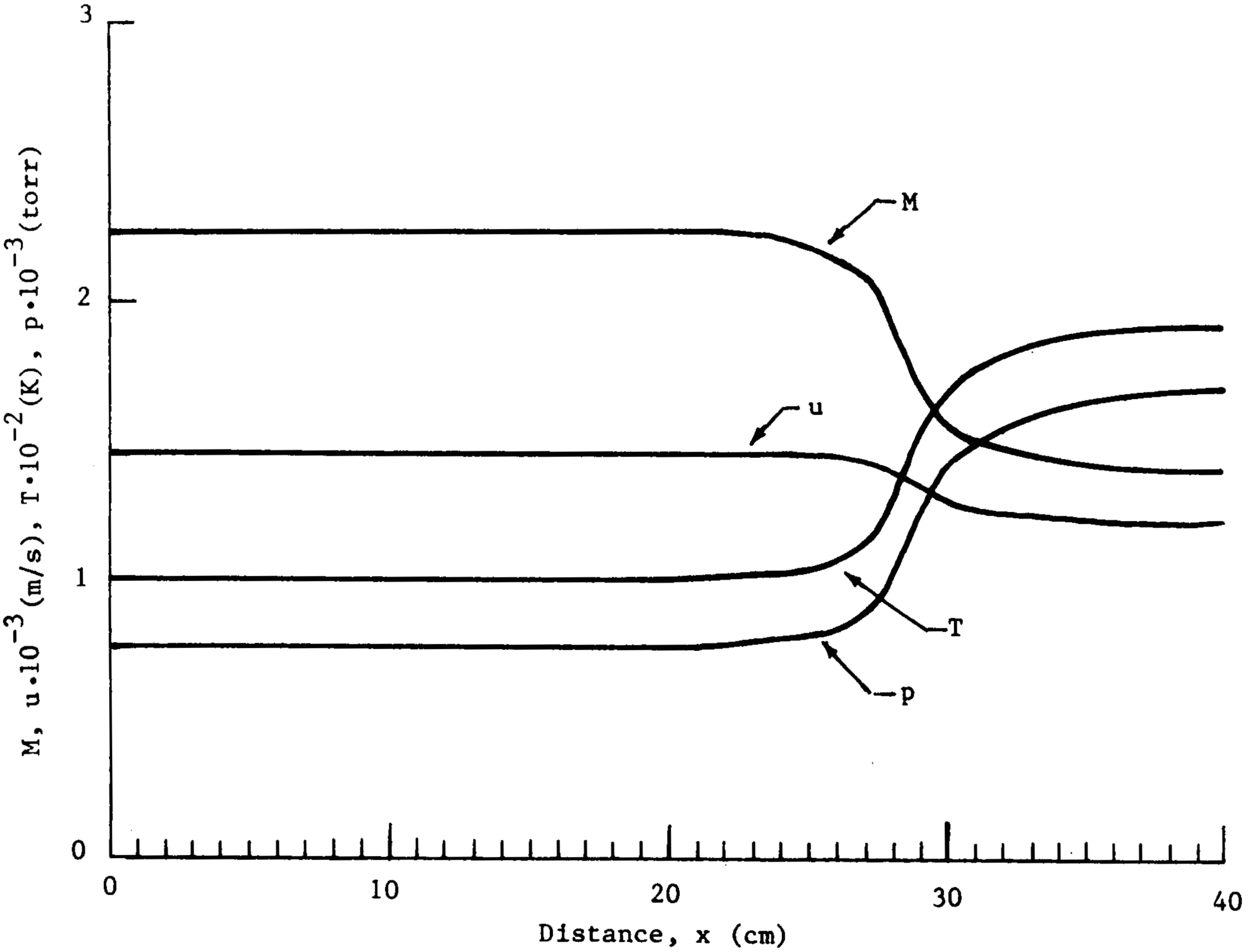

Fig. A-1 - Supersonic Channel Flow with H_2-Air Combustion ($\phi = 0.25$)

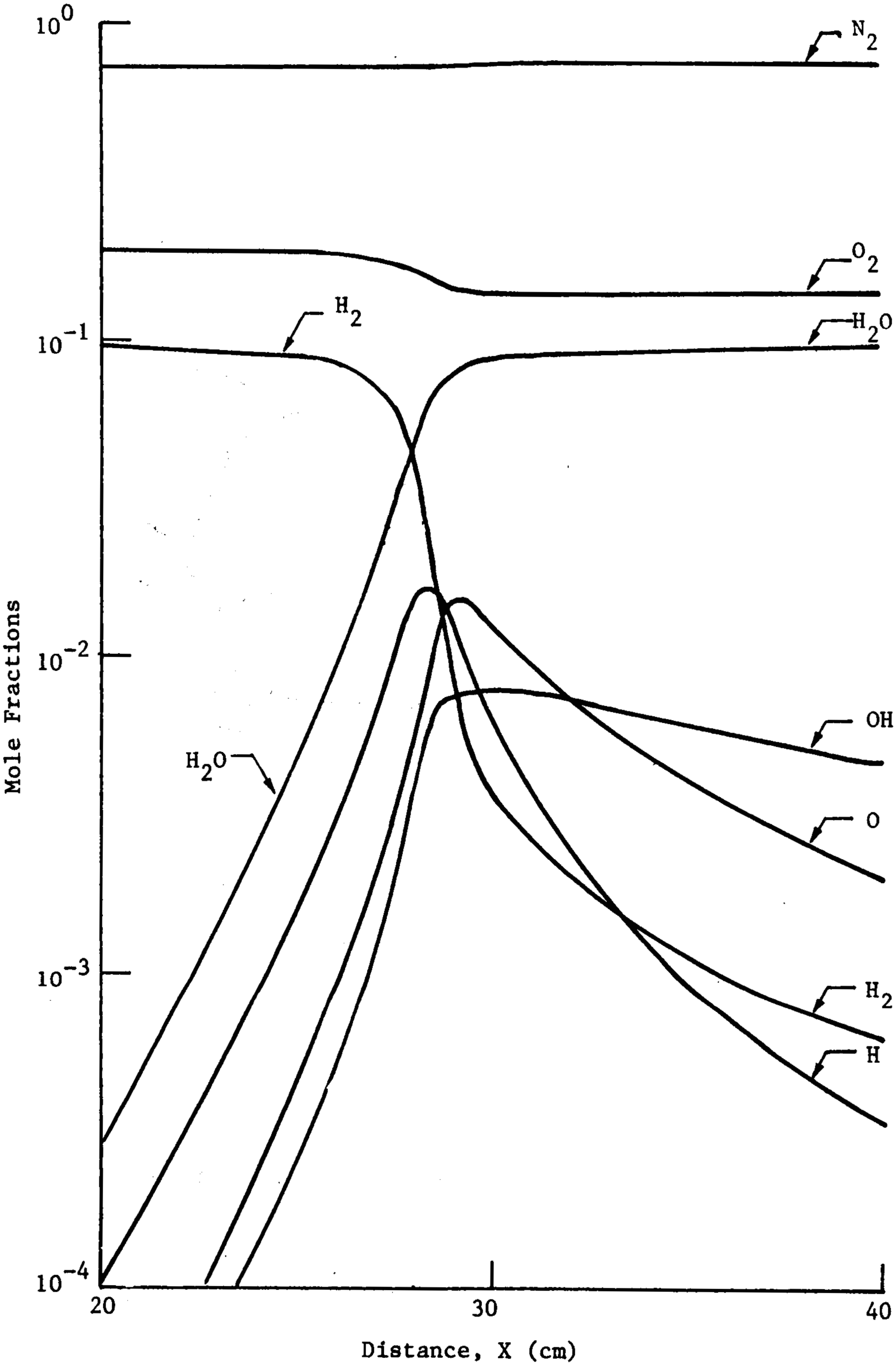

Fig. A-2 - Supersonic Channel Flow with H_2-Air Combustion (ϕ = 0.25)

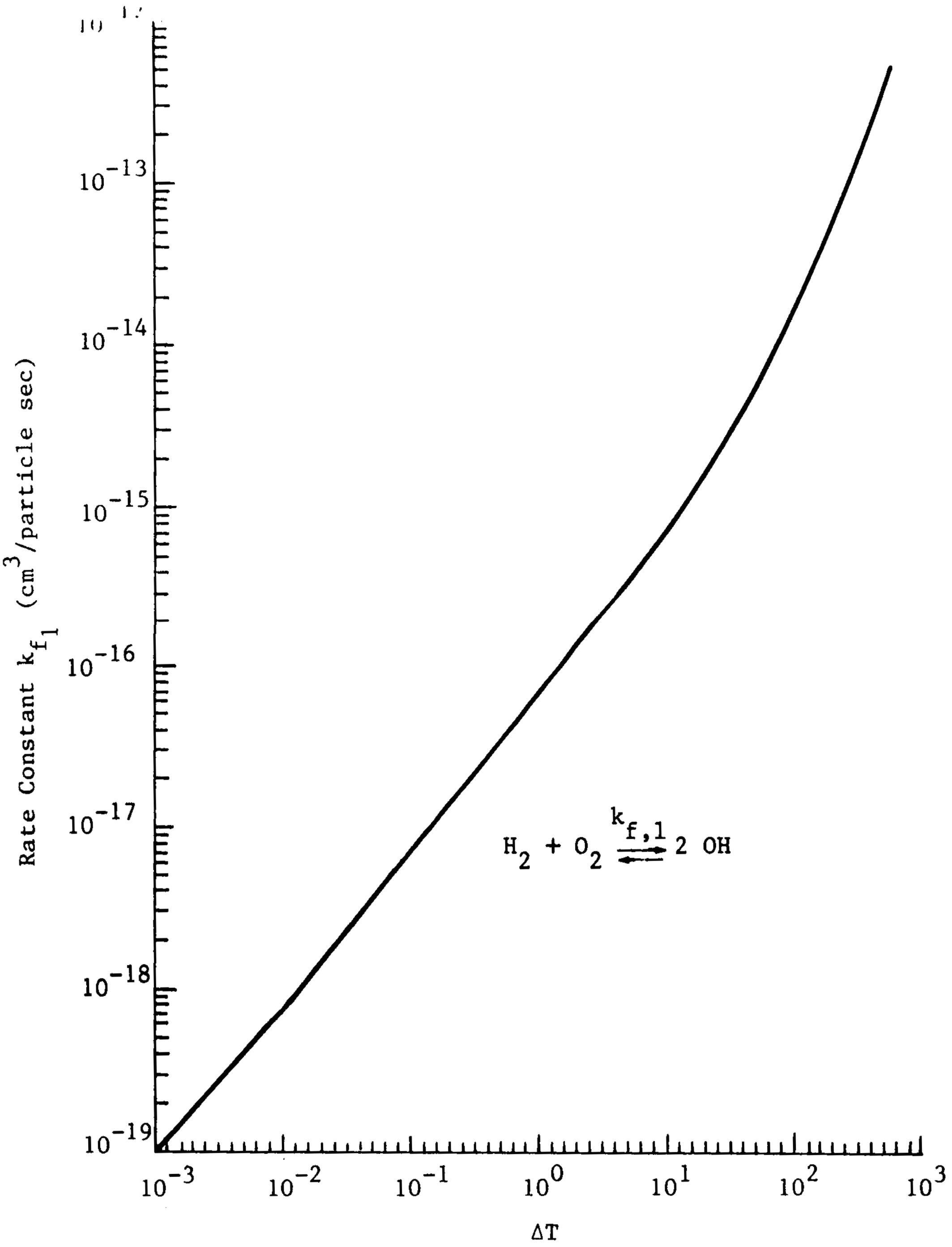

Fig. A-3 - Global Rate Constant $k_{f,1}$ as a Function of ΔT
(ΔT = T - 1000.0)

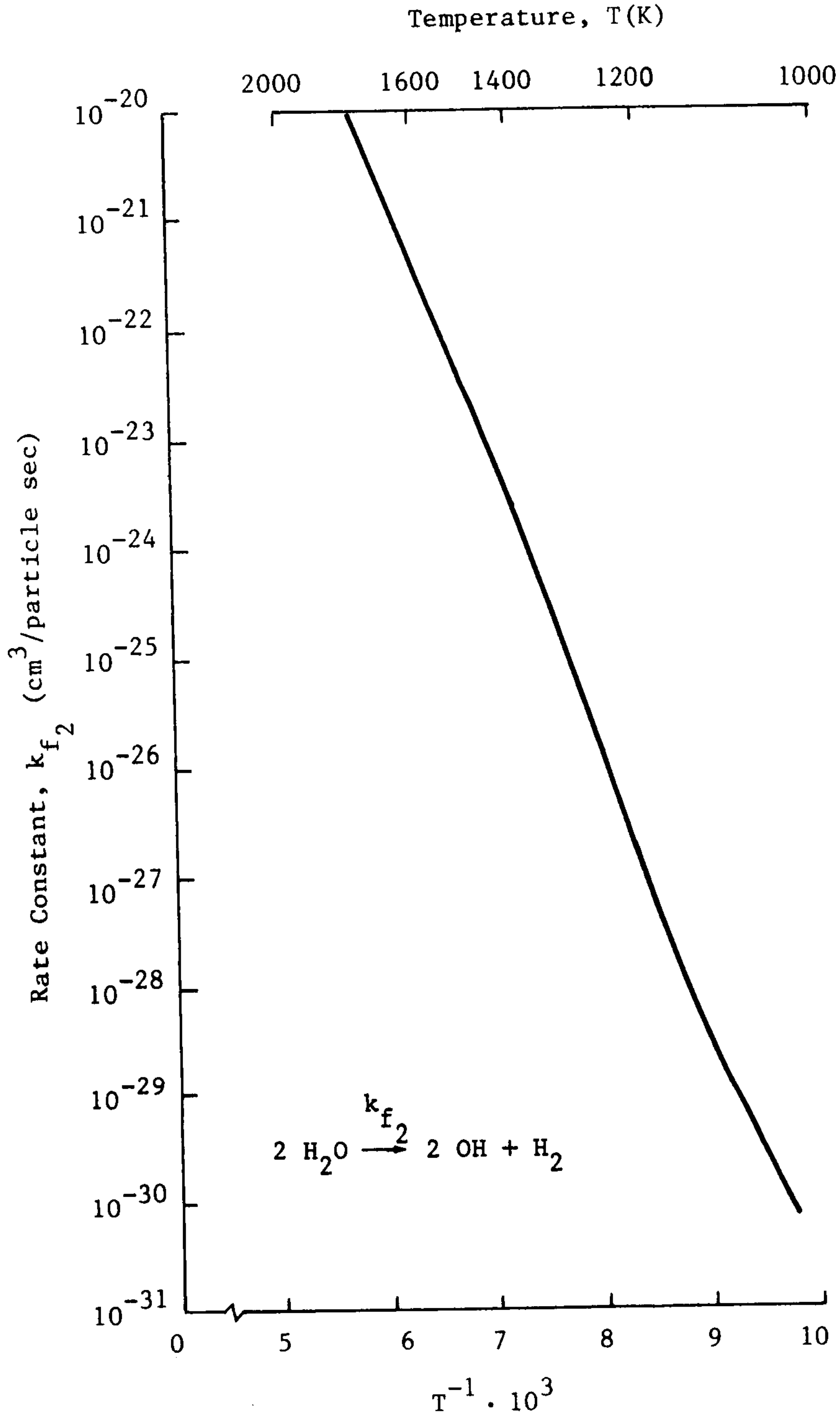

Fig. A-4 - Global Rate Constant k_{f_2} as Function of T^{-1}

versus ΔT. $k_{f,2}$, plotted versus inverse temperature, is shown in Fig. A-4. The almost perfect straight line immediately suggests a fit of the form k = A exp(-B/T). Trial curve fits and calculations with the global model revealed that excellent results can be obtained from the global model provided that the global rate constants are curve fitted accurately in the low temperature regime (i.e., for the conditions during the ignition delay period). A close fit for the high temperature region is much less important as in this region the rate of production is essentially determined by the concentrations of the reactants being depleted.

The final best curve fits obtained are (in cm^3/part sec)

$$k_{f,1} = 6.925 \,.\, 10^{-17} \Delta T^{0.979} \tag{A.26}$$

$$k_{f,2} = 3.80 \,.\, 10^{-6} \exp(-116{,}000/RT) \tag{A.27}$$

with emphasis on accuracy in the low temperature regime. The validity of these particular rate constants is, of course, at least at this time, restricted to the conditions used in these calculations.

Using the ALFA code, combustion calculations were then repeated using identical initial conditions but with the global model consisting of only five species (N_2,O_2, H_2, OH, and H_2O) and the two reactions (17, 18) with rate constants as given in Eqs. (A.26) and (A.27). The results are shown in Figs. A-5 and A-6 in comparison with the results from the detailed reaction model. As seen in Fig. A-5, results for the distribution of velocity, temperature and pressure are in excellent agreement with the detailed results, and the ignition delay is modeled exactly, for all practical purposes. Final temperature (and pressure) is slightly higher than that from the detailed model, a result expected based on the discussion given in Ref. A-3. Species concentration distribution through the combustion front can be compared in Fig. A-6. The agreement is very satisfactory.

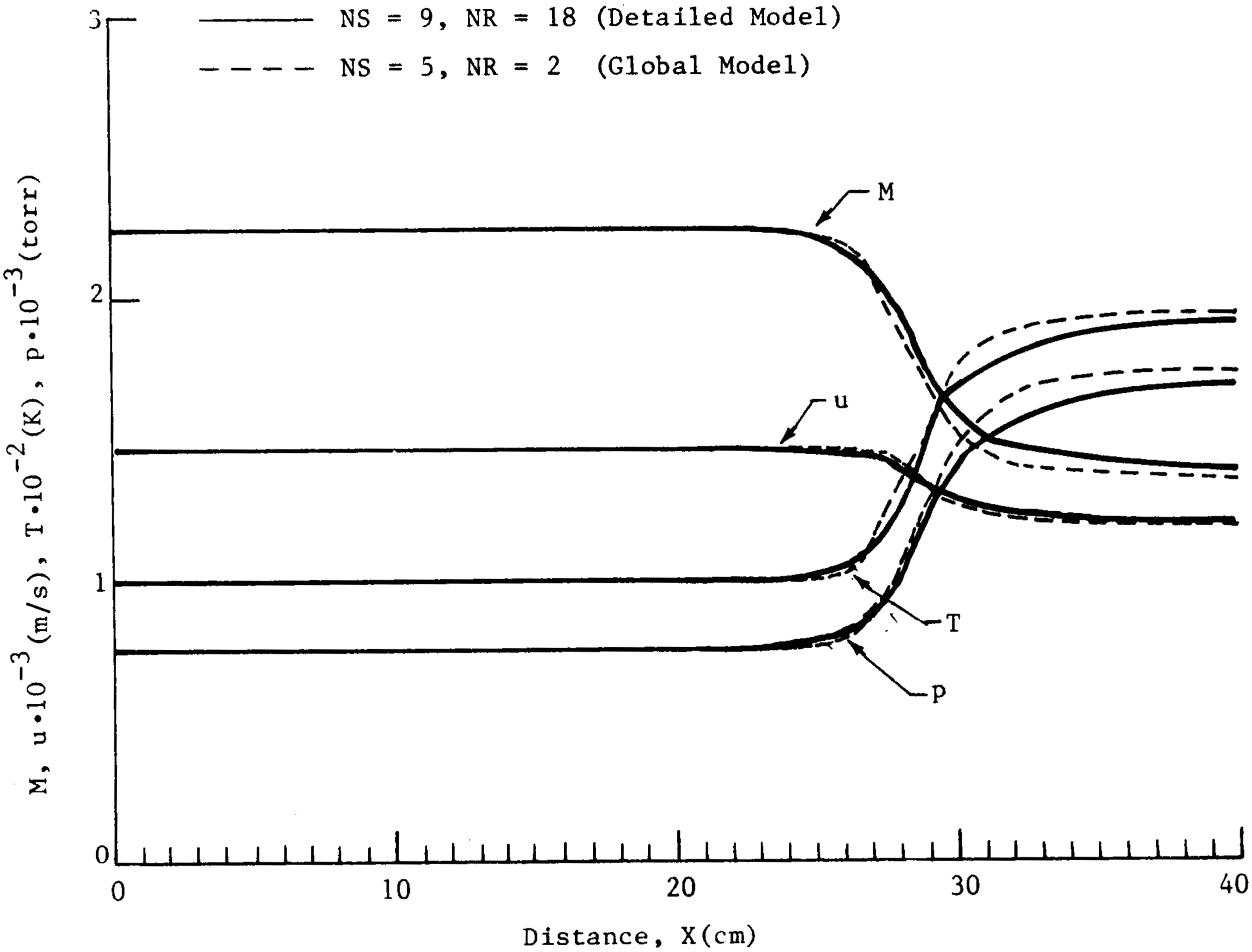

Fig. A-5 - Supersonic Channel Flow with H_2-Air Combustion ($\phi = 0.25$)

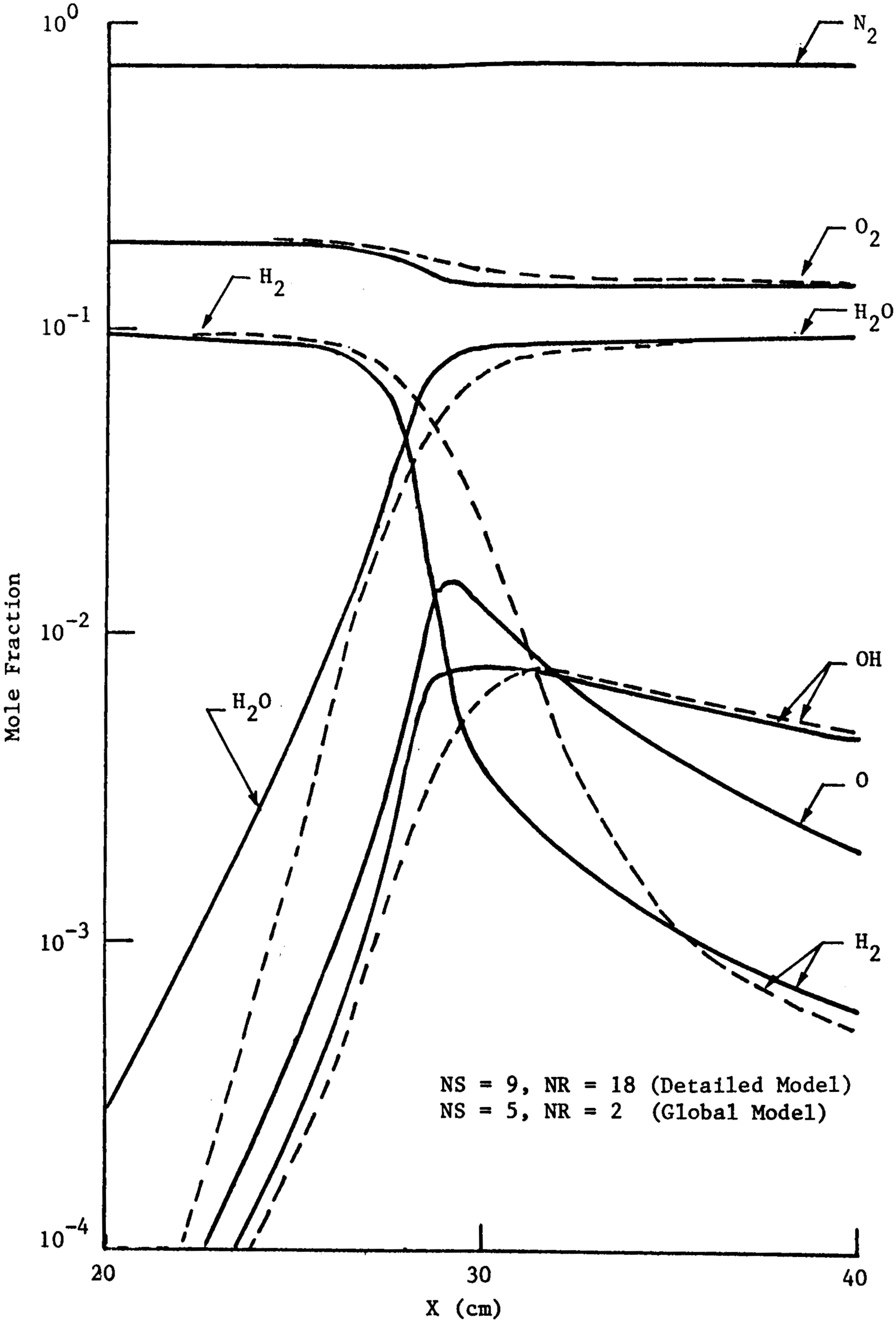

Fig. A-6 - Supersonic Channel Flow with H_2-Air Combustion (ϕ = 0.25)

A.5 CONCLUSIONS AND RECOMMENDATIONS

A general methodology has been presented to systematically reduce detailed reaction models, employing numerous species and reaction rates, to global systems with a minimum number of species and reaction mechanisms. Global rate constants can be evaluated directly thus avoiding possible tedious trial and error procedures.

The methodology was applied to the hydrogen-air combustion kinetics systems. Global rate constants were evaluated, curve fitted, and used to almost exactly reproduce the results obtained by using the detailed kinetics mechanism. The only real problem encountered was that of curve fitting one of the two global rate constants. It was found that, in order to model the ignition delay correctly, care must be taken to obtain an accurate representation of the global rate constants as a function of temperature in the ignition delay period.

The global rate constants which were evaluated are obviously valid for the sample case presented, but not for other conditions (temperature, equivalence ratio, pressure, etc.). Further calculations should be performed to establish global (or compound) rate constants of more general applicability.

REFERENCES

A-1. Thoenes, J., W.L. Hendricks, S.C. Kurzius, and F.C. Wang, "Advanced Laser Flow Analysis Theory and User's Guide," AFWL-TR-78-19, February 1979.

A-2. Beach, H.L., Jr., E.A. Mackley, R.C. Rogers, and W. Chinitz, "Use of Silane in Scramjet Research," 17th JANNAF Combustion Meeting, Volume I, Debra Sue Eggleston, ed., CPIA Publ. 329 (Contract N00024-78-C-5384), Appl. Phys. Lab., Johns Hopkins Univ., Nov. 1980, pp. 639-659.

A-3. Rogers, R.C., and W. Chinitz, "On the Use of a Global Hydrogen-Air Combustion Model in the Calculation of Turbulent Reacting Flows," AIAA Paper No. 82-0112, AIAA 20th Aerospace Sciences Meeting, 11-14 January 1981.

Appendix B

SUPERSONIC AIR-METHANE-SILANE/H_2 IGNITION[*]

---

[*] This work was performed in the period extending from 27 May 1981 to a cut-off date of 31 December 1981.

Appendix B

ABSTRACT

Detailed kinetics mechanisms for silane-hydrogen and methane oxidation have been combined and adapted for use in computation of the characteristics of supersonic air-methane-silane/H_2 ignition and heat release. After initial mechanistic refinement interfacing with the presently meager data (1981), predictions made with Lockheed's ALFA code using the refined mechanism as presently constituted - in a constant pressure, one-dimensional flow regime - are at least within a factor of 2 of early shock tube measurements of ignition delay at Langley Research Center over the range 800 to 1000K for silane-H_2-O_2/N_2 mixtures. Initial results of a parametric examination of theoretical ignition and reaction times in silane-CH_4-air mixtures have been obtained. Use of silane as an ignition aid materially reduces ignition delay and combustion times for methane in air.

INTRODUCTION

The inherent promise of silane as an ignition aid in testing hydrogen-fueled, airframe-integrated, supersonic combustion ramjet engines was first reported by Beach et al. in Ref. B-1. Initial experiments and analytical research at NASA-Langley relating to the use of silane in scramjet ground testing is presented by Beach et al. along with an early SiH_4/H_2 combustion mechanism formulated to permit kinetic computations of hydrogen-air flows employing silane ignition aid.

Use of hydrocarbons as fuel in potential scramjet applications is also of more than conceptual interest. As enumerated in the review of potential scramjet aircraft technology issues by Jones and Huber (Ref. B-2), hydrocarbons suffer by comparison to hydrogen as scramjet fuel due to their lower heats of combustion per unit mass and longer ignition delays. Other systems aspects arising from their intrinsically higher density and ease of handling and storage as liquids combine, however, to make the choice more competitive. Future systems development may very well hinge on the crucial issue of fuel choice between hydrogen and hydrocarbons such as methane, methanol or conventional JP-type aviation fuels. The outcome of such competition will clearly be effected by the utility of ignition aids such as silane in holding ignition and reaction times to manageable levels for these various fuels in flight regimes in which autoignition is not achievable.

The present study has been undertaken with the goal of extending the work of Ref. B-1 from the SiH_4/H_2 combustion system to the SiH_4CH_4 combustion system as a first step in the analytical exploration of the utility of silane as an ignition aid for testing hydrocarbon-fueled, airframe-integrated, supersonic combustion ramjet engines. Parametric computations were carried out to guide the experimental studies which seem likely to follow the favorable results of the present effort and initial, unpublished engine tests with hydrocarbons at GASL employing silane as ignition aid. During the course of the present study, results of initial shock tube measurements of ignition delays in SiH_4/O_2 mixtures diluted with 86 vol.% N_2 became available and it was possible to perform some mechanistic refinement based on these inputs, with the result that the SiH_4/H_2 mechanism of Ref. B-1 has also been substantially updated through necessity to improve agreement with these data.

REACTION MECHANISM

A workable methane/hydrogen-silane combustion mechanism has been formulated. As presently constituted it is as shown in Table B-1, consisting of (A) hydrogen; (B) methane; (C) silane; and (D) methane-silane interactive oxidation mechanisms, discussed in brief below. Lockheed's ALFA computer code (Ref. B-3) has been utilized in this study for all kinetics computations, in a constant pressure, premixed flow mode option. ALFA is a

Table B-1
REACTION MECHANISM

A. Hydrogen Oxidation Mechanism

Reaction (Reversible)	Rate Coefficient, cm^3 $particle^{-1}$-sec^{-1} units	Reference
1. $H_2 + O_2 \rightarrow OH + OH$	1.7×10^{-11} exp-43,000/RT	1, 7
2. $H + O_2 \rightarrow OH + O$	1.0×10^{-13} T exp-14,800/RT	8, Text
3. $OH + H_2 \rightarrow H_2O + H$	1.8×10^{-15} $T^{1.3}$ exp-3,650/RT	8
4. $O + H_2 \rightarrow OH + H$	3.0×10^{-14} T exp-8,900/RT	8
5. $OH + OH \rightarrow H_2O + O$	1.0×10^{-16} $T^{1.3}$	8
6. $H + OH + M \rightarrow H_2O + M$	6.1×10^{-26} T^{-2}	9
7. $H + H + M \rightarrow H_2 + M$	1.8×10^{-30} T^{-1}	1, 7
8. $H + O_2 + M \rightarrow HO_2 + M$	5.8×10^{-30} T^{-1}	1, 7
9. $HO_2 + OH \rightarrow H_2O + O_2$	8.3×10^{-11} exp-1,000/RT	1, 7
10. $HO_2 + H \rightarrow H_2 + O_2$	4.2×10^{-11} exp-700/RT	1, 7
11. $HO_2 + H \rightarrow OH + OH$	3.3×10^{-10} exp-1,800/RT	1, 7
12. $HO_2 + O \rightarrow OH + O_2$	8.3×10^{-11} exp-1,000/RT	1, 7
13. $HO_2 + HO_2 \rightarrow H_2O_2 + O_2$	3.3×10^{-12}	1, 7
14. $HO_2 + H_2 \rightarrow H_2O_2 + H$	5.0×10^{-13} exp-18,700/RT	1, 7
15. $H_2O_2 + OH \rightarrow HO_2 + H_2O$	1.7×10^{-11} exp-1,900/RT	10
16. $H_2O_2 + H \rightarrow OH + H_2O$	8.3×10^{-10} exp-10,000/RT	10
17. $H_2O_2 + O \rightarrow OH + HO_2$	3.3×10^{-11} exp-5,900/RT	10
18. $H_2O_2 + M \rightarrow OH + OH + M$	2.0×10^{-7} exp-45,500/RT	1, 7

Table B-1 (Continued)

B. Methane Oxidation Mechanism

Reaction (Reversible)	(To be used with H_2 Mechanism) Rate Coefficient, cm^3 $particle^{-1}$-sec^{-1} units	Reference
1. $CH_4 + M \rightarrow CH_3 + H + M$	$4.0 \times 10^{7}\ T^{-3.7}$ exp-103,200/RT	11, Text
2. $CH_4 + O_2 \rightarrow CH_2OH + OH$	1.0×10^{-12} exp-43,000/RT	12, Text
3. $CH_4 + OH \rightarrow CH_3 + H_2O$	$3.2 \times 10^{-18}\ T^{2.1}$ exp-2,450/RT	13
4. $CH_4 + H \rightarrow CH_3 + H_2$	$3.7 \times 10^{-20}\ T^{3}$ exp-8,700/RT	14, 15
5. $CH_4 + O \rightarrow CH_3 + OH$	$1.1 \times 10^{-18}\ T^{2.5}$ exp-7,400/RT	16, 17, Text
6. $CH_4 + HO_2 \rightarrow CH_3 + H_2O_2$	3.3×10^{-11} exp-18,000/RT	18
7. $CH_3 + O_2 \rightarrow CH_2OH + O$	1.2×10^{-11} exp-25,600/RT	19
8. $CH_3 + O_2 \rightarrow CH_2OH + O$	$2.0 \times 10^{-8}\ T^{-3}$ exp 1,000/RT	31, Text
9. $CH_3 + OH \rightarrow CH_2OH + H$	7.0×10^{-12}	19, 20
10. $CH_3 + O \rightarrow CH_2O + H$	1.4×10^{-10}	20, 21
11. $CH_3 + HO_2 \rightarrow CH_2OH + OH$	2.6×10^{-11}	18
12. $CH_3 + HO_2 \rightarrow CH_4 + O_2$	2.0×10^{-12} exp-400/RT	18
13. $CH_3 + CH_3 \rightarrow CH_4 + CH_2$	4.0×10^{-11} (Forward Only)	18, 29, Text
14. $CH_3 + CH_2O \rightarrow CH_4 + CHO$	$2.0 \times 10^{-14}\ T^{0.5}$ exp-600/RT	18
15. $CH_3 + CHO \rightarrow CH_4 + CO$	$5.0 \times 10^{-13}\ T^{0.5}$	18
16. $CH_2 + O_2 \rightarrow CO + H_2O$	4.0×10^{-11} exp-2,000/RT	30, Text
17. $CH_2OH + M \rightarrow CH_2O + H + M$	2.0×10^{-9} exp-29,000/RT	20
18. $CH_2OH + O_2 \rightarrow CH_2O + HO_2$	1.7×10^{-11}	20
19. $CH_2O + M \rightarrow CHO + H + M$	1.4×10^{-7} exp-81,000/RT	19
20. $CH_2O + OH \rightarrow CHO + H_2O$	$3.8 \times 10^{-15}\ T^{1.4}$	18, 22, Text
21. $CH_2O + H \rightarrow CHO + H_2$	$1.7 \times 10^{-12}\ T^{0.5}$ exp-3,300/RT	23, 33, Text

Table B-1 (Continued)

22. $CH_2O + O \rightarrow CHO + OH$	3.0×10^{-11} exp-3,100/RT	24
23. $CH_2O + HO_2 \rightarrow CHO + H_2O_2$	1.7×10^{-12} exp-7,900/RT	18, 20
24. $CHO + M \rightarrow CO + H + M$	4.0×10^{-9} exp-29,600/RT	19, 20
25. $CHO + O_2 \rightarrow CO + HO_2$	$3.0 \times 10^{-13}\ T^{0.5}$	20, 25, 26, Text
26. $CHO + OH \rightarrow CO + H_2O$	2.0×10^{-10}	18, 19
27. $CHO + H \rightarrow CO + H_2$	5.0×10^{-10}	25
28. $CHO + O \rightarrow CO + OH$	2.0×10^{-10}	27
29. $CHO + HO_2 \rightarrow CO + H_2O_2$	2.0×10^{-10} exp-3,000/RT	18
30. $CHO + CHO \rightarrow CH_2O + CO$	2.0×10^{-10} exp-700/RT	25, Text
31. $CO + O_2 \rightarrow CO_2 + O$	3.7×10^{-13} exp-60,000/RT	28
32. $CO + OH \rightarrow CO_2 + H$	1.1×10^{-13} exp(T/1100)	28
33. $CO + HO_2 \rightarrow CO_2 + OH$	2.2×10^{-10} exp-23,000/RT	28
34. $CO + O + M \rightarrow CO_2 + M$	4.0×10^{-33} exp-4,300/RT	9

C. Silane Oxidation Mechanism

(To be used with H_2 and CH_4 mechanisms)

Reaction (Reversible)	Rate Coefficient, cm^3-particle^{-1}-sec^{-1} unit	Reference
1. $SiH_4 + M \rightarrow SiH_2 + H_2 + M$	$2.5 \times 10^2\ T^{-2}$ exp-59,600/RT	37, 38, Text
2. $SiH_4 + O_2 \rightarrow SiH_2O + H + OH$	7.0×10^{-8} exp-34,000/RT	Text
3. $SiH_4 + OH \rightarrow SiH_3 + H_2O$	1.4×10^{-11} exp-100/RT	39
4. $SiH_4 + H \rightarrow SiH_3 + H_2$	2.4×10^{-11} exp-2,500/RT	40
5. $SiH_4 + O \rightarrow SiH_3 + OH$	7.0×10^{-12} exp-1,600/RT	39
6. $SiH_4 + HO_2 \rightarrow SiH_3 + H_2O_2$	1.0×10^{-11} exp-2,000/RT	Text

Table B-1 (Continued)

7.	$SiH_3 + O_2 \rightarrow SiH_2O + OH$	1.0×10^{-10} exp-9,700/RT	1, Text
8.	$SiH_3 + SiH_3 \rightarrow SiH_4 + SiH_2$	2.0×10^{-10}	Text
9.	$SiH_3 + OH \rightarrow SiH_2 + H_2O$	1.4×10^{-11}	Text
10.	$SiH_3 + H \rightarrow SiH_2 + H_2$	2.4×10^{-11} exp-1,100/RT	Text
11.	$SiH_3 + O \rightarrow SiH_2O + H$	1.4×10^{-10}	Text
12.	$SiH_3 + HO_2 \rightarrow SiH_4 + O_2$	2.0×10^{-12} exp-400/RT	Text
13.	$SiH_3 + SiH_2O \rightarrow SiH_4 + SiHO$	$2.0 \times 10^{-14}\ T^{0.5}$ exp-600/RT	Text
14.	$SiH_3 + SiHO \rightarrow SiH_4 + SiO$	$5.0 \times 10^{-13}\ T^{0.5}$	Text
15.	$SiH_2 + O_2 \rightarrow SiHO + OH$	4.0×10^{-11} exp-2,000/RT	Text
16.	$SiH_2O + OH \rightarrow SiHO + H_2O$	$4.0 \times 10^{-15}\ T^{1.4}$	Text
17.	$SiH_2O + H \rightarrow SiHO + H_2$	$2.0 \times 10^{-12}\ T^{0.5}$ exp-3,300/RT	Text
18.	$SiH_2O + O \rightarrow SiHO + OH$	3.0×10^{-11} exp-3,100/RT	Text
19.	$SiH_2O + HO_2 \rightarrow SiHO + H_2O_2$	2.0×10^{-12} exp-7,900/RT	Text
20.	$SiHO + M \rightarrow SiO + H + M$	1.0×10^{-9} exp-32,000/RT	Text
21.	$SiHO + O_2 \rightarrow SiO + HO_2$	$3.0 \times 10^{-13}\ T^{0.5}$	Text
22.	$SiHO + OH \rightarrow SiO + H_2O$	2.0×10^{-10}	Text
23.	$SiHO + H \rightarrow SiO + H_2$	5.0×10^{-10}	Text
24.	$SiHO + O \rightarrow SiO + OH$	2.0×10^{-10}	Text
25.	$SiHO + HO_2 \rightarrow SiO + H_2O_2$	2.0×10^{-10} exp-3,000/RT	Text
26.	$SiHO + SiHO \rightarrow SiH_2O + SiO$	2.0×10^{-10} exp-700/RT	Text
27.	$SiO + O_2 \rightarrow SiO_2 + O$	1.0×10^{-13} exp-10000/RT	Text
28.	$SiO + OH \rightarrow SiO_2 + H$	1.1×10^{-13} exp(T/1100)	Text
29.	$SiO + HO_2 \rightarrow SiO_2 + OH$	2.2×10^{-10} exp-23,000/RT	Text
30.	$SiO + O + M \rightarrow SiO_2 + M$	4.0×10^{-33} exp-4,300/RT	Text

Table B-1 (Concluded)

31. $SiO_2 + SiO_2 \rightarrow SiO_2X + SiO_2X$	$4.0 \times 10^{-8}\ T^{-2}$	Text
32. $SiH_2O + SiH_2O \rightarrow SiH_2OX + SiH_2OX$	$4.0 \times 10^{-8}\ T^{-2}$	Text

D. Methane-Silane Oxidation Mechanisms Interaction Reactions

Reaction (Reversible)	Rate Coefficient, cm^3-particle^{-1}-sec^{-1} units	Reference
1. $SiH_4 + CH_3 \rightarrow SiH_3 + CH_4$	1.3×10^{-12} exp-7,000/RT	40
2. $SiH_3 + CH_3 \rightarrow SiH_2 + CH_4$	1.0×10^{-12} exp-500/RT	Text
3. $SiH_3 + CHO \rightarrow SiH_2 + CH_2O$	$5.0 \times 10^{-13}\ T^{0.5}$	Text
4. $SiH_2O + CH_3 \rightarrow SiHO + CH_4$	$2.0 \times 10^{-14}\ T^{0.5}$ exp-600/RT	Text
5. $SiH_2O + CHO \rightarrow SiHO + CH_2O$	2.0×10^{-10} exp-700/RT	Text
6. $SiHO + CH_3 \rightarrow SiO + CH_4$	$5.0 \times 10^{-13}\ T^{0.5}$	Text
7. $SiHO + CHO \rightarrow SiO + CH_2O$	2.0×10^{-10} exp-700/RT	Text
8. $SiO + CHO \rightarrow SiHO + CO$	2.0×10^{-10} exp-700/RT	Text

Condensed Species: SiO_2X, SiH_2OX

M Body Catalytic Weighting Factors:

AR = 0.4, N_2 = 1.0, O_2 = 1.1, H_2 = 2.0, H_2O = 12.0

H_2O_2 = 16.0, CO = 1.0, CO_2 = 3.0, CH_4 = 1.5,
CH_2O = 6.0, CH_3OH = 9.0, SiH_4 = 2.5,
SiO = 16.0, SiO_2 = 16.0;
All Free Radicals = 16.0

two-dimensional code and can readily accommodate mixing between streamlines and/or accept prescribed area flow channels. It is anticipated that these options will be exercised in subsequent efforts.

Thermophysical input data were taken preferentially from the NBS JANAF Thermochemical Tables for species tabulated therein, or from the unpublished input data tapes supporting the computations of Ref. B-1, prepared by A.G. McLain of NASA-Langley Research Center for species (such as SiH_2O, SiHO) not included in the JANAF tables. Exceptions to this are the standard heat of formation of SiH_3 (46.6 kcal/mole), SiH_2 (57.9 kcal/mole) and SiH (90.2 kcal/mole) which were obtained from the recent work of Doncaster and Walsh (Ref. B-4). SiO_2X - silica solids - thermophysical properties utilized are those corresponding to JANAF's "high cristobalite." SiH_2OX is a solid postulated to account for evidence of hydrogen bonding and alternate solids forms observed by early investigators of silane oxidation (e.g., Emeleus and Steward, Ref. B-5), with thermophysical inputs which have been estimated based on those for SiO_2, SiO_2X and SiH_2O.

In view of: (1) the present rather large ignorance factor of the individual species M-body weighting factors for use particularly in the silane reactions, and (2) the need to reduce the reaction mechanism's complexity for computational economy, a simplified approach was taken in this study and a single set of generic M-body weighting factors was utilized. These are given in Table B-1, relative to N_2-which was assigned unit weight. They are derived from an interesting approximately linear correlation between log k and the boiling temperature of M, recently reviewed in the survey kinetics text by Kondratiev and Nikitin (Ref. B-6, p. 110). Here an upper asymptotic limit of 16 has been inferred from the scant data base. In any event, with N_2 the main constituent in the flows of interest, with rates entered for N_2, results should not be overly sensitive to a reasonably judicious choice of generic M-body weighting factors, while the resulting simplification in the computations is appreciable.

A. Hydrogen Oxidation Mechanism

For the most part, the hydrogen mechanism is that used in Ref. B-1, taken from Slack and Grillo (Ref. B-7), minus NO_x reactions. Rate coefficient expressions for reactions 2 through 5 are, however, from the recent critical review by Cohen and Westberg (Ref. B-8)*; similarly, the rate coefficient for reaction 6 is from the recent NBS data compilation by Hampson (Ref. B-9). Additionally, reactions 15 through 17 have been added to the mechanism based on the finding of the sensitivity study by Dougherty and Rabitz (Ref. B-10) that they are required; rate coefficients for these reactions are those recommended by these authors. Similarly, the O+O+M reaction has been deleted from the mechanism, again on the basis of the sensitivity study by Dougherty and Rabitz.

B. Methane Oxidation Mechanism

As is evident from the references cited in Table B-1b, several methane kinetics sources were utilized, preferentially those from critical reviews by Westbrook and Dryer (Ref. B-18), Gardiner and Olson (Ref. B-19), and Tsuboi and Hashimoto (Ref. B-20). The methane mechanism is however less well settled than that for hydrogen and major discrepancies still exist between the assessments of the various authors. It was consequently found necessary to judiciously attempt to resolve some of these discrepancies and also to provide some additional data updates. These only will be briefly discussed below.

---

*The pre-exponential factor for reaction 2 has been modified (well within the uncertainty bound cited by Cohen and Westberg) from 7.5×10^{-14} to 1.0×10^{-13} cm^3- $particle^{-1}$-sec^{-1}, for purposes of obtaining closer correspondence between the computations made with the mechanism of Ref. B-1 and this work. (At 1000K, the ratio of rates for this important reaction is 0.75 for the present set of rates versus that of Ref. B-1; forcing closer agreement would be less consistent with the error bounds cited by Cohen and Westberg in Ref. B-8.

Reaction 1. Tabayashi and Bauer's (Ref. B-11) result for M-body dissociation of methane by Argon has been converted to the corresponding value with N_2 as the M-body, utilizing the generic M-body weighting factors employed in this study. Agreement with Westbrook and Dryer's (Ref. B-18) expression at 2000K is excellent. This modification has been made also for other reactions involving M bodies, where appropriate.

Reaction 2. The rate coefficient for the $CH_4 + O_2$ reaction is poorly known. Huffington et al. (Ref. B-12) cite the "general belief" that O_2 attack is dominant below 2000K. Here, the pre-exponential factor has been estimated at one-twentieth that of the corresponding H_2+O_2 reaction and the activation energy has been set equal to that for the H_2+O_2 reaction. The resulting rate coefficient is about one-half that of the $CH_4 + M$ rate (i.e., Reaction 1) at 2000K and rapidly dominates it at lower temperatures due to the appreciably lower activation energy. A posteriori, the reasonableness of the results obtained in this study suggest that the present estimate is acceptable in the absence of definitive data.

Reaction 5. The rate expression developed by Roth and Just (Ref. B-16) has been modified by this author to better accommodate the prior data and the more recent higher temperature data of Felder and Fontijn (Ref. B-17).

Reaction 8. As observed in the review by Gardiner and Olson (Ref. B-19) there is considerable uncertainty in the temperature behavior of the rate of the $CH_3 + O_2$ branching reactions, particularly at lower temperatures. Here, the approach has been taken to use the rate coefficient for Reaction 7 to represent the high temperature branch of the $CH_3 + O_2$ reaction and to develop the rate coefficient for the low temperature branch of the identical reaction as Reaction 8, using the temperature dependence suggested by Bhaskaran et al. (Ref. B-31), fitting the pre-exponential factor to extensive classical ignition delay data correlated by Asaba et al. (Ref. B-32). We performed iterative calculations of ignition delay defined as the time required to reach 5 percent of the final equilibrium temperature rise at constant pressure, as in Ref. B-1. It was found that the resulting delay times were almost inversely proportional to the sum of the rates for Reactions 7 and 8, with Reaction 8 dominating at low temperature as expected. Excellent agreement was obtained between the shock tube ignition delay times and the delay times so calculated, using the entire methane (and hydrogen) reaction mechanism as given in Table B-1, at 1 atm and initial temperatures varying from 700 to 1500K. However, a more proper computation for comparison to shock tube data would utilize a constant density (rather than pressure) post-shock condition. To do this with the ALFA code, a few code revisions need to be made which unfortunately have not yet been made. We hope to do this in the near future in an extension of this effort and repeat the aforementioned iterative computations to further refine the mechanism. For this reason, these computed results will not be presented here. It is important to note however that the changes resulting from the computational refinements are not anticipated to be more than by a factor of 2 at most, based on prior experience and other data analysis. Thus while the changes are thought to be important and necessary for proper kinetic interpretation of shock tube data, they are not of overriding importance and do not negate the basic goodness-of-fit of results obtained with the present analysis.

Reaction 9. Tsuboi and Hashimoto's (Ref. B-20) rate coefficient for the CH_3 + OH reaction has been employed, with the reaction written to yield CH_2OH + H, as favored by Gardiner and Olson (Ref. B-19).

Reaction 10. Washida's (Ref. B-21) room temperature result for this reaction has been used, with the zero activation energy indicated by Tsuboi and Hashimoto (Ref. B-20).

Reaction 13. The radical sink reaction between CH_3 + CH_3 is known to be important in the methane mechanism (see, e.g., Ref. B-18). The major product is actually thought to be C_2H_6, rather than CH_4 + CH_2 as written in Table B-1 to avoid complexities arising from the introduction of

C_2 hydrocarbons into the mechanism. For this reason we allow this globalized reaction only to proceed in the forward direction in the computations, using the rate coefficient measured by Baulch and Duxbury (Ref. B-29) and thus dodging unnecessary complexities in the mechanism.

Reaction 16. The room temperature result of Laufer (Ref. B-30) has been used for the $CH_2 + O_2$ reaction together with an estimated activation energy of 2 kcal/mole. To eliminate spurious chain branching from the effective radical sink reaction $CH_3 + CH_3$, here written as leading to $CH_4 + CH_2$, the products of the $CH_2 + O_2$ reaction have been written as $CO + H_2O$, rather than $CHO + OH$. Thus the combined result of Reactions 13 and 16 is, effectively, $CH_3 + CH_3 + O_2 \rightarrow CH_4 + CO + H_2O$, i.e., a chain termination step.

Reaction 20. Low temperature recent results by Stief et al. (Ref. B-22) have been pooled with higher temperature results cited by Westbrook and Dryer (Ref. B-18) to obtain the rate coefficient expression used in this study.

Reaction 21. Klemm's (Ref. B-23) low temperature expression for the rate coefficient of the $CH_2O + H$ reaction has been here rewritten to obtain agreement with higher temperature results of Dean, Johnson and Steiner (Ref. B-33).

Reaction 25. The rate coefficient given in Table B-1 for the $CHO + O_2$ reaction is the result of reconciliation by the author of low temperature data by Reilly et al. (Ref. B-25) and Shibuya et al. (Ref. B-26) with the high temperature result of Tsuboi and Hashimoto (Ref. B-20).

Reaction 30. The rate coefficient given in Table B-1 for the $CHO + CHO$ reaction is the result of assigning a pre-exponential factor equal to that for the reaction of CHO with O, OH and HO_2 (Reactions 26, 27, and 28) and equating an Arrhenius rate coefficient format to the room temperature result of Reilly et al. (Ref. B-25), thereby obtaining a quite reasonably activation energy of 700 cal/mole.

C. Silane Oxidation Mechanism

Beyond the most elementary reactions of SiH_4 itself with M (thermal dissociation), OH, H and O, virtually none of the detailed steps of the silane combustion mechanism have been firmly established, much less studied to the point where measurements of individual rate coefficients are available. Consequently this mechanism is largely in an exploratory status. The present formulation has utilized the early mechanism derived by Beach, Mackley, Rogers and Chinitz (Ref. B-1) as a starting point, with the advantage of the first experimental shock tube measurements of silane-hydrogen-oxygen-nitrogen delay times, by McLain (Ref. B-34). Only a very brief discussion of the basis of the mechanism is permitted here.

Reaction 1. In Ref. B-1 the products of the thermal dissociation reaction SiH_4 + M were written as SiH_3 + H, based largely on an analysis of the results of Strater (Ref. B-35). Strater's work however was performed in a reactor packed with silica chips and it seems likely that the results therein were largely dominated by heterogeneous processes. This conclusion is strongly reinforced by the demonstration by Baliga and Ghandi (Ref. B-36) that silane decomposition rates under conditions similar to Strater's are strongly dependent on substrate temperature and obey the rate theory of heterogeneous reactions at a solid surface. Moreover, the existing homogeneous phase thermal decomposition data of Newman et al. (Ref. B-37) and also of Purnell and Walsh (Ref. B-38) is quite convincing in the finding that H_2 rather than H is the hydrogenic species resulting from the primary thermal dissociation step. For these reasons this author has felt compelled to accept the results of Refs. 37 and 38, writing the thermal decomposition step as $SiH_4 + M \rightarrow SiH_2 + H_2 + M$. This of necessity required additional extensive revision to the mechanism of Ref. B-1 as discussed below.

Reaction 2. Silane is well-known to react spontaneously - and also somewhat erratically - with oxygen at temperatures near ambient over a wide range of equivalence ratios. This can only be possible - regardless of an apparent role of impurities of either gas phase or heterogeneous origin as chain starters - if a direct reaction between O_2 and SiH_4, as postulated in Table B-1, occurs. The rate coefficient listed is the result of fitting early ALFA computations of ignition delay times - defined as discussed in B above - to the recent shock tube measurements of ignition delay of McLain (Ref. B-34). Better agreement with the shock tube data and some minor revision of the rate coefficient is anticipated when ALFA can model a constant density flow regime to more accurately describe conditions behind the reflected shock used in NASA's ignition experiments.

Reactions 3, 4, and 5. The rate coefficients for the elementary reactions of silane with OH, H and O are those recommended in the study and review of Atkinson and Pitts (Ref. B-39) and Arthur and Bell (Ref. B-40), respectively.

Rate coefficients for the remaining reactions are all estimates, some of which have had the benefit of refinement possible because of the availability of McLain's recent data (Ref. B-34).

Reaction 6. The Arrhenius parameters for the $SiH_4 + HO_2$ abstraction reaction have been estimated from those for the corresponding reaction of silane with OH, H, and O (i.e., Reactions 3, 4, and 5).

Reaction 7. The rate coefficient for the $SiH_3 + O_2$ reaction, written as in Ref. B-1, is that estimated by Chinitz (Ref. B-1), with the activation energy modified to 9700 cal/mole based on observation by Vasilyeva et al. (Ref. B-41) of this activation energy for the upper ignition limit ratio of silane to O_2 at atmospheric pressure. This assignment must of course be regarded as tentative until such time as a deeper analysis of the available silane explosion limit data is attempted. Such analysis unfortunately was beyond the scope of this limited study.

Reaction 8. Heavy reliance has been placed on the logic employed in developing the methane mechanisms discussed above to write the products of the radical sink SiH_3 + SiH_3 reaction as SiH_4 + SiH_2, with a temperature-independent rate coefficient, quite in analogy to the CH_3 + CH_3 radical sink reaction. The rate coefficient has been increased to 2.0 x 10^{-10} from the 4.0 x 10^{-11} of the CH_3 + CH_3 reaction partly on an intuitive basis and partly as a result of mechanistic refinement required to better match the McLain data.

Reactions 9 and 10. The rate coefficients for the SiH_3 + OH and SiH_3 + H abstraction reactions have been estimated as follows: Preexponential factors equal to those for the corresponding SiH_4 reactions have been assigned; the activation energy for the OH reaction is estimated to be less than that for the OH reaction wih SiH_4, i.e., essentially zero; the activation energy for the H atom reaction has been estimated at 1100 cal/mole based on the corresponding rate coefficient for the H abstraction reaction with disilane reported by Arthur and Bell (Ref. B-40) and the conviction that the SiH_3 rate is appreciably faster than the SiH_4 rate.

Raction 11. The SiH_3 + O reaction has been written as the complete analogue of the CH_3 + O reaction, with identical rate coefficient, in the absence of any other input.

Raction 12. Similarly, the $SiH_3 + HO_2 \rightarrow SiH_4 + O_2$ reaction has been written as the silane analogue of the corresponding $CH_3 + HO_2 \rightarrow CH_4 + O_2$ reaction, with identical rate coefficient. Note that the analogue of the $CH_3 + HO_2 \rightarrow CH_2OH + OH$ reaction has been omitted from the mechanism to avoid having to treat the largely unknown SiH_2OH species.

Reaction 13. Again, the $CH_3 + CH_2O \rightarrow CH_4 + CHO$ reaction has served as the postulated analogue for the postulated $SiH_3 + SiH_2O \rightarrow SiH_4 + SiHO$ reaction, with identical rate coefficient.

Reaction 14. Here the analogue has been the $CH_3 + CHO \rightarrow CH_4 + CO$ reaction, with presumed essentially equal rate coefficient for the postulated $SiH_3 + SiHO \rightarrow SiH_4 + SiO$ reaction.

Reaction 15. Again, the logic employed in the methane system for the $CH_2 + O_2$ reaction has been invoked for the $SiH_2 + O_2$ analogue, with an equal rate coefficient assigned. Note that as in the methane mechanism, the only SiH_2 reaction entered is the dominant one with O_2.

Reactions 16 through 30. With one exception all of these postulated reactions have been written as proceeding just as their analogues in the methane mechanism, with essentially equal or slightly faster rate coefficients. The exception is the $SiO + O_2 \rightarrow SiO_2 + O$ reaction which has been written with a rate coefficient which has relatively little impact on ignition delay times at higher temperatures but without which no ignition can occur at temperatures near ambient even with quite appreciable sensitization by trace species. With the mechanism as written, auto-ignition of silane-air mixtures at temperatures near ambient has been tentatively identified as being due to sensitization by such trace species, as from contaminants and/or the products of heterogeneous reactions. For example, ozone in amounts often present at sea level (i.e., 1 to 10 parts per billion) is predicted to induce ignition of stoichiometric silane-air mixtures at 1 atm and 300 K in from 2 to 7 sec with the mechanism as given in Table B-1. With no ozone or similarly reactive free radical-generating agent - or without Reaction 30 - no perceptible reaction occurs.

Reactions 31 and 32. Condensation of solids results in appreciable (i.e., several hundreds of degrees Kelvin) temperature rise in silane combustion, the magnitude of course depending on the concentration of silane. Inasmuch as such large temperature changes drastically alter rates for individual reactions - especially those with high activation energy - accurate kinetic modeling of silane ignition requires inclusion of solids nucleation. Here, a very simple, expedient approach to modeling solids condensation kinetics has been taken: Rather than becoming embroiled in the exact details of the very complex nucleation processes - largely unknown for silaceous species at this time in any event - a simple ternary condensation process, e.g., $SiO_2 + SiO_2 + M \rightarrow SiO_2X + SiO_2X + M$ was invoked, with a rather ordinary ternary rate coefficient of about $6 \times 10^{-30}\ T^{-1}$. Further, since the ALFA code cannot handle such a reaction type (without special modification which seemed unwarranted) the reaction was rewritten as a simple binary rate process with rate coefficient k x [M], i.e., with [M] evaluated at atmospheric pressure, the rate process is, e.g., $SiO_2 + SiO_2 \rightarrow SiO_2X + SiO_2X$ with a rate coefficient approximated by $4.0 \times 10^{-8}\ T^{-2}$, quite adequate for the relatively small pressure excursion range 0.5 to 2.0 atm contemplated for application of the mechanism developed for this study.

D. Methane-Silane Oxidation Mechanisms Interaction Reactions

This subset extends the silane mechanism developed above for use with the hydrogen and methane mechanisms simultaneously, as required for modeling silane-assisted ignition of methane. Note that the reactions have all been written in the exothermic direction.

Reaction 1. Arthur and Bell (Ref. B-40) reviewed results for the $SiH_4 + CH_3 \rightarrow SiH_3 + CH_4$ reaction, and their recommended value has been utilized in the mechanism developed.

Reaction 2. The rate coefficient for the presumed $CH_3 + SiH_3 \rightarrow CH_4 + SiH_2$ reaction has been estimated from the not disparate values for the $CH_3 + CH_2O \rightarrow CH_4 + CHO$ and $CH_3 + HO_2 \rightarrow CH_4 + O_2$ reactions, in the absence of any other input data.

Reactions 3, 4, 6, and 7. These processes have been written exothermically, with rate coefficients equal to the equivalent encounters in the methane system, i.e., the CH_3 + CHO encounter for SiH_3 + CHO and the $CH_2O + CH_3$ encounter for $SiH_2O + CH_3$, etc.

Reactions 5 and 8. The SiH_2O + CHO and SiO + CHO processes have also been written exothermically, each with rate coefficients equal to that for the CHO + CHO encounter, in the absence of any other input data.

E. Status of Mechanism

In synopsis, it is clear that where experimental inputs have not been available, very heavy use of insights and data inputs developed for the methane combustion mechanism have been imbedded in this work into the development of the silane combustion mechanism, much as was the principle of the approach taken by Chinitz (Ref. B-1) in developing the earlier silane mechanism. Here the methodology has been carried one step further, giving the present mechanism benefit of a large body of literature pertaining to methane combustion where required to close gaps in the relatively meager silane data base. The extent to which this adaptation of the methane formalism accurately describes silane results is still a moot point. As the silane data base expands additional mechanistic refinement can surely be anticipated.

Particular kinetic issues of concern at the moment include: (1) the need for independent experimental confirmation of such key rates as that postulated between silane and O_2 (i.e., Reaction 2, Table B-1c); (2) the need for a detailed exploration of the sensitivities of predicted combustor heat release profiles to variations in uncertain rate coefficients and minor reaction pathways, leading to greater understanding of the $SiH_4/H_2/CH_4$ system and, also, to a mechanism reduced to its essentials; (3) the extent of reaction, if any, between SiO and the species H_2O and CO_2. As presently constituted (with the SiO + OH reaction the primary step leading to SiO_2) in fuel-rich regimes with excess H_2 in the flow, the present mechanism leads to an undershoot in flame temperature potentially of several hundred degrees Kelvin, depending on mixture composition. This has been traced to incomplete (i.e., nonequilibrium) combustion of SiH_4 to SiO due to removal of uncombined O_2 by rapid combustion of H_2 in excess, effectively stopping the SiO oxidation chain. Is this a true nonequilibrium, cool flame phenomenon? Does SiO react with H_2O, or CO_2, to form SiO_2? Russian work indicates this possibility - as well as the possibility that perhaps a solid SiO phase needs to be considered: "Solid SiO reacts slowly with atmospheric O_2 at room temperature. Complete oxidation is not achieved at 500 C. It is pyrophoric in a finely divided state and burns to SiO_2 in air, producing a flame. Water vapor reacts noticeably with SiO even at 500 C, producing SiO_2 and H_2. Silicon monoxide is slowly oxidized in a CO_2 atmosphere at 400 C..." (Berezhnoi, (Ref. B-42, p. 102), and; (4) finally, definitive determination of the identity and concentration history of reaction intermediates and end-products - gaseous and solid - is required to assure the understanding of silane combustion chemical physics.

RESULTS

Digests of results computed in this study have been forwarded under separate cover at periodic intervals to Dr. R.C. Rogers, Hypersonic Propulsion Branch, Langley Research Center. A detailed summary of these extensive results is not presented in the present report due to time and space limitations. We will however summarize the high points and principal results of our effort.

A. Silane-Hydrogen Combustion

Figure B-1 shows results obtained for the recent shock tube experiments of McLain (Ref. B-34). The uppermost curve shows results computed by McLain usin the reaction mechanism of Ref. B-1, employing the NASA code described in Ref. B-43 run in a constant density flow option. $\tau_{Ignition}$ is the ignition delay time based on extrapolation of a T versus time arithmetic coordinate plot at its steepest slope back to the temperature of the initial post-shock gas mixture. Also shown on the figure is McLain's experimental data and the computed results obtaind in the present study with the mechanism

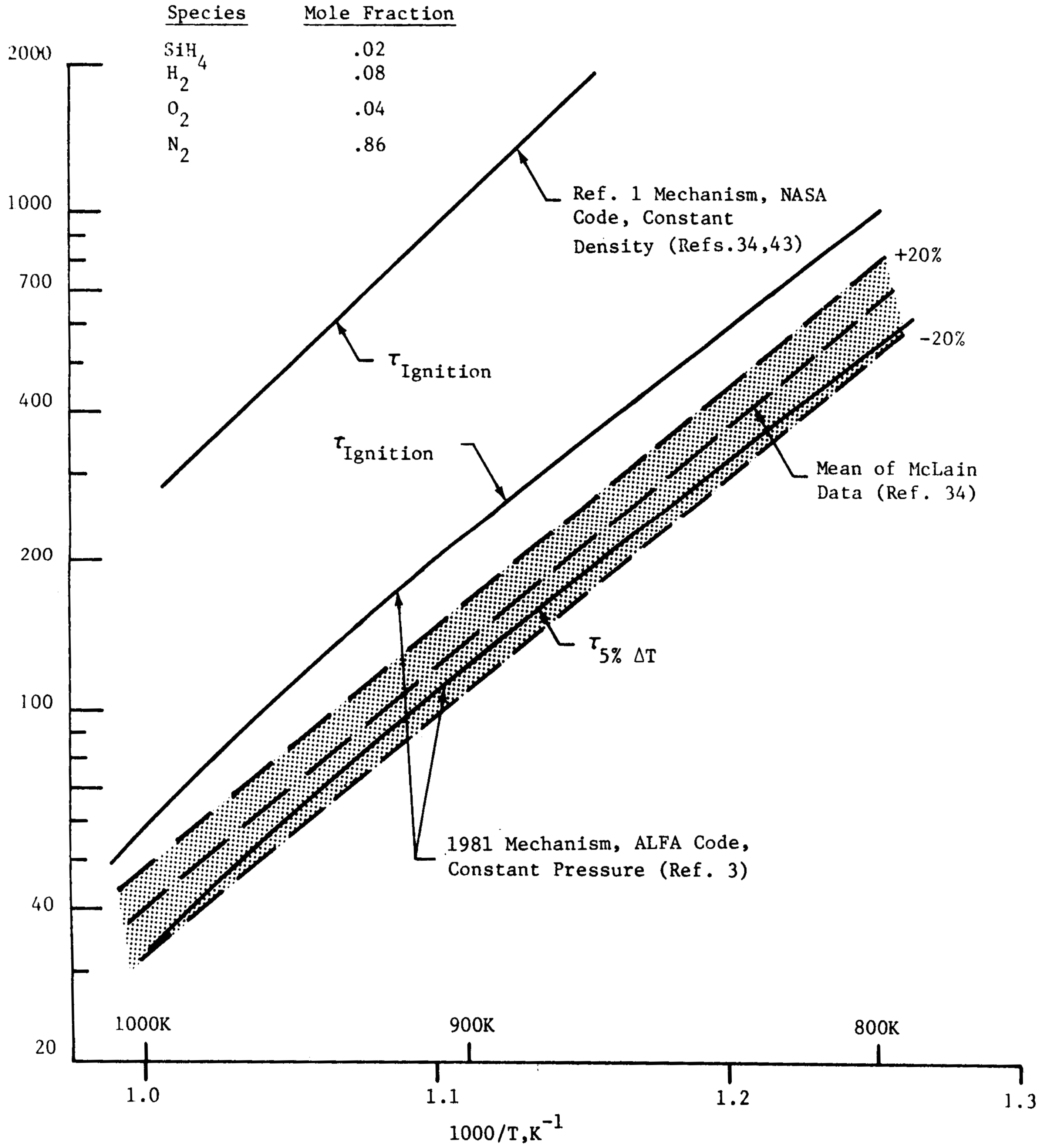

Fig. B-1 - Ignition Times for 20/80 Percent Silane/Hydrogen
P_o = 1.25 atm (All Calculations)

of Table B-1 and the ALFA code (Ref. B-3) run in a constant pressure option, using τ_{Ignition} as defined above, and also, $\tau_{5\%\Delta T}$. The latter delay time corresponds to the time required to reach 5 percent of the fully equilibrated temperature rise, as in Ref. B-1. As already observed elsewhere in this text, a more correct calculational procedure for analysis of shock tube ignition delay measurements involves computation of τ_{Ignition} in a constant density flow option, as by McLain - which option was not available in the particular version of the ALFA code employed in this study. However, based on experience, computations of τ_{Ignition} at constant density fall somewhere between the computations of $\tau_{5\%\Delta T}$ and τ_{Ignition} at constant pressure. Thus the curves computed using the ALFA code and the present reaction mechanism, which straddle the McLain data to within at least a factor of two are also expected to straddle computed values of τ_{Ignition} at constant density, using the present reaction mechanism. Agreement with the present data is thus to within at least a factor of two.

B. Silane-Methane Combustion

Parametric computations of methane combustion in air flows with silane as combustion aid have been performed with the refined mechanism. These computations extend over initial temperatures of from 600 to 1200 K, at constant pressures from 0.5 to 2.0 atm, and overall stoichiometries from 0.25 to 1.0, with from 2 to 20 vol.% silane in the methane fuel. Consistent with early, unpublished engine tests with hydrocarbons at GASL, we find that use of silane as an ignition aid materially reduces required ignition delays and combustion times for methane in air. For example, at 1 atm constant pressure and an initial temperature of 1000 K, the computed value of τ_{Ignition} is reduced from 0.70 sec for stoichiometric CH_4 - air by three orders of magnitude - to 5.3×10^{-4} sec - with 10 vol.% SiH_4 in the fuel; the corresponding time requirement to reach 95% of the equilibrium combustion temperature rise is reduced from 0.73 to 9.2×10^{-4} sec, i.e., also by nearly three orders of magnitude. For the range of parameters explored, $\tau_{5\%\Delta T}$ and $\tau_{95\%\Delta T}$ are found to vary essentially as the first power of reciprocal (constant) pressure. The T versus time plots show interesting structure with the mechanism as presently constituted. Typically there is a relatively steep, accelerating initial temperature rise which gradually becomes less steep as reactions proceed (i.e., showing some cool flame characteristics in early stages) and then gradually increases again, with the slope characteristically being steepest at τ_{Ignition}. At this point the cause of this very interesting and unexpected behavior has not been ascertained.

CONCLUSIONS

Detailed kinetics mechanisms for silane-hydrogen and methane oxidation have been combined and adapted for use in computation of the characteristics of supersonic air-methane-silane/H_2 ignition and heat release. The resulting formulation results in a workable combustion mechanism which (with the ALFA code) typically requires only nominal computational time - say 5 to 20 CRU for a representative 95% heat release run, with the NASA Langley Research Center CDC 6600 computer.

After initial mechanistic refinement interfacing with very recently obtained NASA-Langley shock tube ignition data, predictions made with the refined mechanism agree to at least within a factor of 2 with these early shock tube measurements of ignition delay over the range 800 to 1000 K for silane-H_2-O_2/N_2 mixtures. Additionally, a sensitivity to ignition promotion in silane-air mixtures at temperatures near ambient by trace species arising from contaminants and/or heterogeneous processes has been demonstrated with the present mechanism, again in keeping with experimental observation.

Initial favorable results for use of silane as an ignition aid in supersonic methane combustors have been obtained in a parametric examination of theoretical ignition and reaction times in silane-CH_4-air mixtures. Reductions in ignition and reaction times by factors on the order of 3 orders of magnitude is predicted, depending on particulars. Use of silane as an ignition aid thus appears to offer considerable promise for augmented combustion of hydrocarbon fuels, as well as for hydrogen.

RECOMMENDED NASA SILANE PROGRAM DIRECTIONS

Based on the favorable results of this study and our interaction with and understanding of the status of the NASA silane hypersonic combustion program, we offer the following recommendations for the further implementation and study of this very promising advanced combustion technique:

- Measure silane-hydrogen/oxygen-nitrogen ignition delays in shock tube experiments over a range of initial temperatures, pressures and compositions, utilizing existing computational kinetics codes to support analysis of the experiments. Analysis of combustion products and measurement of combustion temperature, particularly in fuel-rich mixtures with excess hydrogen, is required to assess the role of nonequilibrium combustion. (The latter work could perhaps be accomplished using a flat flame burner to supplement the shock tube.)

- Extend the measurements and analysis to silane-hydrocarbon combustion, first to methane, then to propane, and ultimately to highly practical flight candidates such as JP-type aviation fuels.

- Aggressively pursue engine tests using silane as an igniter, as well as a pilot, for each of the main fuels of interest (i.e., H_2, CH_4, C_3H_8, JP, etc.). Couple these engine tests with kinetic analysis of the combustor flow fields, including recirculation effects known to be of paramount importance to successful flameholding. (A three-dimensional code is required, necessitating use of combustion mechanisms reduced to their essentials only.)

- Explore the use of silane itself, or of higher silanes, as the primary fuel in a hypersonic propulsion system.

REFERENCES

B-1. Beach, H.L., Jr., E.A. Mackley, R.C. Rogers, and W. Chinitz, "Use of Silane in Scramjet Research," 17th JANNAF Combustion Meeting, Volume I, Debra Sue Eggleston, ed., CPIA Publ. 329 (Contract N00024-78-C-5384), Appl. Phys. Lab., Johns Hopkins Univ., Nov. 1980, pp. 639-659.

B-2. Jones, R.A., and P.W. Huber, "Toward Scramjet Aircraft," Astronautics and Aeronautics, February 1978, pp. 38-48.

B-3. Thoenes, J., W.L. Hendricks, S.C. Kurzius and F.C. Wang, "Advanced Laser flow Analysis Theory and User's Guide," AFWL-TR-78-19, February 1979.

B-4. Doncaster, A.M., and R. Walsh, "Kinetics of the Gas-Phase Reaction between Iodine and Monosilane and the Bond Dissociation Energy D (H_3Si-H)," Int. J. Chem. Kinetics, Vol. 13, 1981, pp. 503-514.

B-5. Emeleus, H.J., and K. Steward, "The Oxidation of the Silicon Hydrides - Parts I and II," J. Chem. Soc. (London), 1935, pp. 1182-1189 and 1936, pp. 677-684.

B-6. Kondratiev, V.N., and E.E. Nikitin, Gas-Phase Reactions, Springer-Verlag, New York, 1981.

B-7. Slack, M., and A. Grillo, "Investigation of Hydrogen-Air Ignition Sensitized by Nitric Oxide and by Nitrogen Dioxide," NASA CR-2896, 1977.

B-8. Cohen, N., and K. Westberg, Aerospace Chemical Kinetics Data Sheets; ongoing critical reviews of rate coefficients and rate data, 1979-.

B-9. Hampson, R.F., "Chemical Kinetic and Photochemical Data Sheets for Atmospheric Reactions," NBS Report FAA-EE-80-17, April 1980; update to NBS Special Publication 513, R.F. Hampson and D. Garvin, May 1978.

B-10. Dougherty, E.P., and H. Rabitz, "Computational Kinetics and Sensitivity Analysis of Hydrogen-Oxygen Combustion," J. Chem. Phys., Vol. 72, 1980, pp. 6571-6586.

B-11. Tabayashi, K., and S.H. Bauer, "The Early Stages of Pyrolysis and Oxidation of Methane," Combustion and Flame, Vol. 34, 1979, pp. 63-83.

B-12. Huffington, W.M., G.E. Parks, K.G.P. Sulzmann and S.S. Penner, "Studies of Methane Oxidation Kinetics," Sixteenth Intl. Symposium on Combustion (The Combustion Institute, Pittsburgh, 1977), pp. 997-1011.

B-13. Ernst, J., Hg. Wagner, and R. Zellner, "A Combined Flast Photolysis/Shock-Tube Study of the Absolute Rate Constants for Reactions of the Hydroxyl Radical with CH_4 and CF_3H around 1300 K," Ber. Bunsenges. Phys. Chem., Vol. 82, 1978, pp. 409-414.

B-14. Clark, T.C., and J.E. Dove, "Examination of Possible Non-Arrnehius Behavior in the Reactions H + C_2H_6, H + CH_4 and CH_3 + C_2H_6," Can. J. Chem., Vol. 51, 1973, p. 2147.

B-15. Roth, P., and Th. Just, "Atom-Resonanzabsorptionmessungen beim thermischen Zerfall von Methane hinter Stosswellen," Ber. Bunsenges. Phys. Chem., Vol. 79, 1975, pp. 682-686.

B-16. Roth, P., and Th. Just, "Atomabsorptionmessungen zur Kinetik der Reaktion CH_4 + O CH_3 + OH im Temperaturbereich $1500 \leq T \leq 2250$ K," Ber. Bunsenges, Phys. Chem., Vol. 81, 1977, pp. 572-577.

B-17. Felder, W., and A. Fontijn, "High Temperature Photochemistry, a New Technique for Rate Coefficient Measurements over Wide Temperature Ranges: Initial Measurements on the O + CH_4 Reaction from 525-1250 K," Chem. Phys. Lett., Vol. 67, 1979, pp. 53-56.

B-18. Westbrook, C.K., and F.L. Dryer, "Prediction of Laminar Flame Properties of Methanol-Air Mixtures," Combustion and Flame, Vol. 37, 1980, pp. 171-192; see also Combustion Sci. Technol., Vol. 20, 1979, p. 125.

B-19. Gardiner, W.C., and D.B. Olson, "Chemical Kinetics of High Temperature Combustion," Ann. Rev. Phys. Chem., Vol. 31, 1980, pp. 377-399.

B-20. Tsuboi, T., and Hashimoto, "Shock Tube Study on Homogeneous Thermal Oxidation of Methanol," Combustion and Flame, Vol. 42, 1981, pp. 61-76.

B-21. Washida, N., "Reaction of Methyl Radicals with O (^{3}P), O_2 and NO," J. Chem. Phys., Vol. 73, 1980, pp. 1665-1672.

B-22. Stief, L.J., D.F. Nava, W.A. Payne and J.V. Michael, "Rate Constant for the Reaction of Hydroxyl Radical with Formaldehyde over the Temperature Range 228-362 K," J. Chem. Phys., Vol. 73, 1980, pp. 2254-2258.

B-23. Klemm, R.B., "Absolute Rate Parameters for the Reactions of Formaldehyde with O Atoms and H Atoms over the Temperature Range 250-500 K," J. Chem. Phys., Vol. 71, 1979, pp. 1987-1993.

B-24. Klemm, R.B., E.G. skolnik and J.V. Michael, "Absolute Rate Parameters for the Reaction of O (^{3}P) with H_2CO over the Temperature Range 250 to 750 K," J. Chem. Phys., Vol. 72, 1980, pp. 1256-1264.

B-25. Reilly, J.P., J.H. Clark, C.B. Moore, and G.C. Pimentel, "HCO Production, Vibrational Relaxation, Chemical Kinetics and Spectroscopy Following Laser Photolysis of Formaldehyde," *J. CHem. Phys.*, Vol. 69, 1978, pp. 4381-4394.

B-26. Shibuya, K., T. Ebata, K. Obi, and I. Tanaka, "Rate Constant Measurements for the Reactions of HCO with NO and O_2 in the Gas Phase," *J. Phys. Chem.*, Vol. 81, 1977, pp. 2292-2294.

B-27. Niki, H., E.E. Daby and B. Weinstock, *Twelfth Intl. Symposium on Combustion*, (The Combustion Institute, Pittsburgh, 1969), p. 277.

B-28. Arustamyan, A.M., I.K. Shakhnazaryan, A.G. Philipossyan, and A.B. Nalbandyan, "The Kinetics and the Mechanism of the Oxidation of Carbon Monoxide in the Presence of Hydrogen," *Int. J. Chem. Kinetics*, Vol. 12, 1980, pp. 55-75.

B-29. Baulch, D.L., and J. Duxbury, "Ethane Decomposition and the Reference Rate Constant for Methyl Radical Recombination," *Combustion and Flame*, Vol. 37, 1980, pp. 313-326.

B-30. Laufer, A.H., "Kinetics of Gas Phase Reactions of Methylene," *Rev. Chemical Intermediates*, Vol. 4, 1981, pp. 225-257.

B-31. Bhaskaran, K.A., P. Frank, and T. Just, *Proc. 12th Intl. Symposium on Shock Tubes and Waves* (Magnus, Jerusalem, 1980).

B-32. Asaba, T., K. Yoneda, N. Kakihara, and T. Hikita, "A Shock Tube Study of Ignition of Methane-Oxygen Mixtures," *Ninth Intl. Symposium on Combustion* (The Combustion Institute, Pittsburgh, 1963), pp. 193-200.

B-33. Dean, A.M., R.L. Johnson, and D.C. Steiner, "Shock-Tube Studies of Formaldehyde Oxidation," *Combustion and Flame*, Vol. 37, 1980, pp. 41-62.

B-34. McLain, A.G., NASA-Langley Research Center unpublished results, 1981.

B-35. Strater, K., "Controlled Oxidation of Silane," *RCA Review*, Vol. 29, 1968, pp. 618-629.

B-36. Baliga, B.J., and S.K. Ghandi, "Growth of Silica and Phosphosilicate Films," *J. Appl. Phys.*, Vol. 44, 1973, pp. 990-994.

B-37. Newman, C.G., H.E. O'Neal, M.A. Ring, F. Leska, and N. Shipley, "Kinetics and Mechanism of the Silane Decomposition," *Intl. J. Chem. Kinetics*, Vol. 11, 1979, pp. 1167-1182.

B-38. Purnell, J.H., and R. Walsh, "Arrhenius Parameters for Monosilane Pyrolysis," *Proc. Roy. Soc.*, Vol. A 321, 1971, p. 341.

B-39. Atkinson, R., and J.N. Pitts, "Absolute Rate Constants for the Reactions of O (^3P) Atoms and OH Radicals with SiH_4 over the Temperature Range of 297-438 K," Int. J. Chem. Kinetics, Vol. 10, 1978, pp. 1151-1160.

B-40. Arthur, N.L. and T.N. Bell, "An Evaluation of the Kinetic Data for Hydrogen Abstraction from Silanes in the Gas Phase," Rev. Chem. Intermediates, Vol. 2, 1978, pp. 37-74.

B-41. Vasilyeva, L.L., V.N. Drozdov, S.M. Repinskii, and K.K. Svitashev, "Deposition of Silica Films by the Oxidation of Silane in Oxygen - I. The Kinetics and Physicochemical Model of the Process," Thin Solid Films, Vol. 55, 1978, pp. 221-228.

B-42. Berezhnoi, A.S., Silicon and Its Binary Systems, Consultants Bureau, New York, 1960.

B-43. McLain, A.G., and C.S.R. Rao, "A Hybrid Computer Program for Rapidly Solving Flowing or Static Chemical Kinetic Problems Involving Many Chemical Species," NASA TM X-3403, Langley Research Center, Va., July 1976.

Appendix C

GLOBALIZATION OF HYDROCARBON KINETICS FOR HYPERSONIC COMBUSTION COMPUTATIONS

Appendix C

SUMMARY

A generalized semi-global model of hydrocarbon flame front kinetics suitable for use with the GIM code has been developed for analysis of hypersonic combustion. Real fuels of most interest are liquid hydrocarbon aircraft-type fuels, and the model development has accordingly specifically addressed these fuels.

C.1 BACKGROUND

Modeling the details of combustion of real hydrocarbon fuels including the intricacies of complex pre-ignition kinetics remains remote for two primary reasons:

1. The mechanistic details of the combustion of higher hydrocarbons are still largely unresolved.
2. Even if the detailed kinetics were unambiguously known, the magnitude of the computational problem would still swamp existing computational facilities.

To overcome this, partially empirical combustion models for hydrocarbons ("global, semi-global and quasi-global" models, recently reviewed by Chinitz in Ref. C-1) are under development - all of which assume the hydrocarbon to decompose in a single, fictitious global reaction to relatively simple products, viz. CO, H_2, H_2O and/or C_1-C_2 species such as CH_4 or C_2H_4.

Global models utilize irreversible global rate expressions derived from curve fits to data for all of the combustion products. For example, the global model of Dryer et al. (Ref. C-2) for propane combustion utilizes the following four global reactions to describe the temporal behavior of the species C_3H_8, O_2, C_2H_4. H_2, CO, CO_2 and H_2O:

$$C_3H_8 \rightarrow 1.5\ C_2H_4 + H_2$$

$$C_2H_4 + O_2 \rightarrow 2\ CO + 2\ H_2$$

$$CO + 0.5\ O_2 \rightarrow CO_2$$

$$H_2 + 0.5\ O_2 \rightarrow H_2O$$

None of the individual steps in such models bears any semblance to the fundamental free radical-dominated kinetic steps painstakingly documented in studies of actual combustion mechanisms undertaken over the course of this century. This results in rather obvious shortcomings and great uncertainty in extrapolation beyond the narrow data range fit by the computationally straightforward, but restrictive, expressions employed.

Semi-global models relax this major shortcoming by allowing $CO/H_2/H_2O$ intermediate reaction products to follow their individual, detailed fundamental free radical-dominated kinetic paths while utilizing a global expression for consumption of the hydrocarbon to intermediate species, e.g., as in the global, irreversible finite rate step proposed by Harsha et al. (Ref. C-3) and recommended by Chinitz (Ref. C-1):

$$C_n H_m + \frac{n}{2} O_2 \rightarrow \frac{m}{2} H_2 + n\ CO$$

Quasi-global models allow an additional degree of complexity by incorporating intermediate yields of C_1-C_2 hydrocarbon decomposition products. Individual detailed fundamental kinetic paths of these species are then followed along with reactions of the $CO/H_2/H_2O$ products of the initial globalized hydrocarbon pyrolysis reaction (e.g., $C_n H_{2n+2} + M \rightarrow (n/2) C_2 H_4 + H_2 + M$).

At this time, none of the models is clearly best and all have both shortcomings and controversial features outside of the limited regimes for which they have been developed. In particular, existing global models do not give acceptable results in flows dominated by long ignition delay times.

After review of the problem we concluded that the best available reasonably computationally efficient yet data-based compromise lay in development of a generalized semi-global model of flame front and post-flame front kinetics with heavy reliance on experimental measurements of ignition delay for the specific hydrocarbon considered.

C.2 TECHNICAL APPROACH

Experimental measurements of auto-ignition delays (kinetically-limited) are usually available for fuels of interest over the range of parameters likely to be encountered. If not available, experimental facilities exist which can generate the required data. Such data are to be utilized heavily in the construction of a relatively simple but realistic model of the combustion kinetics of (generic) hydrocarbon fuels, as follows. Coupled with fundamental $CO/H_2/H_2O$ rate processes the resulting model is adequate for finite rate analysis of hypersonic combustion by the GIM or other complex flowfield modeling codes.

The temporal development of combustion in a given parcel of fuel-air mixture is conceptually divided into three regions:

Region 1 - Physical Processes

In this region pre-ignition processes are dominated by physical processes which include droplet formation, heating, vaporization, diffusion, mixing and temperature equilibration with the air stream. Typically, this region is less important than Region 2, below. Region 1 is characterized by a required physical processes residence time, τ_p.

Region 2 - Auto-Ignition Kinetics

In this region pre-ignition processes are dominated by the highly complex chemical processes which result in the partial decomposition of high molecular weight hydrocarbon species and the formation of critical concentrations of intermediate free-radical species, with only a small change in temperature and in the concentration of major species (i.e., fuel and O_2). Region 2 is characterized by a required auto-ignition residence time, τ_{AI}.

Region 3 - Flame Front and Post-Flame Front Kinetics

In Region 3, hydrocarbon molecules are rapidly consumed by oxidation, resulting in a hot flame front with accompanying combustion of H_2/CO/ C_1-C_2 intermediates (C_1-C_2 species are not incorporated in the present model) followed by post-flame front free radical recombination processes.

Figure C-1 summarizes these regions and Fig. C-2 summarizes results of several workers for auto-ignition delays of aircraft-type fuel sprays in air, with auto-ignition delays for H_2 superimposed.

METHODOLOGY

Region 1. Pre-ignition physical processes (i.e., spray and droplet formation, vaporization, mixing, temperature equilibration, etc.) are assumed to be separately analyzed. Normally the physical time scale will be a multiple - a - of the time required for the initial liquid jets - moving at velocity v_L - to traverse a characteristic cross channel flow dimension X, where X will as often as not be a spray bar half spacing, or its equivalent. Thus,

$$\tau_p = (X/v_L)\ a \tag{C.1}$$

where a is a number presumed of order unity obtained in ancilary computations of the time requirement for these physical events preceding ignition. All reaction rates are set equal to zero in Region 1.

Region 2. Auto-ignition delay data like those shown in Fig. C-2 are assumed to be available for a specific fuel-air combustion problem. Functionally τ_{AI} is input as

$$\tau_{AI} = \frac{A_{AI}\ T^N}{P^b\ .\ f(\phi)} \exp\frac{E_{AI}}{RT} \text{ sec} \tag{C.2}$$

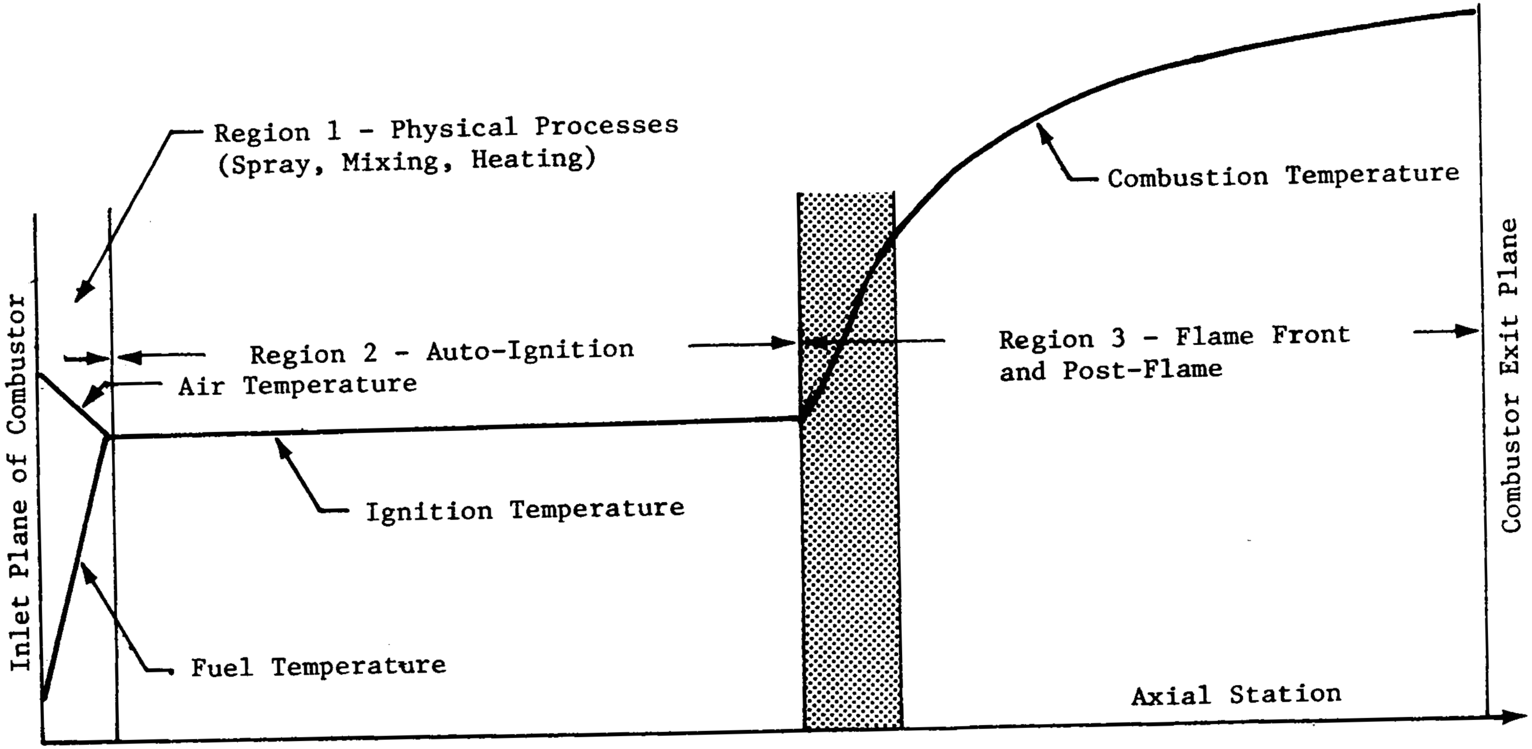

Fig. C-1 - Temporal Regimes in Combustor

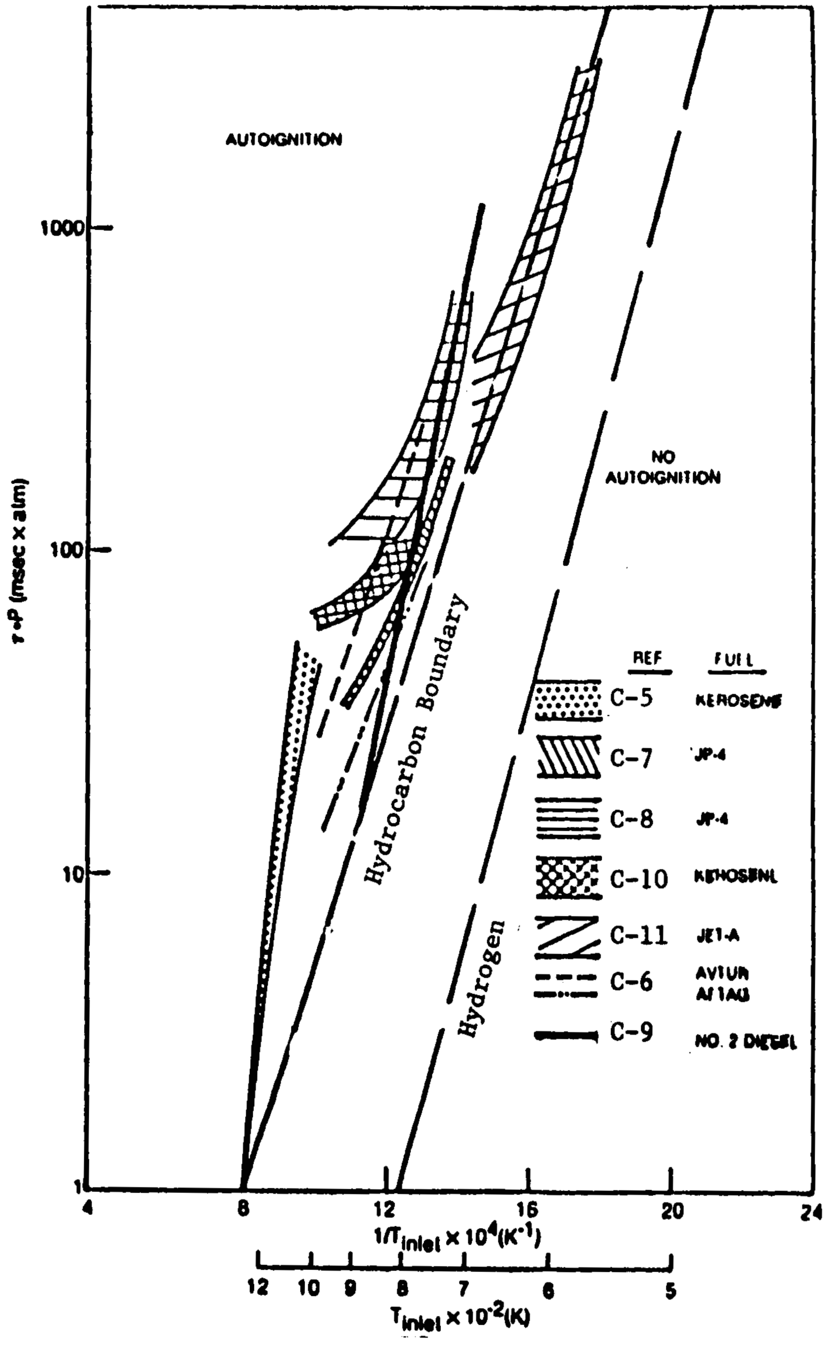

Fig. C-2 - Autoignition of Liquid Hydrocarbon Fuel Sprays in Air (Largely from Ref. C-4, as cited in Ref. C-9)

$$\tau_{AI,\text{Hydrocarbons}} = \frac{1.22 \times 10^{-6}}{P} \exp\frac{8400}{T} \text{ sec (Boundary)}$$

$$\tau_{AI,H_2} = \frac{8.0 \times 10^{-9}}{P} \exp\frac{9600}{T} \text{ sec (Ref. C-12)}$$

where

A_{AI} = Pre-exponential constant of curve fit to auto-ignition data

T = Temperature in Region 2, K

N = Temperature exponent (default = 0)

P = Pressure in Region 2, atm

b = Pressure exponent (default = 1)

$f(\phi)$ = Function of fuel-air stoichiometry ratio, (default value of $f(\phi) = 1$)

$$\phi = \frac{\text{(Fuel: Air molar ratio)}}{\text{(Fuel: Air molar ratio at stoichiometry)}}$$

E_{AI} = Auto-ignition delay apparent activation energy, cal/mole

R = Gas constant

All reaction rates are set equal to zero in Region 2 also, corresponding to the pre-ignition condition of hardly noticeable change in T, P and major species concentration profiles evident in plots such as those of Fig. A-1 and A-2. The onset of ignition at the end of Region 2 - or rather the beginning of Region 3 - is modeled by inputting a discrete, characteristic post-ignition value for the mole fraction of chain branching H atom free radical - X_{H_I} - and initiating the globalized kinetics as discussed below.

Region 3

The kinetics are switched on in Region 3, with the mole fraction of H atoms initialized at a level corresponding to post-ignition, pre-flame conditions, i.e.,

X_{H_I} = Input value

(C.3)

X_{H_I} = A number of order 1×10^{-4} to 1×10^{-3} (see e.g., Figs. A-1 and A-2).

Note that the characteristic rise time for the H atom population to increase from X_{H_I} to a level typical of flame fronts, i.e., a number of order 10^{-2} is a fraction of the autoignition delay for H_2, i.e., τ_{AI,H_2}. From Fig. C-2 it is evident that τ_{AI,H_2} is appreciably shorter than $\tau_{AI,\ Hydrocarbons}$. Thus the H atom rise time from X_{H_I} to flame front levels is only a relatively small fraction of the total auto-ignition delay for hydrocarbon combustion. Results are accordingly relatively insensitive to the choice of X_{H_I}. For hydrocarbon combustion, 1×10^{-4} is a good choice for X_{H_I}. For H_2 combustion, 1×10^{-3} is however more appropriate as the corresponding H atom rise time from 10^{-4} to 10^{-3} mole fraction can be a significant fraction of $\tau_{AI,\ H_2}$.

A rate coefficient - k_{HC} - for depletion of hydrocarbon at the entrance to Region 3 is input such that the time constant for hydrocarbon oxidation is equal to $\tau_{AI,HC}/10$. Thus, the hydrocarbon concentration is decreased by finite rate reaction to 1/e of its initial value in a time equal to 10 percent of $\tau_{AI,HC}$ - i.e., the flame front thickness is set at about 10 percent of the kinetic ignition length. Thus, letting

$$C_n H_m + \frac{n}{2} O_2 \xrightarrow{k_{HC}} n\ CO + \frac{m}{2} H_2 \qquad (C.4)$$

be the irreversible finite-rate oxidation reaction for the hydrocarbon, with rate coefficient k_{HC} defined by

$$-\frac{d\,[C_n H_m]}{dt} = k_{HC}\,[C_n H_m]\,[O_2] \qquad (C.4a)$$

and

$$-\frac{d\,[O_2]}{dt} = \frac{n}{2}\,k_{HC}\,[C_n\,H_m]\,[O_2] \qquad (C.4b)$$

$$\frac{d\,[CO]}{dt} = n\,k_{HC}\,[C_n\,H_m]\,[O_2] \qquad (C.4c)$$

$$\frac{d\,[H_2]}{dt} = \frac{m}{2}\,k_{HC}\,[C_n\,H_m]\,[O_2] \qquad (C.4d)$$

the rate coefficient k_{HC} is given by

$$k_{HC}\,[O_2]_o = \frac{1}{\tau_{HC}} = \frac{10}{\tau_{AI,HC}} \qquad (C.5)$$

Thus

$$k_{HC} = \frac{10}{[O_2]_o\,\tau_{AI,HC}}$$

$$= \frac{10\,.\,P^b\,.\,f(\phi)}{[O_2]_o\,A_{AI}\,T^N}\exp-\frac{E_{AI}}{RT} \qquad (C.6)$$

For air

$$[O_2]_o = (P/T) \times 1.54 \times 10^{21} \text{ particle cm}^{-3} \qquad (C.7)$$

with P in atm and T in K, neglecting fuel dilution. Thus

$$k_{HC} = \left(\frac{6.5 \times 10^{-21}}{A_{AI}\,T^{N-1}}\right)P^{b-1}\,.\,f(\phi)\,.\,\exp\frac{-E_{AI}}{RT} \qquad (C.8)$$

$$\text{cm}^3\,.\,\text{particle}^{-1}\,.\,\text{sec}^{-1}$$

To fix this concept, consider the aircraft fuel ignition delay data of Fig. C-2. While each individual data set can be represented by a specific expression, if this is desired, <u>all</u> of the data are bounded by the expression

$$\tau_{AI,HC} = \frac{1.22 \times 10^{-6}}{P} \exp\frac{8400}{T} \text{ sec}$$

as indicated in the caption to Fig. C-2. Employing this as representative of a generic aircraft fuel hydrocarbon, substitution in Eq. (C.8) yields the expression

$$k_{HC} = 5.3 \times 10^{-15} T \exp -16{,}700/RT \qquad (C.9)$$

Default values for N, b and $f(\phi)$ have been used in the above expression in the absence of more specific inputs, which may or may not be available for a particular case.

The reaction set is completed by adding those elementary reactions necessary and sufficient to model H_2/CO afterburning combustion efficiently as in the basic plume chemistry models utilized in Lockheed's analyses of SSME/SRB/Trident, etc., advanced propulsion systems. The complete semi-global hydrocarbon kinetics model is shown in Table C-1. Elementary rate coefficients for the reversible reactions 2 through 9 are all from Table B-1 and have previously been discussed.

Table C-1 - SEMI-GLOBAL HYDROCARBON KINETICS MODEL

Reaction	Rate Coefficient, cm^3-particle^{-1}-sec^{-1} units
Not Reversible:	
1. $C_n H_m + \frac{n}{2} O_2 \rightarrow n\,CO + \frac{m}{2} H_2$	$\left(\frac{6.5 \times 10^{-21}}{A_{AI}\, T^{N-1}}\right) P^{b-1} \cdot f(\phi) \cdot \exp\frac{-E_{AI}}{RT}$
Test Case: Generic Aircraft Fuel:	
$C_{10} H_{20} + 5O_2 \rightarrow 10\,CO + 10\,H_2$;	$k_1 = 5.3 \times 10^{-15}\, T \exp{-16{,}700/RT}$
Reversible:	
2. $H + O_2 \rightarrow OH + O$	$1.0 \times 10^{-13}\, T \exp{-14{,}800/RT}$
3. $OH + H_2 \rightarrow H_2O + H$	$1.8 \times 10^{-15}\, T^{1.3} \exp{-3{,}650/RT}$
4. $O + H_2 \rightarrow OH + H$	$3.0 \times 10^{-14}\, T \exp{-8{,}900/RT}$
5. $OH + OH \rightarrow H_2O + O$	$1.0 \times 10^{-16}\, T^{1.3}$
6. $CO + OH \rightarrow CO_2 + H$	$1.1 \times 10^{-13} \exp(T/1100)$
7. $H + OH + M \rightarrow H_2O + M$	$6.1 \times 10^{-26}\, T^{-2}$
8. $H + H + M \rightarrow H_2 + M$	$1.8 \times 10^{-30} \exp{-4{,}300/RT}$
9. $CO + O + M \rightarrow CO_2 + M$	$4.0 \times 10^{-33} \exp{-4{,}300/RT}$

M Body Catalytic Weighting Factors:

$N_2 = 1.0$, $O_2 = 1.1$, $C_n H_m = 3.0$, $H_2 = 2.0$, $H_2O = 12.0$, $CO = 1.0$,
$CO_2 = 3.0$, $H = 16.0$, $O = 16.0$, $OH = 16.0$

REFERENCES

C-1. Chinitz, W., "An Assessment of Global and Quasi-Global Models of Hydrocarbon and Hydrogen Combustion Kinetics for Reacting Flowfield Calculations," in Computational Methods for Ramjets, CPIA Publication 373, February 1983.

C-2. Hautman, D.J., F.L. Dryer, K.P. Schug, and I. Glassman, "A Multiple-Step Overall Kinetic Mechanism for the Oxidation of Hydrocarbons," Combustion Science, Vol. 25, 1981, pp. 219-235.

C-3. Harsha, P.T., R.B. Edelman, S.N. Schmotolocha, and R.J. Pederson, "Combustor Modeling for Ramjet Development Programs," AGARD Conf., Preprint No. 307, 1981.

C-4. Sturgess, G.J., in Premixed-Prevaporized Combustor Technology Forum, NASA Conference Publication 2078 (1979).

C-5. Mullins, B.P., Fuel, Vol. 32, (1953).

C-6. Stringer, F.W., A.E. Clarke, and J.S. Clarke, "The Spontaneous Ignition of Hydrocarbon Fuels in a Flowing System," Proc. Auto. Div., Institution of Mechanical Engineers (1970).

C-7. Taback, E.D., "The Auto-ignition Characteristics of JP-4 at High Temperature and Pressure," PWA TDM-2284, 1971.

C-8. Spadaccini, L.J., J. of Engineering for Power, Trans. ASME 99A, January 1977.

C-9. Spadaccini, L.J., and J.A. TeVelde, "Autoignition Characteristics of Aircraft-Type Fuels," Combustion and Flame, Vol. 46, 1982, pp. 283-300.

C-10. Mestre, A., and F. Ducourneau, "Recent Studies of the Spontaneous Ignition of Rich Air-Kerosene Mixtures," Combustion Institute European Symposium, 1973.

C-11. Marek, C.J., L. Papathakos, and P. Verbulecz, "Preliminary Studies of Auto-ignition and Flashback in a Premixing-Prevaporizing Flame Tube Using Jet-A Fuel at Lean Equivalence Ratios," NASA TM-X-3526, May 1977.

C-12. Pergament, H.S., "A Theoretical Analysis of Nonequilibrium Hydrogen-Air Reactions in Flow Systems," [Preprint] 63113, American Inst. Aeronaut. and Astronaut., April 1963, as cited in Ref. C-13.

C-13. Huber, P.W., C.J. Schexnayder, and C.R. McClinton, "Criteria for Self-Ignition of Supersonic Hydrogen-Air Mixtures," NASA TP 1457, August 1979.

Appendix D

PROGRESSIVE ASSEMBLY OF THE GIM CODE ELEMENTS

Appendix D

D.1 INTRODUCTION

This appendix describes the GIM code difference analogs from a slightly different perspective than that developed in the previous documentation. This development is based on new weight functions which allow the integration of the analogs in a closed form which is amenable to vectorization and repetative calculation. As a result, the analogs can now be computed with great efficiency when needed (i.e., "progressively") rather than occupying machine storage. This saving in storage is particularly important in the solution of large three-dimensional problems.

It is assumed here, as in all GIM development, that all functions of the local variables can be expressed in a discretizing relation as interpolated sums of point functions:

$$f(\overline{\eta}) = S_i(\overline{\eta})\, f_i; \quad i=1,\ldots,2^d$$

where d is the problem dimensionality. Further, the shape functions, S_i, are assumed here to be multilinear Lagrange interpolants.

The following summation conventions hold, except where noted:

1. Repeated indices are summed.
2. Lower case Latin indices run over the 2^d corner points.
3. Greek indices run over the d dimensions.
4. Capital Latin indices run over all nodes in the discrete domain.

D.2 TWO-DIMENSIONAL ANALOGS

The two-dimensional divergence law equation is

$$\frac{\partial U}{\partial t} + \frac{\partial E}{\partial x} + \frac{\partial F}{\partial y} = 0$$

This is modeled by the discrete difference equation on the element e (Fig. D-1a):

$$I^e = A^e_{ij} \dot{U}_j + B^e_{ij} E_j + C^e_{ij} F_j = 0$$

where

$$A^e_{ij} = \int_o^1 d\eta_1 \int_o^1 d\eta_2 \, W_i \, S_j \, \frac{\partial(x,y)}{\partial(\eta_1,\eta_2)}$$

$$B^e_{ij} = \int_o^1 d\eta_1 \int_o^1 d\eta_2 \, W_i \, \frac{\partial(S_j,y)}{\partial(\eta_1,\eta_2)}$$

$$C^e_{ij} = \int_o^1 d\eta_1 \int_o^1 d\eta_2 \, W_i \, \frac{\partial(x,S_j)}{\partial(\eta_1,\eta_2)}$$

and

$S_1 = (1 - \eta_1)(1 - \eta_2)$ $\qquad$ $S_2 = \eta_1 (1 - \eta_2)$

$S_3 = \eta_1 \eta_2$ $\qquad$ $S_4 = (1 - \eta_1) \eta_2$

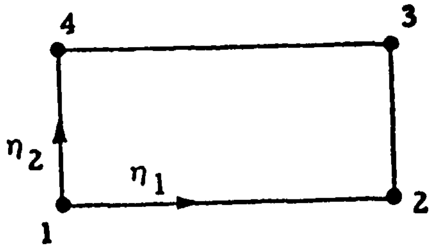

a. Element Domain

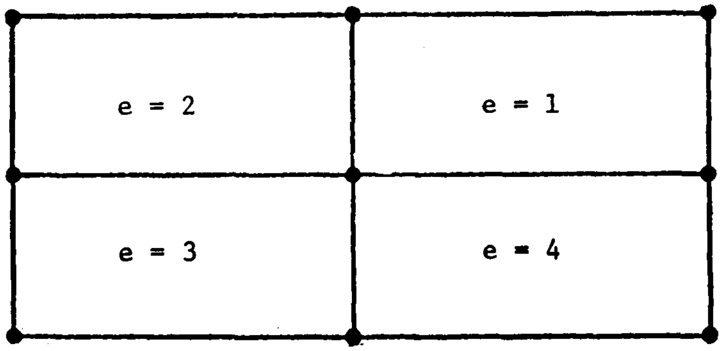

b. Assembled Computational Domain

Fig. D-1 - Two-Dimensional Rectilinear Domains

The choice of the following quadratic weight functions:

$$W_1 = (9 - 36\ \eta_1 + 30\ \eta_1^2)\ (9 - 36\ \eta_2 + 30\ \eta_2^2)$$

$$W_2 = (3 - 24\ \eta_1 + 30\ \eta_1^2)\ (9 - 36\ \eta_2 + 30\ \eta_2^2)$$

$$W_3 = (3 - 24\ \eta_1 + 30\ \eta_1^2)\ (3 - 24\ \eta_2 + 30\ \eta_2^2)$$

$$W_4 = (9 - 36\ \eta_1 + 30\ \eta_1^2)\ (3 - 24\ \eta_2 + 30\ \eta_2^2)$$

yield closed form analogs of the differential expressions. These can be written in the following form:

$$A_{ij}^e = \begin{cases} \left[\dfrac{\delta(x_i,\ y_i)}{\delta(\eta_1,\ \eta_2)} \right]^e & i = j \\ 0 & i = j \end{cases}$$

$$B_{ij}^e\ E_j = \left[\frac{\delta(E_i,\ y_i)}{\delta(\eta_1,\ \eta_2)} \right]^e$$

$$C_{ij}^e\ F_j = \left[\frac{\delta(x_i,\ F_i)}{\delta(\eta_1,\ \eta_2)} \right]^e$$

where the finite difference Jacobian determinant is defined as

$$\left[\frac{\delta(f_i,\ g_i)}{\delta(\eta_1,\ \eta_2)} \right]^e = \varepsilon_{\lambda\nu}\ \Delta_\lambda^e\ f_i\ \Delta_\nu^e\ g_i$$

with no sum on i. $\varepsilon_{\lambda\nu}$ is the two dimensional Levi-Civita symbol and Δ_μ^e f_i is the two point finite difference in the η_μ direction evaluated at point i in element e.

The element equations can be assembled over the four elements which make up the typical 9-node computational domain by performing the weighted Boolean sum

$$\sum_{e=1}^{4} \alpha_e I^e = 0$$

where

$$\sum_{e=1}^{4} \alpha_e = 1$$

This results in an assembled field equation for node N

$$A_{NM} \dot{U}_M + B_{NM} E_M + C_{NM} F_M = 0$$

where

$$A_{NM} = \delta_{NM} \sum_{e=1}^{4} \alpha_e \left[\frac{\delta(x_N, y_N)}{\delta(\eta_1, \eta_2)} \right]^e$$

$$B_{NM} E_M = \sum_{e=1}^{4} \alpha_e \left[\frac{\delta(E_N, y_N)}{\delta(\eta_1, \eta_2)} \right]^e$$

$$C_{NM} F_M = \sum_{e=1}^{4} \alpha_e \left[\frac{\delta(x_N, F_N)}{\delta(\eta_1, \eta_2)} \right]^e$$

Since A_{NM} is diagonal, the resulting difference scheme is an explicit finite difference analog to the divergence law.

D.3 THREE-DIMENSIONAL ANALOGS

The approach to the three-dimensional analogs is directly analogous to the 2-D derivation. The three-dimensional divergence law equation

$$\frac{\partial U}{\partial t} + \frac{\partial E}{\partial x} + \frac{\partial F}{\partial y} + \frac{\partial G}{\partial z} = 0$$

is modeled by the element equation

$$I_e = A^e_{ij} \dot{U}_j + B^e_{ij} E_j + C^e_{ij} F_j + D^e_{ij} G_j = 0$$

where e is the eight-node element (Fig. D-2a) and

$$A^e_{ij} = \int_e d^3\eta \; W_i \; S_j \frac{\partial(x,y,z)}{\partial(\eta_1,\eta_2,\eta_3)}$$

$$B^e_{ij} = \int_e d^3\eta \; W_i \frac{\partial(S_j,y,z)}{\partial(\eta_1,\eta_2,\eta_3)}$$

$$C^e_{ij} = \int_e d^3\eta \; W_i \frac{\partial(x,S_j,z)}{\partial(\eta_1,\eta_2,\eta_3)}$$

$$D^e_{ij} = \int_e d^3\eta \; W_i \frac{\partial(x,y,S_j)}{\partial(\eta_1,\eta_2,\eta_3)}$$

$S_1 = (1 - \eta_1)(1 - \eta_2)(1 - \eta_3)$ $\qquad$ $S_5 = (1 - \eta_1)(1 - \eta_2)\eta_3$

$S_2 = \eta_1 (1 - \eta_2)(1 - \eta_3)$ $\qquad$ $S_6 = \eta_1 (1 - \eta_2)\eta_3$

$S_3 = \eta_1 \eta_2 (1 - \eta_3)$ $\qquad$ $S_7 = \eta_1 \eta_2 \eta_3$

$S_4 = (1 - \eta_1)\eta_2 (1 - \eta_3)$ $\qquad$ $S_8 = (1 - \eta_2)\eta_2 \eta_3$

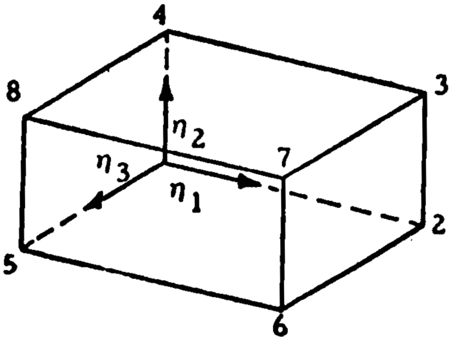

a. Element Domain

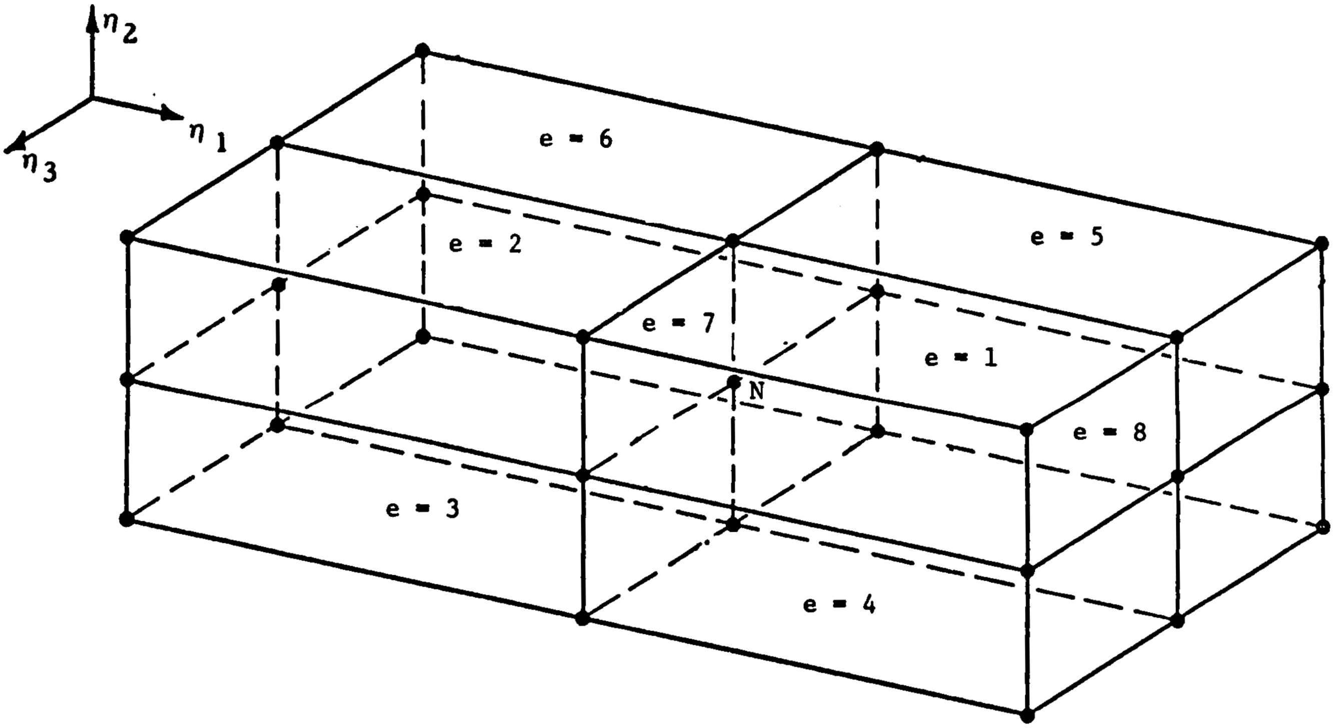

b. Assembled Computational Domain

Fig. D-2 - Three-Dimensional Rectilinear Domains

Choosing the following weight functions:

$$W_1 = 64\ (4 - 30\eta_1 + 60\eta_1^2 - 35\eta_1^3)\ (4 - 30\eta_2 + 60\eta_2^2 - 35\eta_2^3)$$

$$.\ (4 - 30\eta_3 + 60\eta_3^2 - 35\eta_3^3)$$

$$W_2 = 64\ (-\ 1 + 15\eta_1 - 45\eta_1^2 + 35\eta_1^3)\ (4 - 30\eta_2 + 60\eta_2^2 - 35\eta_2^3)$$

$$.\ (4 - 30\eta_3 + 60\eta_3^2 - 35\eta_3^3)$$

$$W_3 = 64\ (-\ 1 + 15\eta_1 - 45\eta_1^2 + 35\eta_2^3)\ (-\ 1 + 15\eta_2 - 45\eta_2^2 + 35\eta_2^3)$$

$$.\ (4 - 30\eta_3 + 60\eta_3^2 - 35\eta_3^3)$$

$$W_4 = 64\ (4 - 30\eta_1 + 60\eta_1^2 - 35\eta_1^3)\ (-\ 1 + 15\eta_2 - 45\eta_2^2 + 35\eta_2^3)$$

$$.\ (4 - 30\eta_3 + 60\eta_2^2 - 35\eta_3^3)$$

$$W_5 = 64\ (4 - 30\eta_1 + 60\eta_1^2 - 35\eta_1^3)\ (4 - 30\eta_2 + 60\eta_2^2 - 35\eta_2^3)$$

$$.\ (-\ 1 + 15\eta_3 - 45\eta_3^2 + 35\eta_2^3)$$

$$W_6 = 64\ (-1 + 15\eta_1 - 45\eta_1^2 + 35\eta_1^3)\ (4 - 30\eta_2 + 60\eta_2^2 - 35\eta_2^3)$$

$$.\ (-\ 1 + 15\eta_3 - 45\eta_3^2 + 35\eta_3^3)$$

$$W_7 = 65\ (-\ 1 + 15\eta_1 - 45\eta_1^2 + 35\eta_1^3)\ (-\ 1 + 15\eta_2 - 45\eta_2^2 + 35\eta_2^3)$$

$$.\ (-\ 1 + 15\eta_3 - 45\eta_3^2 + 35\eta_3^3)$$

$$W_8 = 64\ (4 - 30\eta_1 + 60\eta_1^2 - 35\eta_1^3)\ (-\ 1 + 15\eta_2 - 45\eta_2^2 + 35\eta_3^3)$$

$$.\ (-\ 1 + 15\eta_3 - 45\eta_2^2 + 35\eta_3^3)$$

element analogs result which are similar to the two-dimensional form, i.e.,

$$A^e_{ij} = \begin{cases} \left[\dfrac{\delta(x_i, y_i, z_i)}{\delta(\eta_1, \eta_2, \eta_3)} \right]^e & i = j \\ 0 & i \neq j \end{cases}$$

$$B^e_{ij} \; E_j = \left[\frac{\delta(E_i, y_i, z_i)}{\delta(\eta_1, \eta_2, \eta_3)} \right]^e$$

$$C^e_{ij} \; F_j = \left[\frac{\delta(x_i, F_i, z_i)}{\delta(\eta_1, \eta_2, \eta_3)} \right]^e$$

$$D^e_{ij} \; G_j = \left[\frac{\delta(x_i, y_i, G_i)}{\delta(\eta_1, \eta_2, \eta_3)} \right]^e$$

Here the three-dimensional finite difference Jacobian determinant is

$$\left[\frac{\delta(f_i, g_i, h_i)}{\delta(\eta_1, \eta_2, \eta_3)} \right]^e = \varepsilon_{\lambda\mu\nu} \, \Delta^e_\lambda \, f_i \, \Delta^e_\mu \, g_i \, \Delta^e_\nu h_i$$

(no sum on i).

The three-dimensional assembly consists of a weighted Boolean sum over the eight elements which comprise the classic 27 node finite difference cell (Fig. D-2b).

The assembled equation becomes

$$A_{NM} \, \dot{U}_M + B_{NM} \, E_M + C_{NM} \, F_M + D_{NM} \, G_M = 0$$

where

$$A_{NM} = \sum_{e=1}^{8} \alpha_e \, A^e = \sum_e \alpha_e \, \delta_{NM} \left[\frac{\delta(x_N, y_N, z_N)}{\delta(\eta_1, \eta_2, \eta_3)} \right]^e$$

$$B_{NM}\ E_M = \sum_{e=1}^{8} \alpha_e \left[\frac{\delta(E_N, y_N, z_N)}{\delta(\eta_1, \eta_2, \eta_3)}\right]^e$$

$$C_{NM}\ F_M = \sum_{e=1}^{8} \alpha_e \left[\frac{\delta(x_N, F_N, z_N)}{\delta(\eta_1, \eta_2, \eta_3}\right]^e$$

$$D_{NM}\ G_M = \sum_{e=1}^{8} \alpha_e \left[\frac{\delta(x_N, y_N, G_N)}{\delta(\eta_1, \eta_2, \eta_3)}\right]^e$$

$$\sum_{e=1}^{8} \alpha_e = 1$$

D.4 SUMMARY

This appendix has presented an alternative development of the GIM finite difference analogs. A different choice of weight functions provides closed-form discrete difference expressions of the integral analogs. These expressions are amenable to vectorization and repetative calculation. By calculating the analogs progressively during the solution procedure much storage can be saved.

There are a number of other, less obvious, advantages to this development:

- Fewer nodal connections are necessary (5 in 2-D; 7 in 3-D).
- No significant differences have been seen in comparisons with earlier GIM code versions.
- The MATRIX module is no longer necessary
- The GEOM module performance is significantly improved by eliminating the element matrix integration

- The INTEG module is now independent of the GEOM module. Any grid generation program can now be used so long as its output is suitably formatted.
- The finite difference scheme can now be changed without multiple GEOM runs.

☆U.S. GOVERNMENT PRINTING OFFICE: 1989-627-064/86009.

NASA
National Aeronautics and Space Administration

Report Documentation Page

1. Report No. NASA CR-4183	2. Government Accession No.	3. Recipient's Catalog No.

4. Title and Subtitle Development of the General Interpolants Method for the CYBER 200 Series of Supercomputers	5. Report Date December 1988
	6. Performing Organization Code LMSC-HREC TR D867354
7. Author(s) J. F. Stalnaker, M. A. Robinson, L. W. Spradley, S. C. Kurzius, and J. Thoenes	8. Performing Organization Report No.
	10. Work Unit No. 763-01-61-02
9. Performing Organization Name and Address Lockheed Missiles & Space Company, Inc. Huntsville Research & Engineering Center 4800 Bradford Drive, Huntsville, AL 35807	11. Contract or Grant No. NAS1-15783
	13. Type of Report and Period Covered Contractor Report
12. Sponsoring Agency Name and Address NASA Langley Research Center Hampton, VA 23665	14. Sponsoring Agency Code

15. Supplementary Notes

Final Report
Langley Technical Monitor: James L. Hunt

16. Abstract

The General Interpolants Method (GIM) is a 3-D, time-dependent, hybrid procedure for generating numerical analogs of the conservation laws. This study is directed toward the development and application of the GIM computer code for fluid dynamic research predictions as implemented for the Cyber 200 series of supercomputers. An elliptic and quasi-parabolic version of the GIM code are discussed. Turbulence models, algebraic and differential equations, were added to the basic viscous code. An equilibrium reacting chemistry model and an implicit finite difference scheme are also included.

17. Key Words (Suggested by Author(s)) Elliptic Quasi-parabolic Euler General Interpolants Navier Stokes Parabolic Navier Stokes	18. Distribution Statement Unclassified - Unlimited Subject Category 61

19. Security Classif. (of this report)	20. Security Classif. (of this page)	21. No. of pages	22. Price
Unclassified	Unclassified	212	A10

NASA FORM 1626 OCT 86

NASA-Langley, 1988

For sale by the National Technical Information Service, Springfield, Virginia 22161-2171